

UC Berkeley

UC Berkeley Electronic Theses and Dissertations

Title

Nanoscale Properties of Low-Dimensional Crystalline Organic Semiconductor Films

Permalink

<https://escholarship.org/uc/item/5p2476b9>

Author

Buyanin, Alexander

Publication Date

2016

Peer reviewed|Thesis/dissertation

Nanoscale Properties of Low-Dimensional Crystalline Organic Semiconductor Films

By

Alexander Buyanin

A dissertation submitted in partial satisfaction of the
requirements for the degree of

Doctor of Philosophy

in

Chemistry

in the

Graduate Division

of the

University of California, Berkeley

Committee in charge:

Professor Miquel Salmeron, Co-Chair
Professor Gabor A. Somorjai, Co-Chair
Professor Phillip L. Geissler
Professor Michael Crommie

Fall 2016

Nanoscale Properties of Low-Dimensional Crystalline Organic Semiconductor Films

© Copyright 2016
Alexander Buyanin
All rights reserved

Abstract

Nanoscale Properties of Low-Dimensional Crystalline Organic Semiconductor Films

by

Alexander Buyanin

Doctor of Philosophy in Chemistry

University of California, Berkeley

Professor Miquel Salmeron, Co-Chair

Professor Gabor A. Somorjai, Co-Chair

The self-assembly and optoelectronic properties of model crystalline organic semiconductor films was studied by atomic force microscopy (AFM) techniques. Small molecule organic semiconductors serve as model systems for the active materials in organic electronic devices. Applications such as organic solar cells and light-emitting diodes rely on organic polymers and small molecules for their properties but the performance of these organic devices could still yet be improved compared to the inorganic-based devices. The aim of this work is to study different structure-property relationships in model organic systems to gain a better understanding for designing organic electronic material. Other spectroscopic and structural techniques are used to complement the spatial mapping capability of AFM, providing a more comprehensive view of the fundamental processes governing organic semiconductor films. First, self-assembled oligothiophenes with different surface functionalization are studied for the role humidity has on the electronic properties of a monolayer film. In-situ AFM and x-ray photoelectron spectroscopy (XPS) show that the water vapor is found to change the electronic properties of films with hydrophilic surface termination groups leaving hydrophobic films unaffected. Next, different indigo small molecules are self-assembled at the air-water interface into crystalline structures. The role of intermolecular interactions is found to play a critical role in the indigo crystal morphology. The self-assembled indigo crystals are studied by photoluminescence (PL) spectroscopy revealing the presence of H-aggregate formation during self-assembly. Further studies of the electronic properties of the indigo crystal films are performed using electrical AFM techniques and field-effect transistors. Finally, a scheme for the fabrication of flat field-effect transistors using graphene photolithography is presented. Graphene field-effect transistors are fabricated and tested providing a platform to study more accurately thin organic semiconducting films. This dissertation demonstrates the advantage of studying model systems of organic semiconductors with nanoscale precision with the aim of designing better performing organic electronic devices.

To my parents

Table of contents

Abstract	1
Table of contents	ii
List of figures	iii
Acknowledgments	viii
1 Introduction	1
Abstract	1
1.1 Organic Electronics	2
1.2 Organization of Thesis	5
2 Experimental Methods	6
Abstract	6
2.1 Introduction	7
2.2 Scanning Probe Microscopy	7
2.2.1 Atomic Force Microscopy	7
2.2.2 Conductive Atomic Force Microscopy	9
2.2.3 Kelvin Probe Force Microscopy	10
2.3 X-ray Photoelectron Spectroscopy	13
2.4 Grazing Incidence Wide-angle X-ray Scattering	15
2.5 Photoluminescence Spectroscopy	15
2.6 Langmuir-Blodgett Films	16
3 Influence of Humidity on Electronic Properties of Functional Self-Assembled Oligothiophene Monolayers	17
Abstract	17
3.1 Introduction	18
3.2 Experimental	20
3.3 Results and Discussion	21
3.3.1 Self-assembly of HD4TBA into crystalline monolayers	21
3.3.2 Electronic properties of D5TBA and HD4TBA monolayers	23

3.3.3	Changes in surface potential of HD4TBA and D5TBA with varying humidity	26
3.3.4	Oxygen sensitivity of TD4TBA to water vapor by APXPS	30
3.4	Conclusions	32
4	Self-assembly of Indigo Small Molecules at the Air-Water Interface	33
	Abstract	33
4.1	Introduction	34
4.2	Experimental	35
4.3	Results and Discussion.....	36
4.3.1	EH-Indigo crystallite films	36
4.3.2	EH-Indigo crystallite bundle formation.....	42
4.3.3	EH-Indigo self-assembly with high solution concentration	44
4.3.4	EHT-Indigo film self-assembly	46
4.4	Conclusion.....	49
5	Optoelectronic Active Aggregate Formation in Indigo Films and Graphene Field- Effect Transistors	51
	Abstract	51
5.1	Introduction	52
5.2	Experimental	54
5.3	Results and Discussion.....	55
5.3.1	Optical H-aggregate formation in EH-Indigo and EHT-Indigo Films	55
5.3.2	Conductive AFM and KPFM of EH-Indigo	62
5.3.3	Graphene field-effect transistors	64
5.4	Conclusion.....	68
6	Summary and Outlook.....	69
	Abstract	69
6.1	Summary	70
6.2	Future Directions.....	72
	References	74

List of figures

Figure 1.1 Solar Cell Efficiency Records. ¹⁰	2
Figure 1.2. Common organic semiconductor molecules used in optoelectronic applications. P-type organic semiconductors are shown in the left panel. N-type organic semiconductors are shown in the right panel. ²²	3
Figure 2.1 Typical AFM setup using a cantilever deflection method.....	7
Figure 2.2 Agilent 5500 SPM. (a) The AFM on the isolation block with the glass environmental chamber visible below the scanner head. (b) Detailed view of inside the environmental chamber. The tip (illuminated by a red laser) is in close proximity to the surface of a sample. The metal sample stage contains pins for electrical biasing and grounding the sample.....	8
Figure 2.3. Conductive AFM imaging of a pentathiophene monolayer. (a) Height image of D5TBA monolayer. (b) Current mapping of the area shown in (a) at a sample bias of -3V. Brighter contrast indicates a larger amount of current is measured at that pixel.	10
Figure 2.4. Energy level diagram of the AFM tip and the sample during KPFM operation. (a) Tip and sample are close to one another but not in electrical contact. (b) Tip and sample are in electrical contact. (c) Tip and sample are in electrical contact but a DC voltage is applied to the tip to compensate for the contact potential difference.	11
Figure 2.5. KPFM of a HOPG surface. (a) AFM height image. (b) Contact potential difference image.	12
Figure 2.6. Principle of x-ray photoelectron emission.....	13
Figure 2.7. Ambient Pressure X-Ray Photoelectron Spectroscopy. (a) Beamline 9.3.2 at the Advanced Light Source Berkeley, CA. (b) Differentially pumping and electrostatic focusing of electrons. (c) Schematic of APXPS system found at beamline 9.3.2 with the hemispherical electron energy analyzer shown in yellow. ⁵⁵	14
Figure 2.8. Grazing-Incidence Wide-Angle Scattering X-ray Geometry ⁵⁸	15
Figure 2.9. Langmuir-Blodgett Technique. (a) Pressure-area isotherm showing different phase transitions for a model system of fatty acid molecules. (b) Schematic of the deposition process onto the substrate from the water surface. ⁶⁵	6
Figure 3.1. Molecular structures of oligothiophenes used in this study	19
Figure 3.2. Langmuir-Blodgett surface-pressure isotherms of D5TBA and HD4TBA.....	21
Figure 3.3. AFM height images of oligothiophene monolayers. a) D5TBA and b) HD4TBA on mica.....	22

Figure 3.4. AFM Imaging of mixed D5TBA/HD4TBA monolayers. (a) Height and (b) frequency shift images.	23
Figure 3.5. Conductive AFM imaging of HD4TBA on doped silicon. (a) Height and (b) current map at -1V sample bias.	24
Figure 3.6. UV-Vis absorbance of D5TBA and HD4TBA solutions in chloroform.	25
Figure 3.7. Kelvin probe microscopy of mixed D5TBA/HD4TBA monolayers. (a) Height (non-contact) and (b) work function image calculated from the KPFM surface potential image. HOPG is used as a reference to calibrate the tip work function.	26
Figure 3.8. Kelvin probe force microscopy imaging of HD4TBA under varying humidity. (a) Height image (non-contact) and (b) CPD at 2.9% relative humidity. (c) CPD at 19.6% relative humidity. The CPD images have a color scale of -200meV.	27
Figure 3.9. Contact potential difference of HD4TBA monolayer and the silicon oxide substrate with varying humidity	28
Figure 3.10. Kelvin probe imaging of mixed D5TBA/HD4TBA monolayers under varying humidity. Height and CPD images taken at (a) ~0% RH and (b) 34% RH. (c) Distribution of contact potential difference values in the AFM image.	29
Figure 3.11. Diagram of a D5TBA/HD4TBA mixed film and the work function change of each oligothiophene upon the addition of water vapor.	30
Figure 3.12. Ambient pressure X-ray photoelectron spectroscopy of TD4TBA on gold. a) O1s and b) S2p XPS binding energies in vacuum conditions. (c) O1s and (d) S2p XPS binding energies in 100mTorr of water.	31
Figure 4.1. Indigo functionalized small molecules used in this study	35
Figure 4.2. Langmuir-Blodgett EH-Indigo pressure-area compression isotherm.	37
Figure 4.3. Optical microscope images of EH-Indigo films at deposited on silicon oxide at surface compression value of ~1 mN/m. (a) Scale bar is 500 microns and (b) different region of same film where scale bar is 200 microns.	38
Figure 4.4. AFM imaging of EH-Indigo films at low-compression on silicon oxide. (a) AFM height image of EH-Indigo crystallite film. Scale bar is 5 microns. (b) High resolution image of film. Scale bar is 1 micron.	39
Figure 4.5. EH-Indigo crystallite morphology characterization by AFM. (a) Height image of EH-Indigo crystallites showing layer by layer growth. Scale bar is 500 nm. (b) Height distribution of (a) showing each layer is ~2 nm in height.	39
Figure 4.6. Friction imaging of EH-Indigo crystallites. (a) Height image of EH-Indigo crystallites. (b) Friction force of the corresponding image. Darker areas indicate lower friction. Scale bar in both images is 1 micron.	40

Figure 4.7. EH-Indigo Crystal Structure. (a) GIWAXS pattern of EH-Indigo on silicon oxide. (b) EH-Indigo π - π stacking interaction along the (100) axis. (c) EH-Indigo hydrogen bonding interaction along the (010) axis.	41
Figure 4.8. EH-Indigo macroscale aggregate formation on the water surface at high LB compression (>20 mN/m).....	42
Figure 4.9. Optical microscope images of EH-Indigo bundles formed at surface compression values greater than 20 mN/m. Different regions of the same film on silicon oxide where the (a) scale bar is 500 microns and (b) scale bar is 50 microns.	43
Figure 4.10. AFM imaging of EH-Indigo bundles. (a) and (b) are AFM height images of different regions of a EH-Indigo bundle film on silicon oxide. Scale bar in both images is 4 microns	44
Figure 4.11. EH-Indigo film formed from 2 mg/mL concentration in a pre-compressed Langmuir-Blodgett trough. (a) EH-Indigo film where the scale bar is 500 microns. (b) Zoom in region of the film where the scale bar is 100 microns.	45
Figure 4.12. AFM height image of 2 mg/mL EH-Indigo films on silicon oxide. (a) Height image of a region with a visible crack in the film. (b) High resolution AFM height image of the EH-Indigo film morphology.	46
Figure 4.13. EHT-Indigo Langmuir-Blodgett film self-assembly. (a) Surface pressure-area compression isotherm. (b) Optical microscope image of an EHT-Indigo film on silicon oxide. Scale bar is 200 microns.	47
Figure 4.14. AFM height imaging of EHT-Indigo film on silicon oxide. (a) AFM height of a EHT-Indigo film with a crack present in the film. (b) Region of film with less dense regions of the EHT-Indigo film.	47
Figure 4.15. EHT-Indigo X-ray scattering. (a) GIWAXS pattern of few-layer EHT-Indigo on silicon oxide. (b)-(c) Visualization of crystal structure calculated from GIWAXS of an EHT-Indigo single crystal from a saturated solution in THF.	48
Figure 4.16. EHT-Indigo films on conductive substrates. (a) AFM height image of EHT-Indigo film on highly doped p-type silicon with native oxide. (b) AFM height image of EHT-Indigo film on HOPG.	49
Figure 5.1. Energy diagram of H-J aggregate formation in a molecular dimer system. In J-aggregates the molecule packing is head-to-tail and causes an absorbance and fluorescence redshift. In H-aggregates the packing is face-to-face and the fluorescence shows a blueshift. ¹⁵⁶	52
Figure 5.2. Field-effect transistor geometries for thin organic films. (a) Standard fabrication with bottom-contact source and drain electrodes. The electrodes are typically tens of nanometers in height above the insulator. (b) Coplanar source-drain	

electrodes with the insulating oxide layer. (c) Graphene field-effect transistor with monolayer graphene (~1 nm in height) on top of the insulator layer.	53
Figure 5.3. EH-Indigo solution in chloroform absorbance and photoluminescence spectrum.....	56
Figure 5.4. EH-Indigo crystallite film on silicon oxide. (a) AFM height image. (b) Map of photoluminescence in a different region of the same film. The color intensity scales linearly with photon counts.....	57
Figure 5.5. EH-Indigo crystallite film absorbance and photoluminescence spectrum	58
Figure 5.6. Photoluminescence lifetime of EH-Indigo in solution and EH-Indigo crystallites.....	59
Figure 5.7. Photoluminescence of a concentrated 2 mg/mL EH-Indigo Langmuir-Blodgett film compared with the photophysics of EH-Indigo in solution	60
Figure 5.8. EHT-Indigo film photoluminescence	61
Figure 5.9. KPFM of EH-Indigo crystallite film deposited on bottom-contact field-effect transistors. Height (top) and CPD (bottom) at (a) no bias conditions, (b) 20 minutes after constant -9 V bias applied to the gate, (c) 18 hours after constant -9 V bias applied to gate. For this image the gate bias was turned off and no bias was applied at any electrode.....	62
Figure 5.10. CAFM of EH-Indigo crystallite film. (a) Height image scaled to show the 50 nm gold electrode. (b) Height image scaled to show the thin film of EH-Indigo crystallites. (c) Current image measured with a +5 V bias applied to the gold electrode.....	63
Figure 5.11. Graphene field-effect transistor fabrication process. The photoresist is deposited on the graphene before patterning by UV light and development. Oxygen plasma etches the exposed graphene leaving only the electrode features. Acetone and hydrochloric acid cleans the graphene electrodes and channel regions of silicon oxide.	64
Figure 5.12. Graphene field-effect transistors. (a) Scale bar is 500 microns. (b) Electrode contacts. Scale bar is 100 microns. (c) Stainless steel tubes with copper wire silver pasted on to graphene pads. Scale bar is 500 microns.....	65
Figure 5.13. AFM characterization of graphene after electrode fabrication. (a) Height image of graphene on silicon oxide. (b) Height profile of green line in (a) which shows the step height of graphene is approximately 1 nm. (c) Height image of graphene after 30 minute soak in 1 M hydrochloric acid.	66
Figure 5.14. KPFM characterization of the graphene electrode. (a) Height image showing a crack in the electrode just above the kink. (b) Phase image showing the distinct	

crack. (c) CPD image of the electrode. The bottom half of the electrode is still connected to the voltage source and is biased to a higher potential. 66

Figure 5.15. KPFM of EHT-Indigo on graphene field-effect transistors. (a) Height image of EHT-Indigo thin film deposited on graphene electrodes. (c) CPD image showing different surface potentials of EHT-Indigo in electrical contact with graphene. No bias is applied to the graphene or the gate..... 67

Acknowledgments

First I'd like to acknowledge my Ph.D. advisor, Miquel Salmeron. Your help has been instrumental and you have helped me become a better scientist. Without your direction I would not have reached this point in my career. I would also like to thank Gabor Somorjai for being an additional source of support and guidance throughout the years. I would like to thank both the Salmeron group and the Somorjai group for being good friends and helping me along the way by answering all of the stupid questions I have had. I would especially like to thank Yingjie Zhang, Sara Barja, Cheng Hao Wu, G r me Melaet, Baran Eren and Robert Weatherup. I would also like to thank Tressa Kay Mikel for being a great undergrad student and I hope things go well in your future endeavors.

I would like to acknowledge the great staff and users of the Molecular Foundry. I cannot speak enough about how beneficial my time has been at the Foundry. I spent a large portion of my graduate career in the Foundry and I only have good things to say about the people who walk through those halls. I would like to give special acknowledgement to Alex Weber-Bargioini, Paul Ashby, Virginia Altoe, Ed Wong, Deirdre Olynick, Yi Liu, Babak Sanii, Prashant Kulshreshtha, Bo He, Sebastian Wickenburg, and Nick Borys. I feel awful not naming more people because I feel like there have been so many people who have had a positive influence on my career and life, even if it was simply a chat in the hallway for a few minutes, but it would double the length of this dissertation to name every single person.

I would like to acknowledge the early influences on my chemistry career. Mrs. Gamberale you were instrumental into making me appreciate chemistry in your AP chemistry class in high school. You made me realize chemistry could be fun and in your class I decided that chemistry is something I would pursue in my life. I'm glad you are still teaching and hopefully inspiring future chemists. Professor Michael Sailor thank you for letting me join your research group at UC San Diego and letting me experience first-hand what it meant to do research. You allowed me to fall in love with research and live the life of a chemist. Liz you were the best graduate student mentor an undergraduate student could have and I am sure that if I was assigned anyone else my experience would not have been as great. I am happy I got to spend two and a half years working with you.

I would like to thank all of the friends I have made here in Berkeley, especially in the chemistry department. I have made a lot of great friends and met a lot of people I will cherish forever. Getting a Ph.D. is easy when you enter the program with a great set of people who become close friends over the years. I could also spend pages naming everyone in the department (since I know everyone, obviously) but I hope everyone knows how appreciative I am for being friendly faces around the chemistry complex. I want to thank Andrew A., Andrew N., Anna, Cheri, Frances, Karla, Kelly, Tony, and Richard for being great friends from the beginning. We will always have the river and La Vals. I also want to mention Ben and Sarah, this past year getting to know you has been great and I'm fortunate to have met you.

Lastly and most importantly I'd like to thank my family. To my brother Mike, I am proud to call you my younger brother as you've always been the most caring person I know. To my sister Julia, you are the best older sibling someone could have to look up to.

I hope I achieve as much as you already have and will continue to do so. Mom and dad, thank you for always supporting me. Everything I do is a way of saying thank you for everything you have ever done for me. I will always look up to you.

1 Introduction

Abstract

Organic semiconductors and their electronic applications are introduced in this chapter. A fundamental understanding of how organic semiconductors behave at the molecular level as well as when assembled into a film is essential for achieving high performing devices. The tunability of organic molecules to achieve different energetic states and environmental sensitivity makes organic electronics suitable for applications such as photovoltaics, light-emitting diodes, and sensors. A nanoscale approach to study the structure and optoelectronic properties of low-dimensional model organic films is introduced.

1.1 Organic Electronics

The discovery of new and better materials has led to the constant development of technology. In the last fifty years the use of semiconductors in electronics has revolutionized all facets of society. The physics of a semiconductor are inherent from simple objects such as a transistor to a complicated device such as a solar cell. The research in inorganic semiconductors was followed by the discovery that particular organic molecules could also exhibit semiconducting properties.¹⁻² Since their realization, organic semiconductors have found use in various applications but two primary areas that have driven much of the research is in photovoltaics³⁻⁶ and light-emitting diodes.⁷⁻⁹ Figure 1.1 shows the progression of solar-cell efficiencies in various types of devices. Inorganic semiconductor devices, especially silicon based solar cells, have efficiencies typically above 20% and have served as benchmarks for the field. As one can see, although the field of organic solar cells has developed the efficiency up to approximately 12%, it still lags behind their inorganic counterparts.

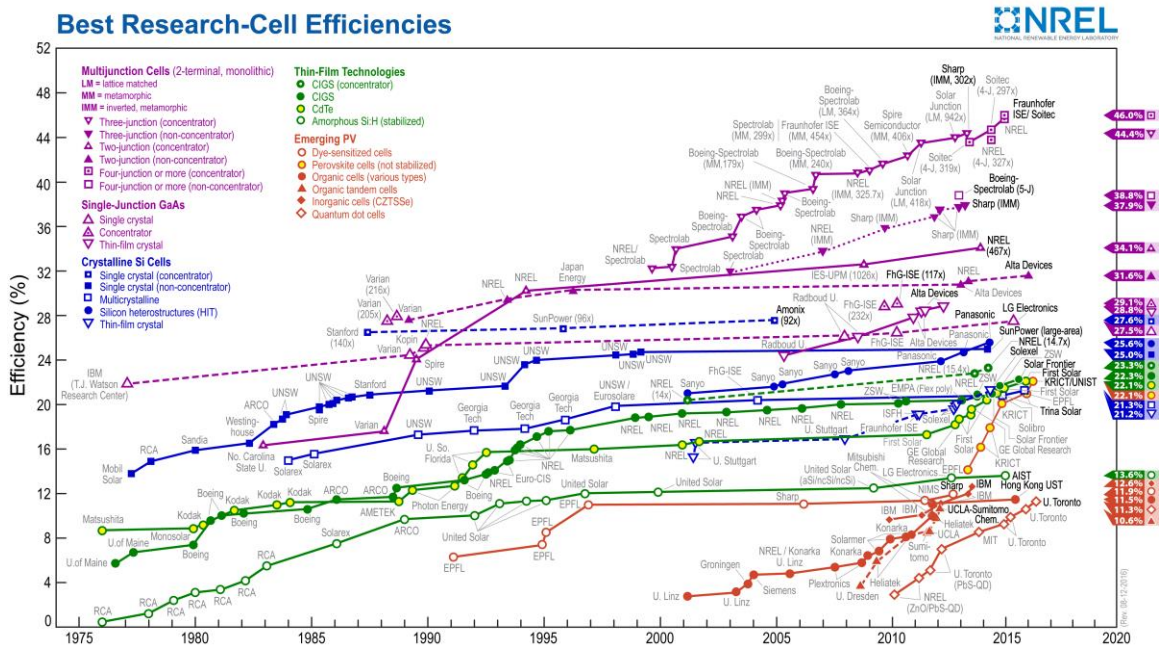


Figure 1.1 Solar Cell Efficiency Records.¹⁰

On the other hand, organic light-emitting diodes have found extensive use in display applications such as televisions and mobile phones and are surpassing fully-inorganic based displays. Furthermore, the mechanical flexibility of organic molecules and polymers is allowing researchers to explore flexible electronic devices.¹¹⁻¹² However, a primary drawback that continues to limit further use of organic semiconductors is the poor charge mobility in organic films compared to inorganic films.

Organic semiconductors exhibit fundamentally different charge transport behavior than inorganic semiconductors. For inorganic semiconductor solids, a band model applies

where there is a delocalization of charge carriers (i.e. electrons and holes).¹³ Band transport results in crystalline silicon having an electron mobility of $1400\text{cm}^2\text{V}^{-1}\text{s}^{-1}$ and hole mobility of $450\text{cm}^2\text{V}^{-1}\text{s}^{-1}$. Organic semiconductors on the other hand do not have fully delocalized charge carriers but rather the charge is localized and hops to neighboring semiconducting molecules during transport.¹⁴⁻¹⁶ For comparison, a rubrene single crystal only has a hole mobility of $40\text{cm}^2\text{V}^{-1}\text{s}^{-1}$.¹⁷ However, organic semiconductors have significant advantages over inorganic materials. Specifically the widespread field of organic synthesis means organic semiconductors can be tuned synthetically which is not as simple with inorganic crystals.¹⁸ Synthetic developments have yielded different functional groups that make a molecule inherently p-type¹⁹ and n-type.²⁰⁻²¹

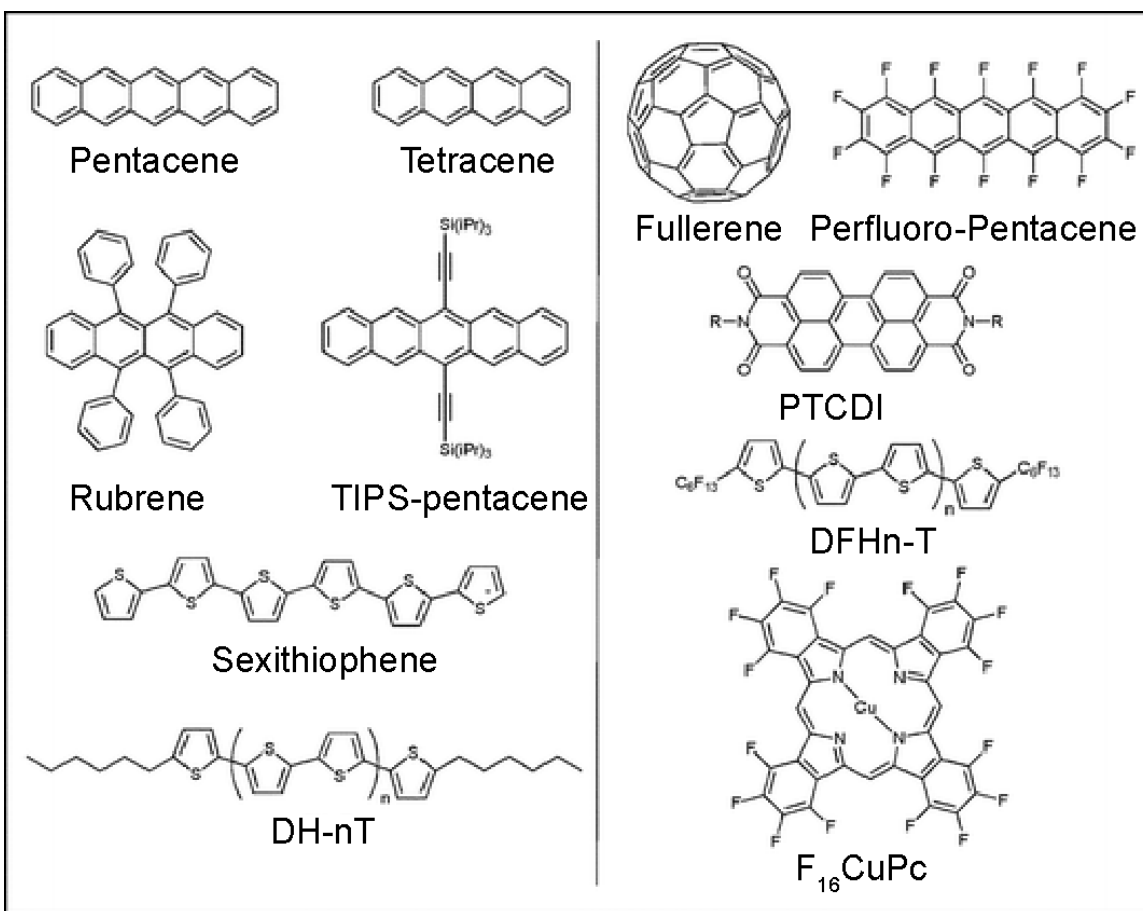


Figure 1.2. Common organic semiconductor molecules used in optoelectronic applications. P-type organic semiconductors are shown in the left panel. N-type organic semiconductors are shown in the right panel.²²

Figure 1.2 shows commonly used organic semiconductor molecules. Fundamental to all of the examples is a conjugated π -system that can be further “doped” by oxidation/reduction to remove/add delocalized electrons. P-type semiconductors are electron deficient species where the hole is the charge carrier, and n-type are electron rich species where the electron is the charge carrier. The synthetic tunability of molecules directly leads to the tunability of optical and electronic properties. Different chemical

groups on the conjugated system will modify the energetic levels of the highest occupied molecular orbital (HOMO) and the lowest unoccupied molecular orbital (LUMO) which determines the bandgap of the molecule. The molecular structure also plays an important role in the self-assembly of the molecule into a film and the reactivity of the molecule/film to other molecules.

The importance of self-assembly for organic electronics can be understood by examining the intermolecular interactions between two molecules in an active layer. For a specific electronic application there is inherently a preferential geometry or structure to the active organic film. For example, in an organic field-effect transistor, the active organic layer must efficiently conduct charge across the film between electrodes. The conductivity depends on how efficient the charge hopping is between hopping sites in the film which is itself highly dependent on how well the molecules pack together (i.e. single-crystal films exhibit higher mobilities than amorphous films).²³ Thus the structure-property relationship in organic semiconductor films is a critical aspect of research to investigate and finding the most effective processing methods is important for the realization of better performing organic electronic devices. Different techniques exist to form organic films. Solution based techniques such as spin coating or dip coating have significant drawbacks in achieving highly conductive films. Since the self-assembly process is driven primarily by weak forces such as van der Waals interactions, small variations in solvent evaporation rate or concentration can lead to defects and grain boundaries in the film which decrease performance.²⁴⁻²⁵ To achieve single crystals of organic semiconductors the most common method is solution growth or physical vapor deposition.¹⁷ To study the inherent structure-property relationship it is also important to study model systems where the molecular packing is ordered and easily resolvable. For this purpose self-assembled monolayers or few-layer films are ideal.

It is also important to consider the chemical nature of organic semiconductors. Inorganic semiconductors such as silicon or gallium arsenide typically show a fair amount of inertness in their optical and electronic properties to moderate environmental changes. This is not true for organic semiconductors as the HOMO/LUMO levels are energetically capable of causing a chemical reaction with elevated temperature or the presence of other chemicals present in the atmosphere such as water molecules. However, this opens an important area for study in the field of sensors. Organic molecules can be highly tuned to be chemically reactive to specific molecules, or analytes, and an organic film can be used as a sensor for both gaseous and liquid species.²⁶⁻²⁸ In sensors typically a bulk signal is measured that is composed of multiple receptor-analyte interactions. Molecular understanding of the analyte binding event and the influence it has on the local electronic properties of a semiconductor is important for the design of higher performing organic sensors as a stronger local interaction typically causes a larger bulk signal that can be measured.

Scanning probe microscopy has revolutionized our understanding of the nanoscale properties of semiconductor films. In addition to measuring mechanical properties²⁹, atomic force microscopy has allowed researchers to study a variety of optoelectronic properties in organic semiconductor films including but not limited to local

conductivity³⁰⁻³², photoconductivity³³⁻³⁴, and work function heterogeneity.³⁵⁻³⁷ These nanoscale spatial measurements enable researchers to correlate the nanoscale structure of an organic semiconductor film with the local property that would otherwise be averaged out if only bulk measurements are performed. Electronic properties such as conductivity depend greatly on nanoscale defects or grain boundaries in organic films and techniques with nanoscale spatial resolution are necessary to characterize why these defects cause a loss in performance.³⁸⁻³⁹ To study the fundamental structure-property relationship in organic semiconductor films it is advantageous to use model systems. Monolayers or few-layer films are ideal because they are better characterized by atomic force microscopy but also reflect the properties that exist in bulk films used for actual devices. In this thesis crystalline monolayers and few-layer films are studied to understand how the structure and packing of the individual organic molecules define the optoelectronic properties of the film.

1.2 Organization of Thesis

This chapter is a brief background on organic electronics and the organic molecules within the active layers in devices. The properties of organic semiconductors are discussed and a methodology of how to study the structure-property relationship at surfaces and in low-dimensional organic materials is presented. Chapter two gives a detailed overview of the experimental techniques used for the different studies in this thesis. Specifically, scanning probe techniques based on atomic force microscopy are presented as well as some secondary techniques to complement the spatially resolved images obtained from scanning probe measurements. Studies of environmental effects on oligothiophene monolayers are presented in Chapter three. A functionalized hydroxyl terminated oligothiophene monolayer that is sensitive to humidity changes is contrasted with an inert methyl terminated oligothiophene monolayer. The hydroxyl terminated monolayer is shown to exhibit changes to the film electronic properties as a function of humidity while the same changes are not observed in the inert monolayer. Chapter four introduces a class of organic semiconductor molecules based on the indigo functional group. Two indigo semiconductors are studied for their self-assembly into crystalline films. The structures of the two films are determined and the competition of different intermolecular interactions is shown to yield unique anisotropic and isotropic geometries. Chapter five studies the optical and electronic properties of the indigo films developed in chapter four. Optical aggregates are shown to exist in crystalline indigo semiconductor films also yielding electrical conductivity between distinct indigo crystallites. In addition, a graphene electrode fabrication scheme is presented to achieve flat field-effect transistors. Finally, chapter six summarizes the results in the thesis and presents an outlook on the future direction of the research.

2 Experimental Methods

Abstract

This chapter will present an overview of the experimental techniques used in this dissertation. Primary focus will be given to imaging nanoscale properties using scanning probe techniques. Also, additional characterization tools that are used such as x-ray photoelectron spectroscopy, transmission electron microscopy, and grazing incidence wide-angle x-ray scattering will be briefly discussed. Photoluminescence spectroscopy and Langmuir-Blodgett films will be discussed in the context of organic semiconductor films in this dissertation.

2.1 Introduction

Probing optoelectronic properties on the nanoscale can be accomplished by utilizing scanning probe techniques such as AFM (atomic force microscopy), CAFM (conductive atomic force microscopy), and KPFM (kelvin probe force microscopy). The resolution of these AFM techniques is determined by the tip which is typically 10-20nm. In addition to structural information, these techniques can simultaneously give chemical and electronic information on length scales up to micrometers. The atomic and molecular scale energetics can be resolved using XPS and photoluminescence measurements. And in addition, x-ray scattering can show atomic and molecular level structural information. Temporal information of organic semiconductor charge behavior can be obtained using time-resolved photoluminescence spectroscopy. Principles of scanning probe, XPS, photoluminescence, and other techniques will be discussed in detail.

2.2 Scanning Probe Microscopy

2.2.1 Atomic Force Microscopy

Atomic force microscopy (AFM) is utilized in all of the research presented in this work due to the ability to perform measurements with high spatial resolution. AFM has become ubiquitous in probing nanoscale properties since its invention in 1985.⁴⁰⁻⁴¹ While many optoelectronic materials are suitable for study by STM due to their conductive nature, the AFM is typically more practical and has the advantage of being able to probe multiple forms of properties of a material at once. Furthermore AFM has been steadily developed and is currently capable of obtaining the highest resolution images of surfaces and molecules when utilized in ultra-high vacuum.⁴²⁻⁴⁵ Most commercial AFM instruments measure surface topography by using a cantilever with a sharp tip at the end to probe the surface. As the tip encounters different features the cantilever will deflect to compensate and this deflection can be monitored by a laser and photodiode (Figure 2.1). The vertical deflection of the cantilever is measured with a laser to obtain the height of the sample whereas the lateral deflection is a measure of the lateral force and is related to the friction of the surface.

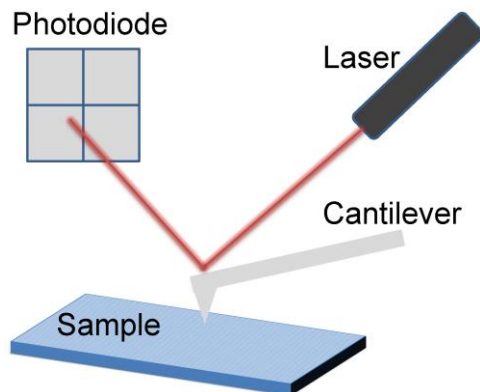


Figure 2.1 Typical AFM setup using a cantilever deflection method

The AFM used here is an Agilent 5500 SPM commercial system (Keysight Technologies, Santa Rosa, CA, USA) with no further modifications and shown in Figure 2.2. A 10 micron scanner head was used to ensure the highest spatial resolution possible. Nevertheless a larger scanner head is available for the system if necessary. A significant advantage for the Agilent 5500 system is that the sample is fixed on the stage through either magnetic attachment or adhesives and the tip performs the raster scan. Tip-scan usually results in better drift control and lowering the contribution of mechanical noise. To minimize the noise from vibrations, the AFM resides on a 20kg block hung by bungee cords to the roof of an acoustically isolated chamber. Most AFM setups utilize vibration isolation tables or dampening legs for the table to minimize vibration but bungee cords and hanging the instrument from above is also suitable. With this form of isolation, lattice resolution of atomically flat surfaces (e.g. mica) is routinely obtained. A 1mW laser with a wavelength of 670 nm is used for monitoring the cantilever deflection. The enclosure allows for complete darkness of the sample so there is no stray light to interfere with the deflection signal of the AFM.

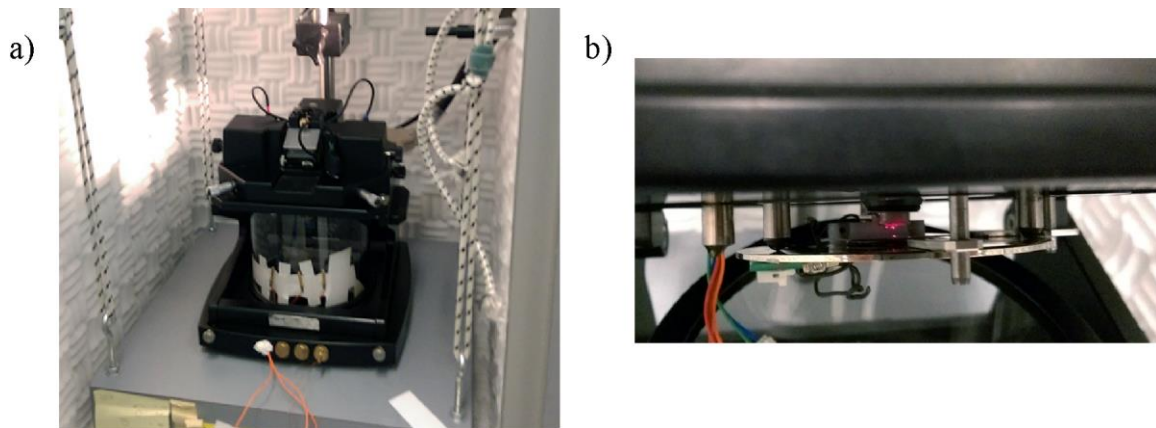


Figure 2.2 Agilent 5500 SPM. (a) The AFM on the isolation block with the glass environmental chamber visible below the scanner head. (b) Detailed view of inside the environmental chamber. The tip (illuminated by a red laser) is in close proximity to the surface of a sample. The metal sample stage contains pins for electrical biasing and grounding the sample.

When measured in contact mode, a silicon cantilever with a small spring constant (~ 0.2 N/m) is used and the tip is scanned across a stationary sample using a constant force ($\sim 1-10$ nN). The deflection of the cantilever is measured and converted through calibration to give a topography image with sub-nanometer precision. However, contact AFM is prone to heavy tip wear and induces sample damage in soft materials so the use of contact AFM was minimal to when either conductive AFM was performed or lateral force information was necessary. Unless noted, tapping mode AFM and non-contact AFM are used in these experiments for topography images. In both modes the tip is oscillated at a resonant frequency and the amplitude of the oscillation is used as the feedback mechanism. For tapping mode, large amplitudes ($\sim 40-80$ nm) are used with the set point frequency just below the resonant frequency. For non-contact mode, the frequency was set to be either on resonance or slightly higher than resonance with very small amplitudes ($\sim 10-20$ nm). Tapping mode AFM was performed with silicon cantilevers with a resonance frequency

typically of 300 kHz and non-contact AFM cantilevers typically had a resonance frequency of 70 kHz. Due to the Agilent 5500 system being in an enclosed glass chamber, it was possible to measure samples under different gaseous environments. The majority of measurements were performed under dry nitrogen and a measured relative humidity of ~0.4%. The lack of a moisture layer on the sample surface or tip typically improved the stability and spatial resolution.⁴⁶⁻⁴⁷

2.2.2 Conductive Atomic Force Microscopy

A metal coated tip can be used instead of inert silicon to measure the current flow between a conductive sample and the tip in a mode called conductive atomic force microscopy (CAFM). In CAFM the tip is in constant contact with the sample and current can flow between the sample and tip. The current is recorded at each pixel that topography is measured and a simultaneous image of current is obtained alongside height and friction. The sensitivity of the CAFM is typically in the femtoamps region and can reach values up to a microamp; however these extremes are usually avoided due to signal-to-noise issues and material degradation respectively. Most measurements are performed with a pico- or nano- level of current. The conductive tips most commonly used for CAFM are platinum coated silicon tips where the platinum layer is 10-25 nm. While suitable for most applications, these tips are susceptible to wear and the platinum coating often times is removed during imaging leading to an insulating tip and the loss of current flow. A more expensive but more suitable alternative is a solid platinum probe. These probes and cantilevers are fabricated with no underlying silicon material and are conductive throughout so that if any tip wear occurs the tip should stay conductive.

In the Agilent 5500 system, a positive or negative voltage can be applied to the tip or sample. Whichever one is chosen for biasing, the other is held at ground and current measurements are collected at each pixel. Due to the decrease of image quality when using a tip bias, the sample is the component most commonly where the voltage is applied. To obtain a current map of a semiconducting organic material as shown in Figure 2.3, the substrate must be carefully chosen. A highly conductive substrate must be used, such as a metal (e.g., gold, copper, etc.) or a highly-doped silicon wafer (0.0005-0.001 $\Omega\cdot\text{cm}$) with only a thin native oxide. Figure 2.3 shows an image of an oligothiophene monolayer on highly doped silicon with a native oxide and Figure 2.3b shows the current image where the oligothiophene film is brighter (more current) than the substrate underneath, this is due to lateral charge transport to neighboring molecules which thus provides a larger electrical contact area. The spatial resolution is higher in the height image (Figure 2.3a) however the current image accurately can depict the morphology of the film. Typical resolution for CAFM can be 50-100 nm if a sharp tip is used and the material does not degrade during the measurement. However, organic materials are susceptible to degradation due to oxidation during current flow and most measurements should be done with as small of a bias as possible. Furthermore, the conductivity of thin films (<20 nm) can decrease with a higher imaging mechanical force from the tip because the conducting pathway is dependent on precise molecular orbital overlap which can be disrupted by pushing on the molecules.⁴⁸

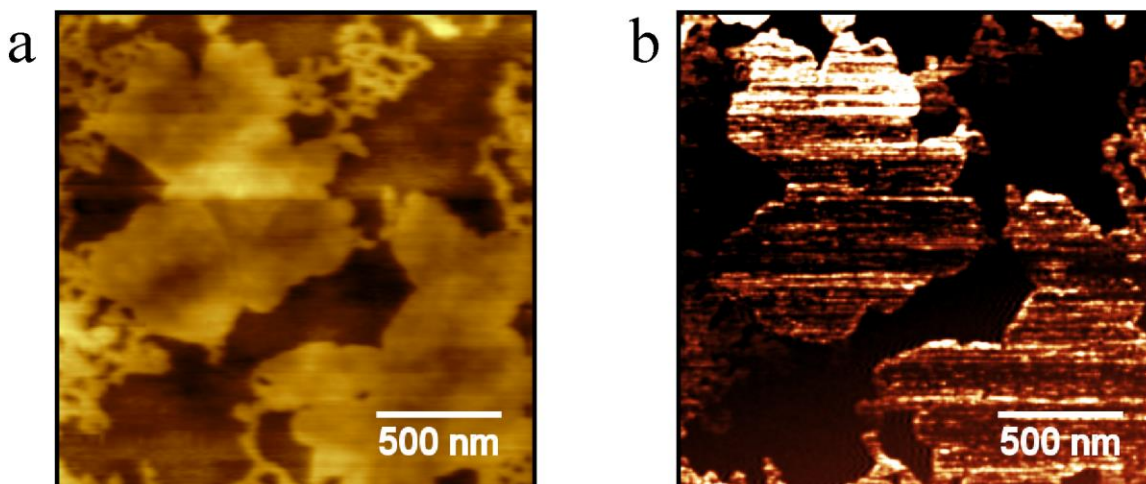


Figure 2.3. Conductive AFM imaging of a pentathiophene monolayer. (a) Height image of D5TBA monolayer. (b) Current mapping of the area shown in (a) at a sample bias of -3V. Brighter contrast indicates a larger amount of current is measured at that pixel.

2.2.3 Kelvin Probe Force Microscopy

Kelvin probe force microscopy (KPFM) measures the local contact potential difference (CPD) between a conductive AFM tip and the surface.⁴⁹ By mapping the local CPD, one can obtain the surface potential or work function of a surface with high spatial and energetic resolution. KPFM can have an energy resolution of 5-20 meV and a spatial resolution that is approximately the AFM tip radius.⁵⁰ Further development has led to the imaging of the charge distribution in a single molecule on a surface in ultra-high vacuum.⁵¹ This is a significant advantage over Kelvin Probe and photoelectron spectroscopy which while having the possibility of excellent energy resolution have little spatial resolution.

In a typical KPFM experiment a platinum coated tip is used in non-contact AFM mode to measure simultaneously topography and the contact potential difference of a conductive or semiconducting sample. One critical aspect of KPFM is for the tip and the surface to not be in contact like in CAFM. Figure 2.4 shows an energy level diagram of an example surface and tip during KPFM operation when the work function of the surface and the tip are different. Figure 2.4a shows the situation where the tip is not in contact and furthermore there is no electrical contact between the tip and sample. Because the fermi levels are different, in Figure 2.4b when the samples are placed in electrical contact current flows and the fermi levels will line up. In this situation the vacuum energy levels are no longer the same and a CPD voltage would form between the sample and the tip. KPFM operates by applying the same magnitude CPD but opposite direction to the tip or sample so that the electrical force can be nullified.

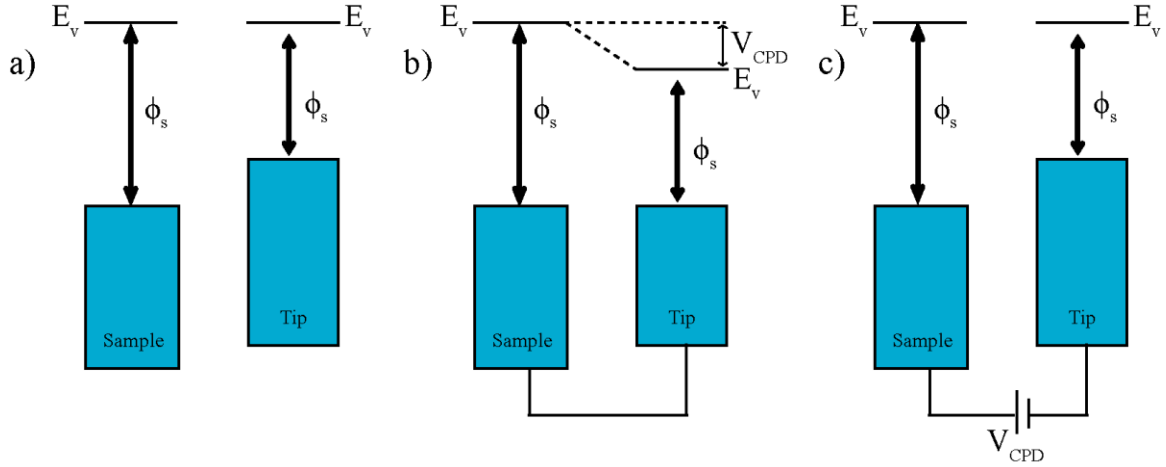


Figure 2.4. Energy level diagram of the AFM tip and the sample during KPFM operation. (a) Tip and sample are close to one another but not in electrical contact. (b) Tip and sample are in electrical contact. (c) Tip and sample are in electrical contact but a DC voltage is applied to the tip to compensate for the contact potential difference.

To measure the CPD of the surface using KPFM, first an AC voltage (V_{AC}) is applied to the tip with a frequency ω to be used as a reference signal. In addition, a DC voltage (V_{DC}) is applied to the tip. The total voltage difference between the sample and the tip is given by

$$V = (V_{DC} - V_{CPD}) + V_{AC} \sin(\omega t)$$

KPFM can be modeled using a parallel plate capacitor model and the electrostatic force can be defined as

$$F = F_{DC} + F_{\omega} + F_{2\omega}$$

where the ω and 2ω are from the AC oscillation placed on the tip. The force can be broken up into its three components

$$F_{DC} = -\frac{\delta C}{\delta Z} \left[\frac{1}{2} (V_{DC} - V_{CPD})^2 \right]$$

$$F_{\omega} = -\frac{\delta C}{\delta Z} (V_{DC} - V_{CPD}) V_{AC} \sin(\omega t)$$

$$F_{2\omega} = -\frac{\delta C}{\delta Z} \frac{1}{4} V_{AC}^2 [\cos(2\omega t) - 1]$$

A lock-in amplifier is used to measure the V_{CPD} by measuring the F_{ω} component of the electrostatic force on top of on the mechanical tip oscillation. When a V_{AC} with a frequency ω is applied to the tip it is overlaid with the mechanical oscillation of the tip used for topography. The lock-in amplifier outputs a voltage (V_{DC}) such that the lock-in output nullifies the F_{ω} at every pixel and this V_{DC} is the negative value of V_{CPD} .

There are two primary ways to measure CPD by KPFM, amplitude modulation (AM) and frequency modulation (FM). In AM, the F_{ω} is measured from the cantilever amplitude directly and the V_{DC} is applied to nullify the amplitude. In FM the frequency shift of F_{ω} is measured and V_{DC} is applied to nullify the frequency shift. Because FM measures the electrical gradient rather than the electrostatic force, FM typically produces higher spatial resolution and thus is preferred to AM. In this work, FM-KPFM is performed with the Agilent 5500 system with the addition of a HF2LI Lock-in Amplifier from Zurich Instruments (Zurich Instruments AG, Switzerland). A modulated bias of 2V at 2 kHz was applied to the tip and a proportional-integral-derivative (PID) controller was used to add a DC bias to the tip to maintain the phase of the 2 kHz signal constant. In addition, the absolute work function of a sample can be determined by first measuring a calibration sample to obtain the work function of the AFM tip. In Figure 2.5a the AFM height image of highly oriented pyrolytic graphite (HOPG) is shown and the simultaneously obtained CPD image is shown in Figure 2.5b.

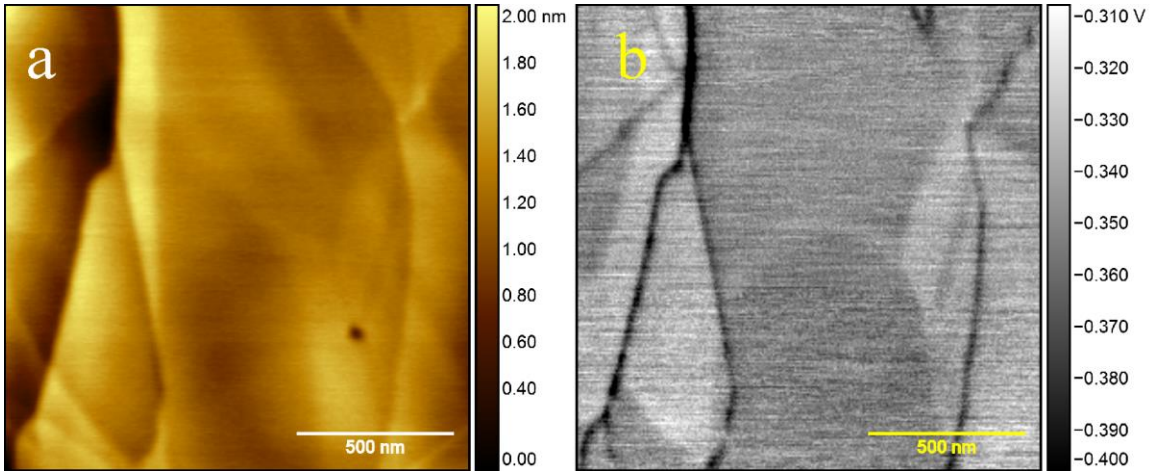


Figure 2.5. KPFM of a HOPG surface. (a) AFM height image. (b) Contact potential difference image.

The work function of HOPG is assumed to be constant with a value of 4.6eV.⁵² Calculating the work function of the platinum/titanium tip gives a tip work function of ~4.3eV. While further measurements with the same tip will yield the work function of a material, one must take care to not change or contaminate the AFM tip in between measurements. Any material picked up by the tip will change the contact potential difference between the new tip apex, with the new contamination material, and the surface. The new tip work function is unknown in this case and an absolute work function cannot be accurately determined.

2.3 X-ray Photoelectron Spectroscopy

X-ray photoelectron spectroscopy (XPS) is a technique used to probe material composition that has proven very successful since its invention in the 1950s.⁵³ The principle of XPS is based on the photoelectric effect where when a material is irradiated with high energy photons, that material will emit electrons with a characteristic kinetic energy

$$E_{\text{kinetic}} = h\nu - E_{\text{binding}} - \Phi_{\text{analyzer}}$$

where $h\nu$ is the incident photon energy, E_{binding} is the binding energy of a core or valence electron, and Φ_{analyzer} is the work function of the analyzer. Each element has distinct core level binding energies and so a XPS spectrum for a given material will show distinct peaks at specific energies corresponding to the elements present and their abundance in the material. A schematic of the emission of an electron from a core level during a XPS experiment is shown in Figure 2.6.

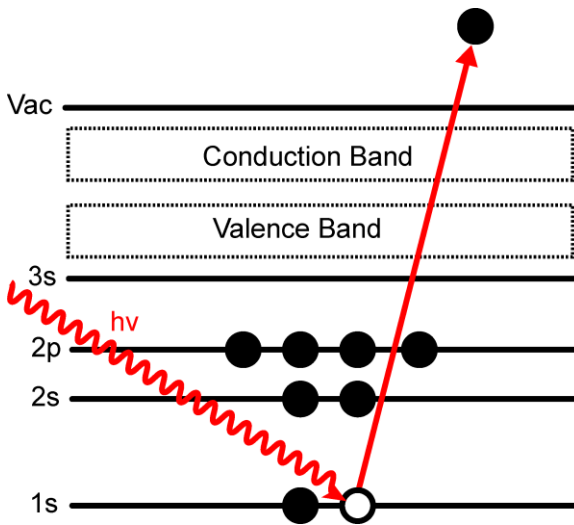


Figure 2.6. Principle of x-ray photoelectron emission

In Figure 2.6 the 1s electron is emitted into the vacuum from the material. The 1s electron would have a kinetic energy that is dependent on the incident energy which would be measured by the analyzer. Typical x-ray sources in a laboratory XPS are aluminum (photon energy ~1487 eV) and magnesium (photon energy ~1254 eV). The incident energies are high enough to probe a variety of core levels encompassing the s-block, p-block, and d-block elements. In addition, because of the small inelastic mean free path of electrons in solids, XPS is inherently a surface sensitive technique where the probing depth of a material is on the order of ~1-10 nm. However, due to electrons scattering with gases, XPS historically is an ultra-high vacuum technique and most of the published studies are of surfaces in vacuum conditions.

In the past fifteen years, extensive technological developments have been made making XPS measurements in moderate pressure conditions possible.⁵⁴⁻⁵⁶ Ambient

pressure x-ray photoelectron spectroscopy (APXPS) setups are now ubiquitous at synchrotron facilities such as the Advanced Light Source in Berkeley, CA (Figure 2.7a). Typical laboratory XPS instruments operate with a pressure differential between the analyzer and sample chamber that is small (from $\sim 10^{-10}$ to $\sim 10^{-8}$ Torr). The addition of a differential pumping system and electron focusing lenses (Figure 2.7b and Figure 2.7c) allows one to have multiple order of magnitude pressure differentials so that the sample can be in gaseous environments with pressures as high as 10 Torr while keeping the analyzer pressure in the 10^{-10} Torr range. Gases such as CO, CO₂, N₂, and H₂O can be introduced using leak valves in a controlled fashion while simultaneously recording the XPS spectrum of a material. Thus it is possible to compare a XPS spectrum in the presence of gas species to that in ultra-high vacuum conditions. Any chemical change due to the gaseous species will result in a change to the oxidation state of particular atoms. However it should be noted that when organic films are measured, beam damage is a significant problem and should be avoided when at all possible.⁵⁷

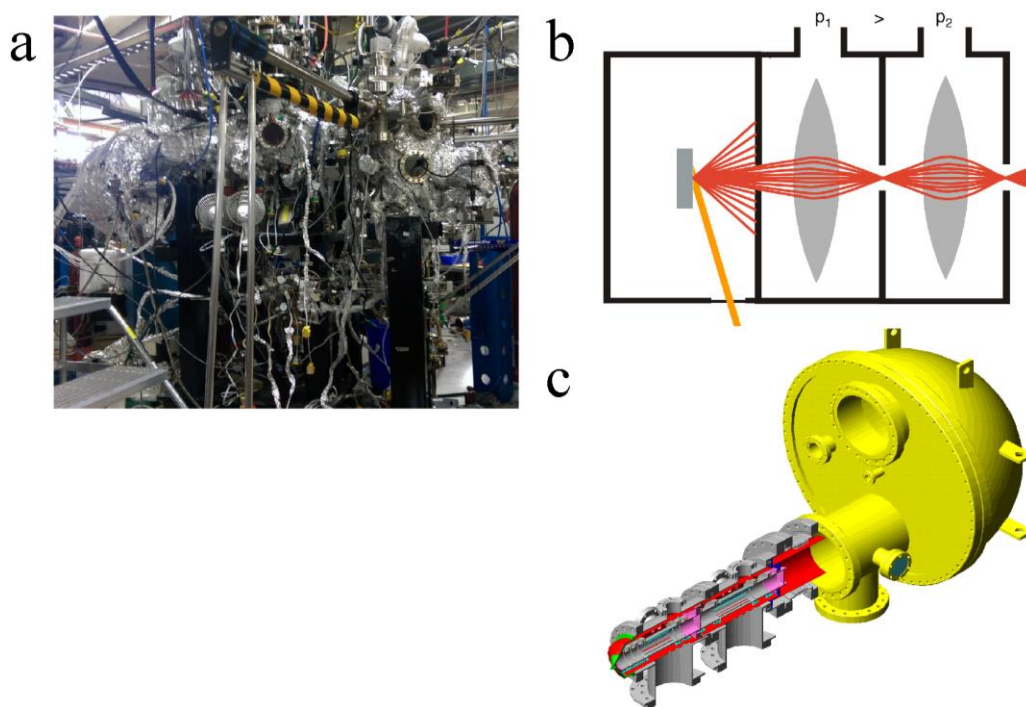


Figure 2.7. Ambient Pressure X-Ray Photoelectron Spectroscopy. (a) Beamline 9.3.2 at the Advanced Light Source Berkeley, CA. (b) Differentially pumping and electrostatic focusing of electrons. (c) Schematic of APXPS system found at beamline 9.3.2 with the hemispherical electron energy analyzer shown in yellow.⁵⁵

2.4 Grazing Incidence Wide-angle X-ray Scattering

Scattering techniques have proven to be highly successful in measuring the micro- and nano-scale structures in organic systems. While transmission is the most commonly used geometry with both x-ray and electron scattering, a reflection, or grazing-incidence, geometry is a useful alternative to measure organic thin films.⁵⁸ An example experimental setup is shown in Figure 2.8. The incident beam of x-rays is sent at the sample with a shallow angle α_i that is commonly below 1° . With grazing-incidence wide-angle scattering (GIWAXS) it is possible to probe the orientation of the local crystallinity in an organic molecular film in three-dimensions for very thin films. Specifically, monolayer or few-layer films of semiconductors are well suited for GIWAXS due to the inherent thickness of such samples. GIWAXS measures the scattering in-plane (xy -axis) as well as out-of-plane (z -axis).

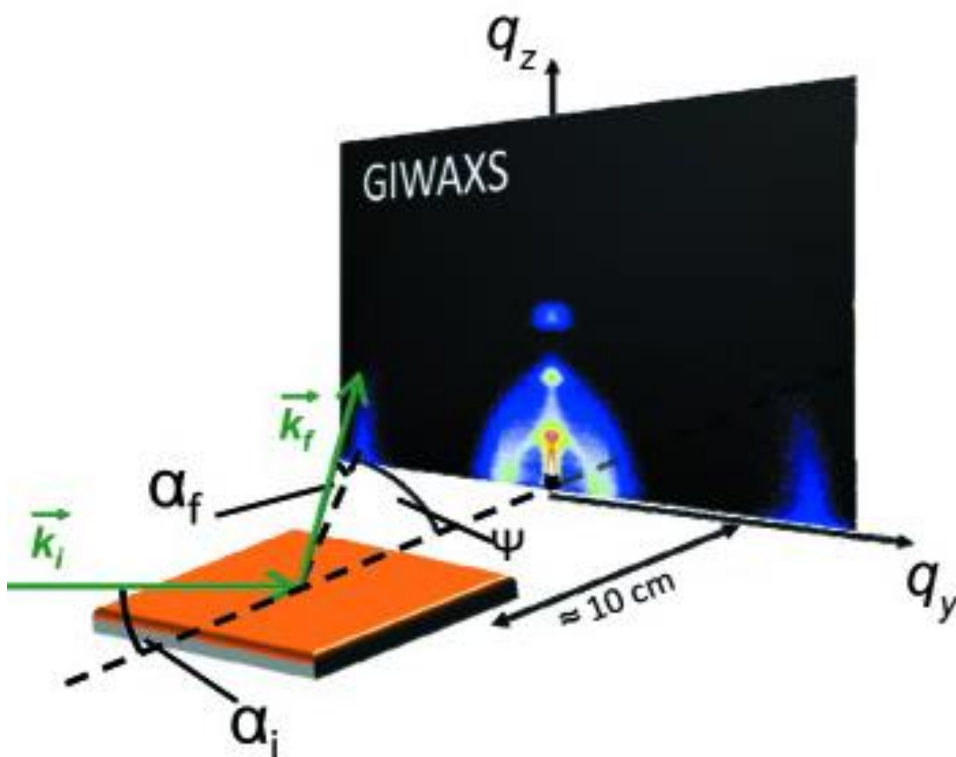


Figure 2.8. Grazing-Incidence Wide-Angle Scattering X-ray Geometry⁵⁸

2.5 Photoluminescence Spectroscopy

Photoluminescence is the process of light emission from a material after absorption of photons from another light source. For organic molecules, photoluminescence is a combination of fluorescence and phosphorescence. Upon light excitation, if the photon emission occurs from two singlet states the process is called fluorescence and if the emission occurs from a triplet state and a singlet state the process is called

phosphorescence.⁵⁹ Organic semiconductors, especially those used for photovoltaics, typically absorb light in the visible range (~400-800nm) and so commercial laser systems are well suited for the study of the photophysics of organic films. Inorganic diode lasers are the most commonly used excitation source due to the vast amounts of wavelengths that are accessible. And by utilizing a motor-controlled stage on a confocal microscope with laser excitation one can easily obtain spatial images of light emission from films⁶⁰ to even single molecules.⁶¹ Furthermore, time resolved photoluminescence measurements gives information about the charge carrier dynamics. By measuring the photoluminescence of a material after excitation over a period of time one can obtain the fluorescence lifetime of an organic molecule which can typically range from picoseconds to nanoseconds.

2.6 Langmuir-Blodgett Films

The Langmuir-Blodgett (LB) technique was developed by Irving Langmuir and Katharine Blodgett.⁶² It has since been extensively used by various fields to form stable organic and inorganic films that can be transferred to different substrates for different experiments.⁶³⁻⁶⁵ The main principle of LB film deposition is to deposit a solution of molecules on the water surface and to use barrier compression to pack the molecules into an ordered film. The surface pressure is continuously monitored using a Wilhelmy plate and molecular behavior can be followed for the presence of phase transitions or morphology changes to the film during compression. An idealized isotherm is shown for fatty acid molecules in Figure 2.9a. The deposition occurs with a solid substrate that is vertically submerged in the water. The substrate is moved vertically out of the water while a film of molecules is deposited onto the substrate at the water meniscus (Figure 2.9b).

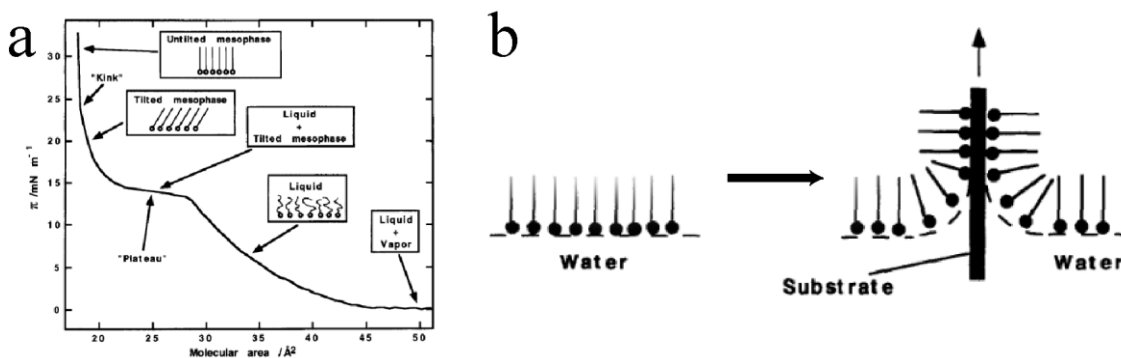


Figure 2.9. Langmuir-Blodgett Technique. (a) Pressure-area isotherm showing different phase transitions for a model system of fatty acid molecules. (b) Schematic of the deposition process onto the substrate from the water surface.⁶⁵

3 Influence of Humidity on Electronic Properties of Functional Self-Assembled Oligothiophene Monolayers

Abstract

The influence of surface group functionalization on the electronic properties of an oligothiophene monolayer was investigated in this chapter. Using Langmuir-Blodgett a quaterthiophene functionalized with a hydroxyl group can self-assemble into crystalline monolayer islands at the air-water interface. The hydrophilic hydroxyl termination is contrasted with a hydrophobic methyl terminated pentathiophene monolayer. The addition of the hydroxyl group does not significantly change the self-assembly behavior producing similar crystalline structures at the air-water interface. The reduction of the semiconducting core to four thiophene groups and the addition of a hydroxyl group reduced the work function of the monolayer as measured by kelvin probe force microscopy. While the surface potential of the methyl terminated shows no change with varying humidity, water adsorption to the hydroxyl terminated film is observed using kelvin probe force microscopy. Ambient-pressure x-ray spectroscopy is used to better understand the localization of water adsorption on the monolayer. Water molecules at low pressure prefer to adsorb onto hydrophilic groups and adsorption onto thiophene groups is not observed as expected. The functionalization of organic electronic material plays a key role in determining how sensitive the electronic properties of the device will be to environmental effects during operation.

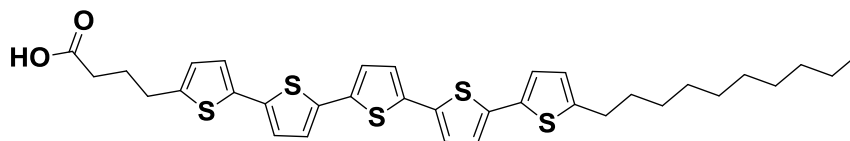
3.1 Introduction

Polythiophenes have been one of the most commonly used and studied conductive polymers since the early 1980s.⁶⁶⁻⁶⁹ The success of poly(3-hexylthiophene-2,5-diyl) (P3HT) in polymeric solar cells and organic field-effect transistors (OFETs) has lead researchers to investigate fundamental charge transport properties of thiophene-based films in the hopes of improving device performance.^{18, 23} Much of this research has been driven by studies of organic semiconductor small molecules. The important advantage of studying small molecules and oligomers is that it allows researchers to study systems that are better defined structurally, enabling more accurate structure-property correlations to be understood compared to their polymeric equivalent.⁷⁰⁻⁷¹ Oligothiophenes have been extensively studied for their behavior in self-assembly⁷²⁻⁷³, donor-acceptor systems⁷⁴, and charge-transport in field effect transistors⁷⁵⁻⁷⁷. Furthermore, the synthetic flexibility of thiophene molecules allow researchers to use thiophene oligomers and polymers in organic sensor applications.⁷⁸⁻⁷⁹ One can tailor the chemical sensitivity of the thiophene film while preserving the high crystallinity and conductivity of the thiophene herringbone crystal packing. While sensor applications often times utilize thick films to obtain a high enough signal to measure in a device, model sensors can be studied using monolayers and thin films. The high crystallinity that results from solution phase self-assembly makes oligothiophenes useful model systems for studying organic electronics and sensors.

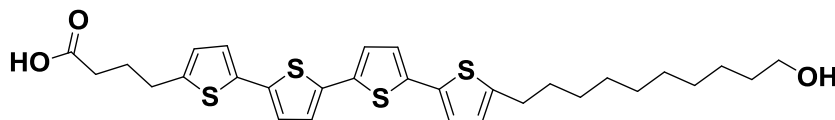
Thiophenes found an early use in Langmuir-Blodgett (LB) film assemblies due to the synthetic feasibility of synthesizing amphiphilic oligomers.⁸⁰⁻⁸² However, unlike other amphiphilic small molecules where the LB compression force can help form the molecular film, thiophenes often do not require any external force to form a crystalline monolayer at the air-water interface.⁸³ The thiophene π - π interaction⁸⁴⁻⁸⁵ is strong enough to induce crystal nucleation upon solvent evaporation and propagate crystal growth locally around the nucleation center. The oligothiophene crystal growth is governed by effects such as choice of solvent, concentration, and temperature. What is of interest for the purposes of organic electronics is that crystals that self-assemble at the air-water interface can be transferred to solid substrates without losing structural integrity.⁸³ Although in-situ studies of the organic monolayer at the air-water interface are possible, preserving the exact crystal packing on the solid substrate as that on the air-water interface allows researchers to use conventional techniques to probe the true self-assembled structure-property relationship of oligothiophenes. Techniques such as conductive atomic force microscopy (CAFM) and kelvin probe force microscopy (KPFM) are well suited to study highly crystalline organic monolayers for their electronic properties. CAFM can study the charge transport behavior within the monolayer while KPFM is sensitive to the work function heterogeneity of the film.

In this chapter, the role of surface terminal functional groups on the electronic properties of similar oligothiophene monolayers was studied using CAFM and KPFM. The use of oligothiophene monolayers for sensor application relies on the ability of the monolayers to be sensitive to environmental changes and preserving their conductive nature. Different oligothiophenes can be synthesized so that the surface termination group of the monolayer after self-assembly ranges in hydrophilicity. Figure 3.1 shows the molecules used in this study and how the terminal functional group is varied depending on the desired degree of environmental sensitivity. The 4-(5'''-decyl-[2,2':5',2'':5'',2'''':5''',2''''-quinquethiophen]-5-yl)butanoic acid (D5TBA) has a pentathiophene semiconducting core and a methyl group as the terminal group

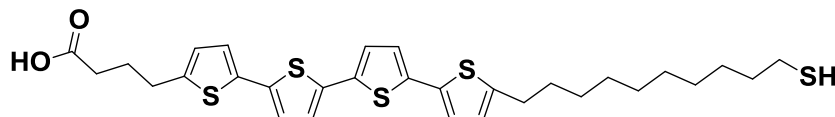
when self-assembled at the air water interface. Previous studies have extensively measured the electronic properties⁸⁶⁻⁸⁸ and crystal-growth⁸⁹ of a D5TBA monolayer. However, while D5TBA would make a good candidate for an organic field-effect transistor, it would not be suitable for sensor applications because the methyl termination would most likely not be sensitive to environmental changes.



4-(5''''-decyl-[2,2':5',2'':5'',2''':5''',2''''-quinque thiophen]-5-yl)butanoic acid (D5TBA)



4-(5'''-(10-hydroxydecyl)-[2,2':5',2'':5'',2'''-quater thiophen]-5-yl)butanoic acid (HD4TBA)



4-(5'''-(10-mercaptodecyl)-[2,2':5',2'':5'',2'''-quater thiophen]-5-yl)butanoic acid (TD4TBA)

Figure 3.1. Molecular structures of oligothiophenes used in this study

The 4-(5'''-(10-hydroxydecyl)-[2,2':5',2'':5'',2'''-quater thiophen]-5-yl)butanoic acid (HD4TBA) and 4-(5'''-(10-mercaptodecyl)-[2,2':5',2'':5'',2'''-quater thiophen]-5-yl)butanoic acid (TD4TBA) oligothiophenes are similar to D5TBA but contain fewer thiophene groups and a functionalized terminal group. HD4TBA would be useful for the study of humidity effects on the electrical properties of self-assembled oligothiophene monolayers. The self-assembly behavior and electrical properties of HD4TBA have not been investigated as of yet but the structure of the molecule should lead to similar self-assembly to that of D5TBA at the air-water interface. TD4TBA is functionalized with a thiol which should allow for a self-assembled monolayer (SAM) to form on a gold surface. While such a system would be different from the D5TBA/HD4TBA system that is self-assembled at the air-water interface, TD4TBA SAMs on gold is a good model system for ambient-pressure x-ray photoelectron spectroscopy (APXPS) experiments due to the stability of the gold-thiol bond in vacuum conditions. Humidity should play a role on the binding energy of TD4TBA atoms if there is a strong enough interaction between water vapor and the film.

This work studies the effect functionalization has on the electronic properties of oligothiophene monolayers. The hydroxyl functionalization of HD4TBA is shown to not interfere with the self-assembly at the air-water interface. HD4TBA crystallizes into similar islands as D5TBA. The CAFM measurements of HD4TBA monolayers indicate that while lateral conductivity is present in a quaterthiophene system, the reduction of the thiophene semiconducting core to only four thiophene units leads to lower conductivity than the pentathiophene core of D5TBA. However, the presence of a hydroxyl (HD4TBA) or carboxylic

(TD4TBA) group is shown to be important for the surface electrical properties of oligothiophenes by KPFM and APXPS as the methyl terminated D5TBA is the only oligothiophene that is not sensitive to humidity changes due to the inability to hydrogen bond with water vapor.

3.2 Experimental

Solutions of 0.1 mg/mL D5TBA and HD4TBA in chloroform were prepared. Solutions were used for up to two months before a fresh solution was necessary due to molecule degradation. Solutions were sonicated for 15 minutes prior to use to break up solution aggregates and immediately filtered using Whatman® 1 qualitative filter paper prior to use. Depending on the desired substrate coverage, 150-300 μ L of solution was gently deposited on MilliQ water in a Teflon Langmuir-Blodgett trough making sure no droplet penetrated the water and deposited underneath the surface. The solution was left to evaporate for approximately 30 minutes or until the surface pressure of the water reached its value prior to chloroform deposition. For mixed oligothiophene samples, a second aliquot of a different oligothiophene solution was subsequently added to the surface. After the chloroform evaporation, the surface was compressed until a desired surface pressure was reached. Typical values were 0.5-2 mN/m. After the compression finished, while maintain the surface pressure constant, the film was transferred at a rate of 1mm/min onto a hydrophilic substrate. Substrates included highly doped p-type silicon wafer with native oxide or freshly cleaved mica.

AFM images were obtained on an Agilent 5500 (Keysight Technologies, Santa Rosa, CA, USA) using OMCL-AC240TM probes (Olympus Micro Cantilevers, Japan) which have a 20 nm platinum coating with a titanium adhesion layer on the tip side and a nominal resonant frequency value of 70 kHz with a nominal spring constant of 2 N/m. The tip radius is 15 nm. Kelvin probe force microscopy was performed using a tip bias of $V_{AC} = 2V$ with a frequency of 2 kHz using a HF2LI lock-in amplifier (Zurich Instruments AG, Switzerland). Conductive AFM images were obtained under ambient conditions using CONTV-PT probes (Bruker, Camarillo, CA, USA) with a nominal force constant of 0.2 N/m and a load of $\sim 1-5$ nN. Voltage biases were applied to the sample and the current was collected through the tip which was held as ground. Humidity was controlled by blowing dry nitrogen or nitrogen bubbled through water into the enclosed AFM chamber. AFM images were analyzed using Gwyddion SPM data analysis software. Solution absorbance was measured on an Agilent Cary 5000 UV-Vis-NIR using a concentration of 0.1 mg/mL in chloroform. All measurements were performed at 298K.

X-ray photoelectron spectroscopy experiments were performed at beamline 9.3.2 at the Advanced Light Source in Berkeley, CA, USA.⁹⁰ TD4TBA was dissolved in dry THF in a 1.75 mg/mL concentration. A 30 nm evaporated gold film on mica with a substrate size of approximately 1cm² was submerged in 2 mL of solution and the mixture sealed for 24 hours to facilitate monolayer formation on the gold surface. The sample was then rinsed with copious amounts of THF and then air dried. After transferring the sample to the AP-XPS chamber, the sample was placed under high vacuum conditions ($<10^{-6}$ torr) for measurement using an incident energy of 650 eV. To measure the effect of water adsorption on the TD4TBA sample, water was first freeze-pump-thawed to purify the water of other gases and then introduced into the chamber

to a final chamber pressure of 100 mTorr using a leak valve before measurement. All APXPS measurements were taken at 298K.

3.3 Results and Discussion

3.3.1 Self-assembly of HD4TBA into crystalline monolayers

The pressure-area isotherm of HD4TBA indicates HD4TBA self-assembles into crystalline islands upon solvent evaporation at the air-water interface. The pressure-area isotherms for D5TBA and HD4TBA are shown in Figure 3.2. Both oligothiophenes show the same behavior over the compression area. The initial increase (240cm² to 220cm²) is due to mechanical effects in the experimental apparatus and is not the result of film compression. Both D5TBA and HD4TBA show a flat region of no changing surface pressure until the compression area is reduced to less than half of the available area. Both isotherms then proceed to increase exponentially to higher surface pressures. This isotherm behavior has previously been reported for D5TBA and the film morphology has been studied at various regions of the isotherm finding that D5TBA crystallizes into monolayer islands upon solvent evaporation.^{87,91} The amphiphilic nature of D5TBA results in the butyric group orienting itself towards the water and the long decyl group away from the water. Compression does not change the morphology of the crystalline islands or the packing of the molecules within an island but rather only pushes islands into each other forming a network of islands. Based on the isotherm behavior shown in Figure 3.2, HD4TBA appears to self-assemble in the same way and the compression would most likely not affect the molecular packing.

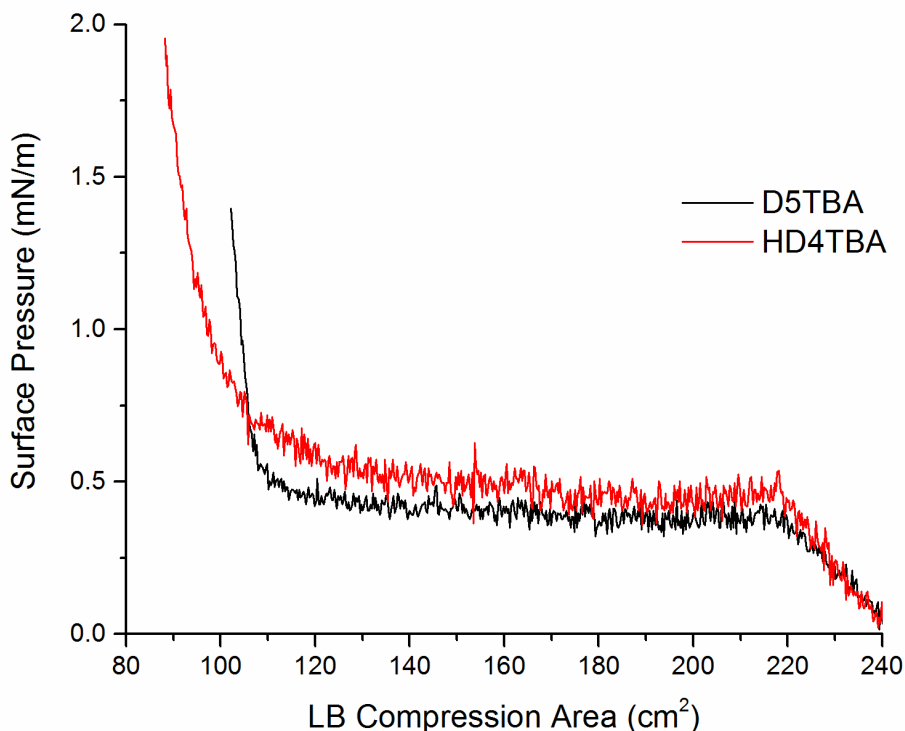


Figure 3.2. Langmuir-Blodgett surface-pressure isotherms of D5TBA and HD4TBA

AFM is capable of resolving morphological differences in the self-assembly nature of D5TBA and HD4TBA. The morphological difference between the crystalline monolayers is visible in the AFM height images in Figure 3.3. At 0.1 mg/mL concentration, the majority of D5TBA islands show a dense round shape with a width of ~800 nm. This is contrasted by the more porous morphology of the HD4TBA film with no islands present in the region shown, indicating that at the same concentration D5TBA can more easily self-assemble into large islands whereas HD4TBA cannot. As a result the HD4TBA film resembles the film morphology of D5TBA when the concentration is not high enough to nucleate island growth.⁸⁷

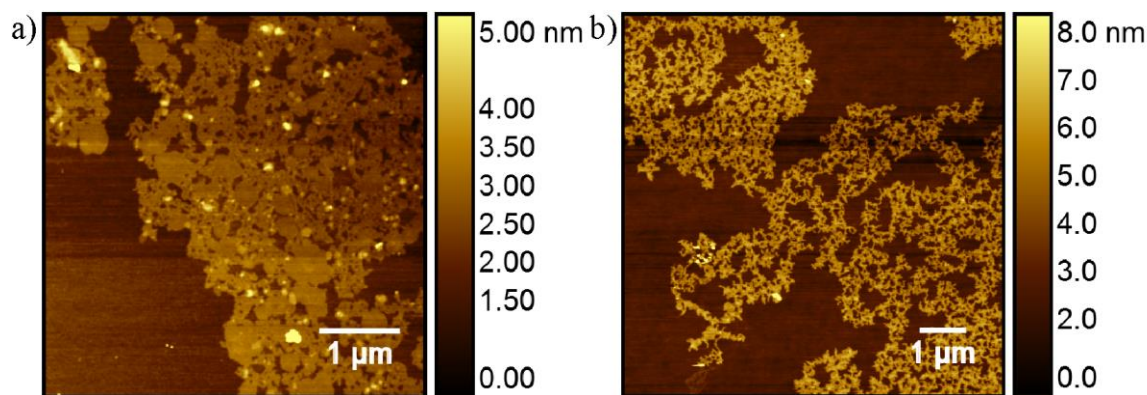


Figure 3.3. AFM height images of oligothiophene monolayers. a) D5TBA and b) HD4TBA on mica.

Based on the AFM imaging, the self-assembly behavior of HD4TBA and D5TBA do not seem to differ. Thiophenes have been shown to prefer the herringbone packing motif.⁹²⁻⁹³ It is assumed that the HD4TBA molecules preferentially self-assemble with the butyric acid pointed towards the water similar to D5TBA because butyric acid is soluble in water whereas 1-decanol is insoluble. The height of a D5TBA monolayer island is 2.6 nm whereas the height of the HD4TBA film is approximately 1.6 nm (see Figure 3.5). The theoretical length of a full length HD4TBA molecule is 3.1 nm, which is significantly longer than the height of the self-assembled monolayer. For D5TBA the shorter height compared to its full length of 3.6 nm was found to be due to molecular tilt at both the decyl chain and butyric acid and a similar effect is expected for HD4TBA.⁸⁷ However due to the presence of a hydroxyl group the chain length is slightly increased and the tilt is expected to increase for HD4TBA.⁹⁴⁻⁹⁵ This is consistent with the height of the HD4TBA monolayer being only 52% of the molecule length compared to 72% for D5TBA. With D5TBA's herringbone crystal structure⁸⁸ one may infer that the removal of one thiophene functional group and the addition of a hydroxyl terminal group should not disrupt the driving force of π - π stacking on the self-assembly at the air-water interface. However, the HD4TBA π - π stacking is weaker compared to D5TBA and is the likely reason for the less dense morphology compared to D5TBA at the same concentration. While densely packed islands are present (see Figures 3.4 and Figure 3.8) they are more sparse when compared to D5TBA at the same concentrations.

Multiple oligothiophene monolayers can be placed on the same substrate by sequential Langmuir-Blodgett depositions. Figure 3.4 shows a Langmuir-Blodgett deposition where D5TBA was first pipetted on top of the water of the trough followed by HD4TBA. The height image in Figure 3.4a shows two distinct regions. In the middle-left region the film is the lowest

height of the entire sample with a height of ~ 2.6 nm. This is most likely a single layer of D5TBA. The rest of the image shows a second layer at a higher height of ~ 4.4 nm. This second layer has two distinct morphologies. On the left side of the image it is porous and appears to mimic the morphology of the D5TBA underneath. On the right side of the image, the film is denser and island-like.

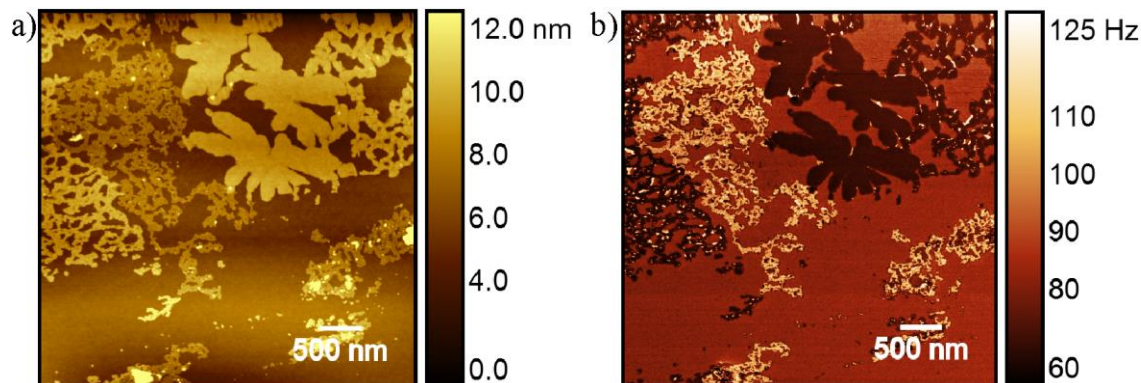


Figure 3.4. AFM Imaging of mixed D5TBA/HD4TBA monolayers. (a) Height and (b) frequency shift images.

When operating the AFM in non-contact mode, a frequency shift to the resonance frequency occurs that can be simultaneously recorded to give a frequency shift image. Looking at the frequency image in Figure 3.4b the D5TBA layer has a positive frequency shift relative to the silicon substrate whereas the second layer shows a negative frequency shift relative to the silicon substrate. A positive frequency shift is due to repulsive forces and with a silicon tip would indicate a more hydrophobic interaction.⁹⁶ The silicon surface should be mostly hydrophilic due to the presence of SiO_2 and SiOH groups, indicating this second oligothiophene layer has a hydrophilic termination. This second layer is most likely HD4TBA that self-assembled on top of D5TBA. In non-contact AFM the height is not always accurate due to forces on the tip⁹⁶, so the apparent height of 1.8 nm for a HD4TBA second layer is inaccurate but comparable to value of 1.6 nm measured by contact AFM (Figure 3.5). The growth of the second layer of HD4TBA can start to be understood by considering the nature of HD4TBA molecules in chloroform solution around D5TBA islands. It appears from the images in Figure 3.4 that there are regions of HD4TBA that overlap perfectly with the D5TBA underneath. This growth occurs during the chloroform evaporation on the air-water interface. One can assume that HD4TBA nucleation crystals can form on top of the D5TBA the same way they can on the water surface and begin to grow continuously over the areas of D5TBA. However, the HD4TBA that is at the edges of the D5TBA that does not nucleate or HD4TBA that is not on the D5TBA is free to move further away from the D5TBA island and nucleate/grow elsewhere. This would explain why in the image shown in Figure 3.4 there are no distinct HD4TBA islands that reside over D5TBA and the silicon substrate equally. However, further experiments in the deposition procedure and growth are necessary to fully understand the growth of second layer oligothiophenes and the role of solvent molecules in the preferential packing of oligothiophenes on top of each other.

3.3.2 Electronic properties of D5TBA and HD4TBA monolayers

To confirm the presence of electrical connectivity between molecules in HD4TBA, the conductivity of Langmuir-Blodgett monolayers was measured by conductive AFM. When

D5TBA is deposited on highly doped silicon with only a native oxide, a higher current is measured when the tip is on top of D5TBA than the substrate. The higher current over D5TBA is explained with a lateral conduction model.⁸⁷ When a hole is injected into D5TBA monolayers, the hole will go through a hopping mechanism to neighboring D5TBA molecules which will increase the area for tunneling through the oxide to the doped silicon. A similar effect can be seen in HD4TBA. Figure 3.5a shows a height image of HD4TBA deposited on highly doped p-type silicon with a native oxide layer (~1nm).

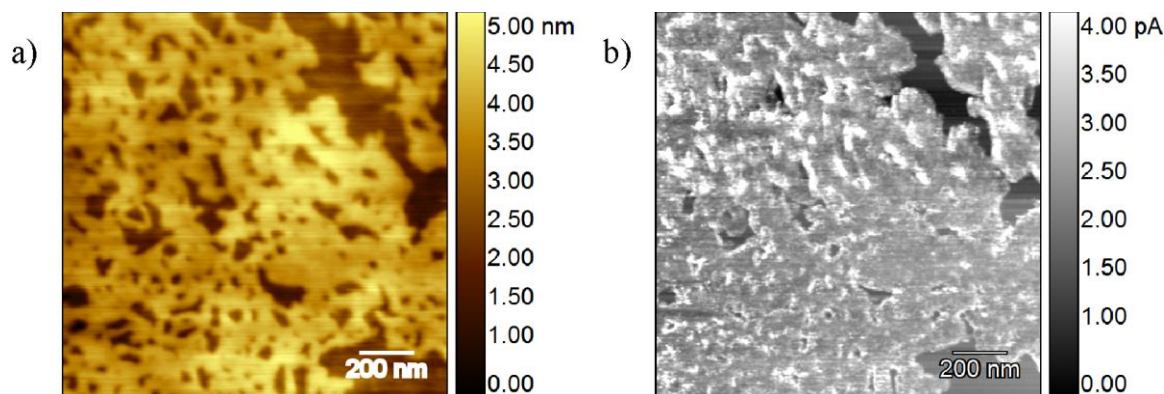


Figure 3.5. Conductive AFM imaging of HD4TBA on doped silicon. (a) Height and (b) current map at -1V sample bias.

The image shows both HD4TBA monolayer film and a region of bare substrate. In Figure 3.5b is the corresponding current map where every pixel is the current measured between the tip and sample with a -1V bias applied to the doped silicon. A negative sample bias on the substrate indicates hole injection from the tip to the film. The current over the bare silicon substrate is ~0pA whereas for the HD4TBA film it is 2-4pA indicating the presence of lateral conduction within a HD4TBA layer. However, the magnitude of current measured for a particular voltage applied is lower for HD4TBA than for D5TBA. The current measured for HD4TBA is approximately twenty times lower than the current measured for D5TBA at the same voltage.⁸⁷ The lower conductivity of HD4TBA compared to D5TBA can be attributed to an increase in the bandgap due to the reduction in the number thiophene groups⁹⁷⁻⁹⁸ and the introduction of a hydroxyl group which can act as an electron trap^{20, 78, 99-101} reducing the current in the measurement compared to a methyl terminated molecule. In addition, the thiophene packing of the thiophenes in HD4TBA are not necessarily as well-aligned as in the case of D5TBA. The optical bandgap can be estimated by measuring the absorption edge of the oligothiophene solution.⁶⁶ Figure 3.6 shows the absorbance onset of D5TBA is at a higher wavelength than that of HD4TBA as expected. Using the absorption edges, the D5TBA optical bandgap is estimated to be ~2.5eV whereas HD4TBA has an optical bandgap of ~2.7eV. While the hydroxyl group makes HD4TBA an important model system to study for environmental effects on the electronic properties of thiophene molecules, the low conductivity of HD4TBA makes it difficult to study using current sensing techniques such as conductive AFM.

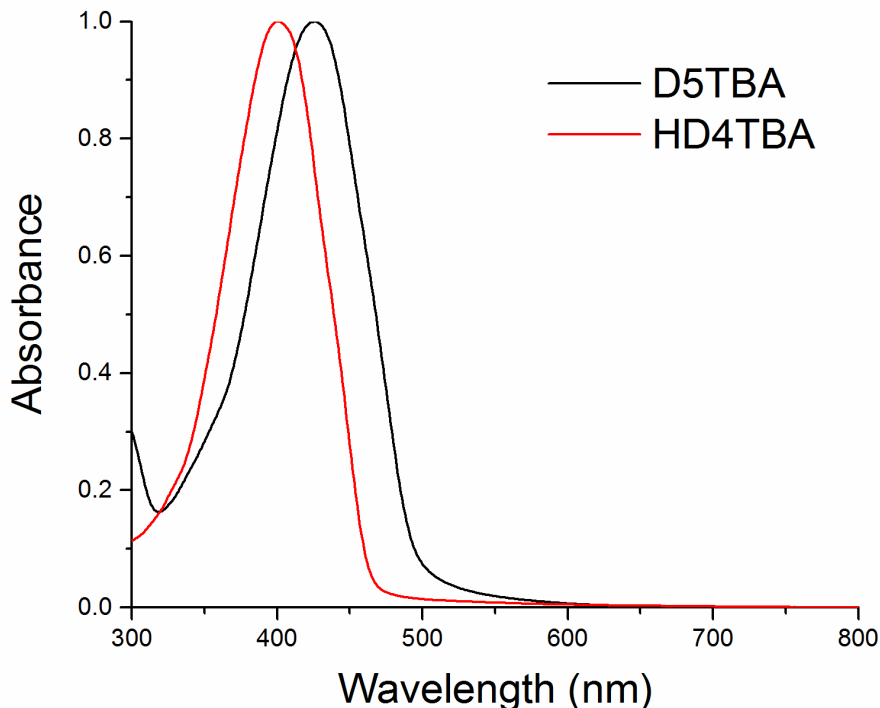


Figure 3.6. UV-Vis absorbance of D5TBA and HD4TBA solutions in chloroform.

Kelvin probe force microscopy is a useful tool to probe the work function difference between HD4TBA and D5TBA monolayers. Kelvin probe is sensitive to variations in the surface potential in organic films¹⁰² and can be used to probe the effect changing the surface termination of a monolayer has on the surface potential.¹⁰³⁻¹⁰⁵ Mixed monolayer samples were studied to avoid tip changes that would occur if different samples were measured in different conditions giving rise to variations in contact potential difference (CPD) that were the result of tip inconsistency rather than true surface potential heterogeneity between samples. Figure 3.7 shows the same mixed monolayer sample as in Figure 3.4 with Figure 3.7b showing the work function as measured by the platinum tip in ambient conditions. The platinum tip was calibrated beforehand by measuring a reference HOPG substrate ($\Phi=4.6\text{eV}$) and the tip's work function was determined to be 4.92eV. The platinum tip measures the CPD between the tip and the oligothiophene monolayer and with this calibration the work function of the sample is calculated by subtracting the surface potential from the tip. The tip quality for KPFM is poor in Figure 3.7b but the quantitative difference between different monolayers can still be discerned.

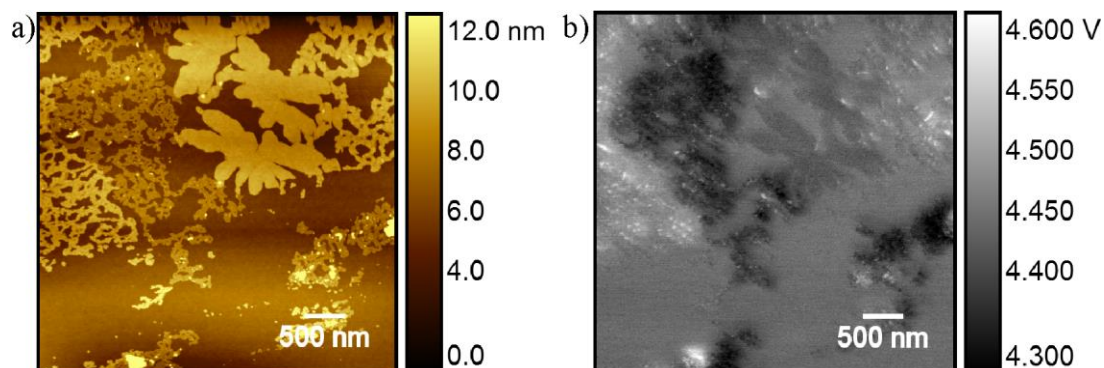


Figure 3.7. Kelvin probe microscopy of mixed D5TBA/HD4TBA monolayers. (a) Height (non-contact) and (b) work function image calculated from the KPFM surface potential image. HOPG is used as a reference to calibrate the tip work function.

The D5TBA monolayer has a work function of $\sim 4.35\text{eV}$ and HD4TBA is shown to have a work function that is larger than D5TBA which is expected. HD4TBA monolayers differ from D5TBA by reducing the number of thiophenes present in the semiconducting core and the presence of a hydroxyl group instead of a methyl group at the surface of the monolayer closest to the tip. The theoretical band structure of thiophene oligomers indicates that the work function of pentathiophene would be smaller than that of a quaterthiophene⁹⁸ which fits with the pentathiophene derivative D5TBA having a smaller work function. In addition, experimental and theoretical results show that fluorinated self-assembled monolayers on gold lowers the surface potential, thereby increasing the work function, compared to that of a methyl due to the molecular dipole strength directed along the normal direction to the surface.¹⁰⁶ The hydroxyl group on HD4TBA would in the same way lower the surface potential compared to the methyl termination of D5TBA, also leading to an increase in the work function of the HD4TBA monolayer. Because KPFM is surface sensitive, the change from methyl to hydroxyl termination is predicted to dominate the increase in measured work function although the influence in thiophene groups cannot be ruled out.

In addition, HD4TBA shows two distinct values for the work function that is based on the film morphology. For the densely packed islands the measured work function is $\sim 4.5\text{eV}$ whereas for the porous morphology the work function is higher with a value of $\sim 4.6\text{eV}$. The extent of crystalline molecular packing is larger in the island-like which could give rise to a greater degree of electron delocalization which has been shown to decrease the work function in π -stacked materials.¹⁰⁷⁻¹⁰⁸ Although the poor tip quality in the image could lead to tip artifacts it would not explain the quantitative difference in work measured work function which seems constant over an area much larger than the tip area ($\sim 10\text{-}20\text{nm}$).

3.3.3 Changes in surface potential of HD4TBA and D5TBA with varying humidity

The effect water adsorption has on the electronic properties of oligothiophenes can be studied by kelvin probe force microscopy while varying the humidity of the local environment. Water layers have been known to influence the surface potential of a surface by the process of shielding.⁴⁷ Figure 3.8 shows the height and CPD of a region of HD4TBA monolayer on silicon. The HD4TBA island has a surface potential that is distinct from that of the silicon oxide surface of the substrate according to Figure 3.8b.

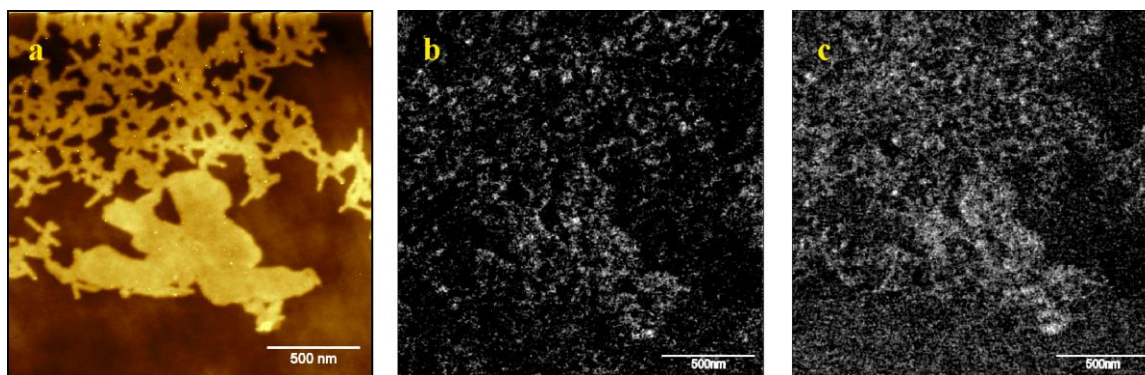


Figure 3.8. Kelvin probe force microscopy imaging of HD4TBA under varying humidity. (a) Height image (non-contact) and (b) CPD at 2.9% relative humidity. (c) CPD at 19.6% relative humidity. The CPD images have a color scale of -200meV.

The contact potential of HD4TBA can be monitored over time in the same location as the humidity is increased. Figure 3.8c shows the same region where the relative humidity has been increased to 19.6%. The CPD shows a brighter contrast to the HD4TBA layer which indicates that the CPD has increased (more positive). This increase is expected with water adsorption on to the surface of a HD4TBA monolayer. The CPD of the HD4TBA island measured over a large humidity range is shown in Figure 3.9. The CPD sharply increases up to ~10% RH before the rate of CPD increase changes. A similar CPD increase after 10% RH was observed by Verdaguer and coworkers¹⁰⁹ on silicon oxide, however no CPD measurements were obtained on silicon oxide with less than 10% RH.

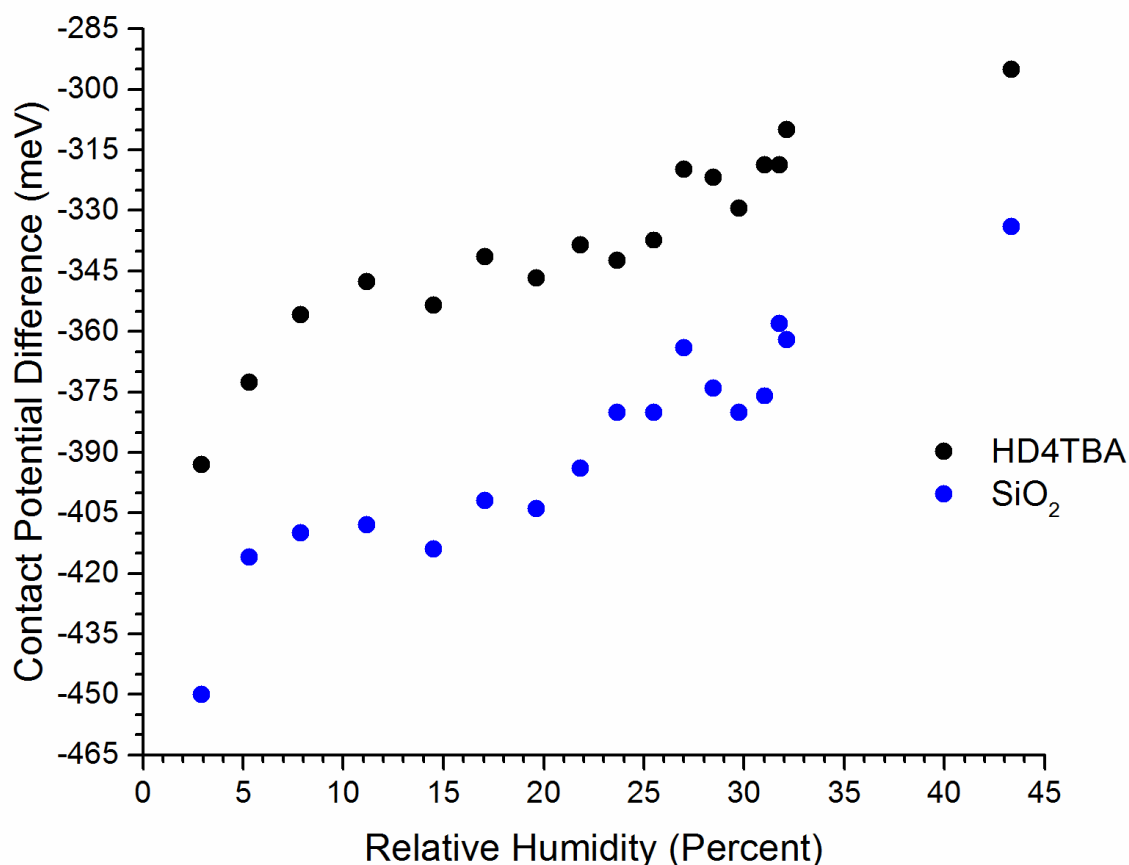


Figure 3.9. Contact potential difference of HD4TBA monolayer and the silicon oxide substrate with varying humidity

The low humidity regime (<20% RH) is where one monolayer of water is expected to form on a hydrophilic surface such as mica and silicon oxide¹⁰⁹ and the CPD-relative humidity curve matches the water adsorption isotherm seen on other hydrophilic surfaces.¹¹⁰⁻¹¹¹ The shape of the curve, if taken as an indicative of water adsorption, would fit with the Langmuir model¹¹² and would be comparable to vibrational studies probing water adsorption on a hydroxyl terminated self-assembled thiol monolayer.¹¹³⁻¹¹⁴ However the structure of the water layer cannot be discerned by the shape of the isotherm here. The CPD increases by ~40meV which falls in the expected range of a single hydroxyl-water interaction¹¹⁵ indicating that KPFM is sensitive enough to be measuring the adsorption of a single water layer on a HD4TBA monolayer. The CPD-relative humidity curve of the silicon oxide substrate is also shown for reference in Figure 3.9. The shape and magnitude of the curve is comparable to previous measurements.¹⁰⁹ Further sum-frequency generation vibrational spectroscopy studies under varying humidity would be beneficial to probe the exact geometry of the interaction between the water vapor and hydroxyl groups of HD4TBA.

The sensitivity of different functional groups to the increase in humidity can be probed by monitoring the surface potential of different oligothiophenes simultaneously by KPFM. HD4TBA has a hydroxyl termination group which is active for hydrogen bonding whereas D5TBA has a methyl group which should be inert to the presence of water. Figure 3.10a shows a

mixed HD4TBA/D5TBA monolayer film on silicon. The top image is an AFM height image showing a mixed film with both D5TBA and HD4TBA present. The bottom image is a CPD image of the same region taken at $\sim 0\%$ RH. A more positive CPD indicates a smaller work function. The regions of D5TBA and HD4TBA are difficult to discern in height (upper) and CPD (lower) but according to previous KPFM measurements (Figure 3.7) the film with a more positive CPD should be regions of D5TBA due to D5TBA having a smaller work function than HD4TBA.

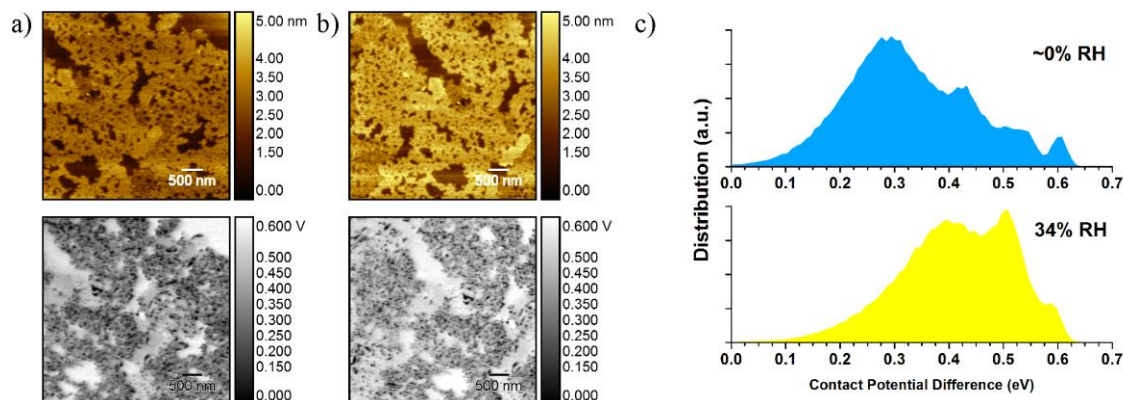


Figure 3.10. Kelvin probe imaging of mixed D5TBA/HD4TBA monolayers under varying humidity. Height and CPD images taken at (a) $\sim 0\%$ RH and (b) 34% RH. (c) Distribution of contact potential difference values in the AFM image.

The mixed monolayer sample was placed in a sealed chamber and the humidity was controlled by a combination of dry nitrogen gas flow and nitrogen bubbled through water. Figure 3.10a shows the height and CPD of the mixed film at $\sim 0\%$ RH and Figure 3.10b shows the same region at 34% RH. The distribution of CPD values in both images are plotted in Figure 3.10c. The $\sim 0\%$ RH values show four distinct populations of CPD values: 280meV, 440meV, 500-550meV, and 600meV. The highest value is attributed to the silicon oxide substrate whereas the 500-550meV is attributed to D5TBA. The other two values of CPD (440meV and 280meV) correspond to HD4TBA film. The measurement in Figure 3.7 better resolved the spatial separation of HD4TBA and D5TBA and there HD4TBA was found to have a CPD -200meV when porous and -300meV when island-like compared to D5TBA. These values are close to the differences seen in Figure 3.10 between HD4TBA and D5TBA although are not expected to match due to the difference in the humidity conditions. In addition, in this particular sample the two oligothiophenes may have mixed more during the Langmuir-Blodgett process giving rise to a larger CPD contribution of D5TBA to the HD4TBA region.

The increase in humidity leads to an increase in contact potential difference that is very apparent when the CPD values are compared for the dry and humid case in Figure 3.10c. When the mixed film is at 34% RH, a large portion of the CPD values increase from the dry measurement and now have a large broad distribution around 400meV. The increase is of similar magnitude to that observed with just HD4TBA (Figure 3.9). On the other hand in both $\sim 0\%$ RH and 34% RH there is large group of values 500-550meV indicating that the D5TBA CPD does not change as humidity changes. Figure 3.11 shows a model for the observed CPD change in both monolayers.

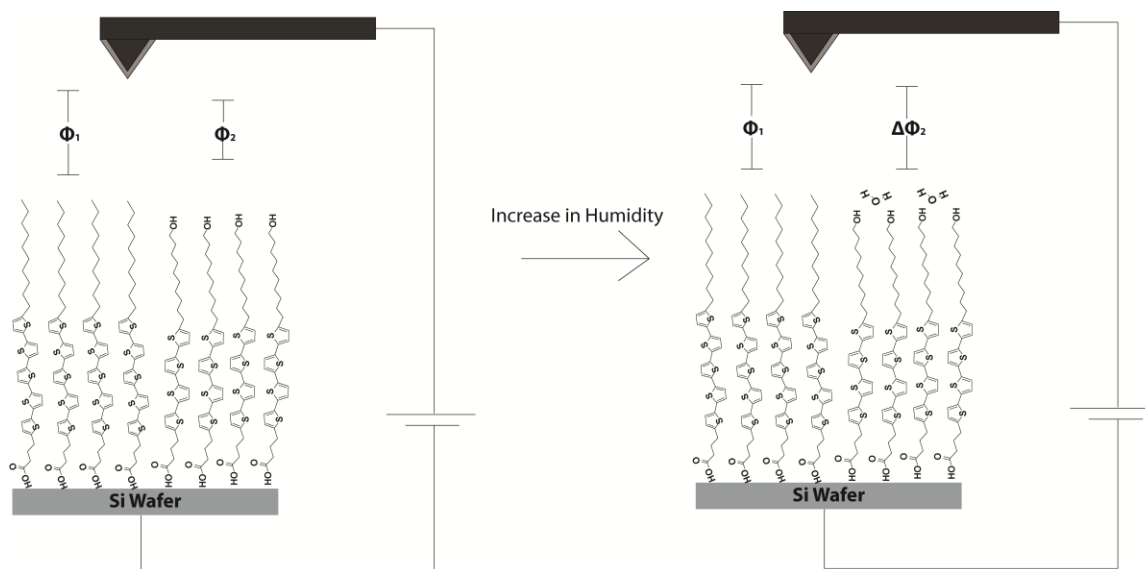


Figure 3.11. Diagram of a D5TBA/HD4TBA mixed film and the work function change of each oligothiophene upon the addition of water vapor.

Tu and coworkers¹¹³ found that on a methyl terminated SAM, water did not adsorb at room temperature and over a large humidity range (0-95% RH). Therefore one would expect that water should not adsorb onto the methyl surface of a D5TBA monolayer and if there was no other site of adsorption that the contact potential difference of D5TBA should not change due to humidity changes which is in contrast to the hydroxyl terminated HD4TBA. These results show that KPFM is sensitive enough to monitor the electrostatic behavior of two very similar albeit different organic semiconductors under the presence of an analyte.

3.3.4 Oxygen sensitivity of TD4TBA to water vapor by APXPS

Ambient pressure x-ray photoelectron spectroscopy was performed to better understand the location of water adsorption on oligothiophene monolayers and test the suitability of a synchrotron to monitor water adsorption progress on an organic semiconductor monolayer. Although KPFM is a powerful technique to study the electrostatics of water adsorption, it does so on a length scale much larger than a single molecule and functional group. APXPS can localize the binding event to a specific atom because of the elemental specificity of core-electron binding energies. In functional oligothiophenes with unique chemical groups, the location of water adsorption can be discerned by looking for changes to the binding energy of different elements and seeing which one differs under the presence of water vapor compared to vacuum conditions. Due to the synthetic challenge of obtaining a thiol-carboxylic group substitution derivative of HD4TBA, TD4TBA self-assembled on gold was used instead. TD4TBA has a carboxylic acid hydrophilic termination group which should be the primary location of water adsorption however the adsorption on thiophene groups cannot be ruled out.¹¹⁶ Ketteler and coworkers⁵⁷ showed that for a 11-mercaptoundecanoic acid SAM on gold, water vapor was found to change the O1s binding energy region at 100mTorr. Similar to 11-mercaptoundecanoic acid, TD4TBA's carboxylic acid group has two distinct oxygen binding energies which can both be observed in UHV as shown by Figure 3.12a.

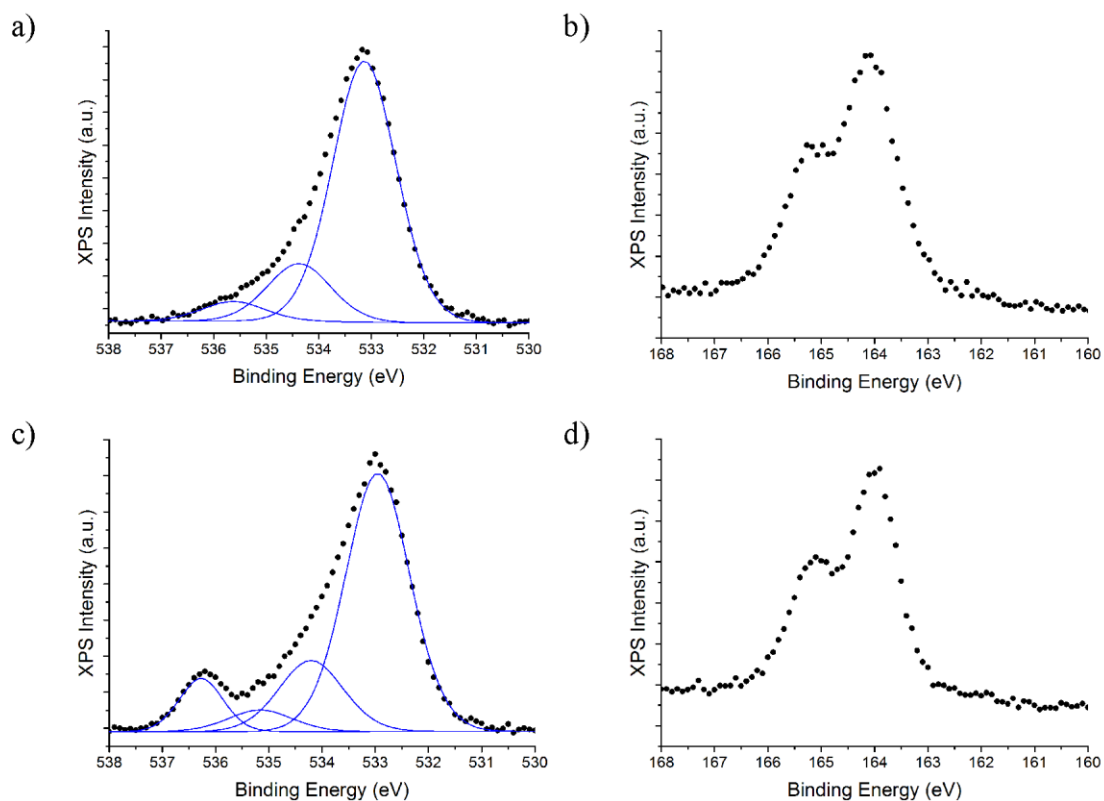


Figure 3.12. Ambient pressure X-ray photoelectron spectroscopy of TD4TBA on gold. a) O1s and b) S2p XPS binding energies in vacuum conditions. (c) O1s and (d) S2p XPS binding energies in 100mTorr of water.

The dominant peak at 533.1eV corresponds to a C=O bond whereas the higher energy peak at 534.4eV is due to the C-OH bond of the carboxylic acid group. The third peak at 535.6eV most likely corresponds to some form of water on the gold substrate that is not removed and remains constant over the experiment.¹¹⁷⁻¹¹⁸ Upon introducing 100mTorr of water into the chamber the O1s region changes as shown by Figure 3.12c. The new peak at 536.3eV is water in the vapor phase as it grew slowly while the pressure of water increased. The ratio of the C=O/C-OH peaks also change: in UHV it is 4.5 whereas in 100mTorr it is 3.6. The change of peak ratios indicates that introducing water into the chamber perturbed the carboxylic acid groups of TD4TBA in some way. The water molecules most likely exhibit some hydrogen bonding with the carboxylic acid surface group. In contrast to the O1s region, the S2p region of TD4TBA does not change from UHV (Figure 3.12b) to more humid conditions (Figure 3.12d). The sulfur 2p peak is at the same binding energy previously seen for thiophene SAMs on gold.¹¹⁹ Furthermore, beam damage previously observed in alkyl-based SAMs on gold⁵⁷ is not observed here indicating the measured sulfur peak is most likely of the thiophenes and not of the gold-sulfur bond. The lack of change to the sulfur peak under the presence of water vapor indicates either water does not interact with the sulfur atom of the thiophenes or the interaction is not strong enough to perturb the sulfur binding energy. It should be noted that at 24°C a water pressure of 100mTorr corresponds to a relative humidity of ~0.45% which is quite small. And previous studies have shown that the water-uptake behavior of carboxylic acid SAMs is not high below a relative humidity value of 35%.¹¹³ Unfortunately experimental limitations prevented measurements at

higher gas pressures but one can speculate that measuring the S2p and O1s binding energy at RH values of >40% might lead to more significant changes.

3.4 Conclusions

HD4TBA was successfully self-assembled at the air-water interface into conductive crystalline islands. The CAFM measurements of HD4TBA films revealed the presence of lateral conduction between neighboring HD4TBA molecules but smaller in magnitude compared to that of the pentathiophene D5TBA monolayer. KPFM determined the work function of a HD4TBA monolayer was larger than a D5TBA monolayer due to the reduction of the semiconducting core and the presence of a hydroxyl dipole at the surface. However, the methyl terminated D5TBA was shown to not be sensitive to humidity changes by KPFM whereas the hydrophilic HD4TBA was found to show favorable water adsorption by KPFM. APXPS of TD4TBA revealed that water adsorption most likely does not occur on the thiophene groups at low humidity and that the most likely location of water adsorption is onto hydrophilic groups such as a carboxylic acid group or hydroxyl group. The choice of chemical functional groups is an important parameter to consider both when designing organic materials for OFETs and organic sensors. The presence of hydrophilic groups are not desirable for OFETs as water adsorption will change and disrupt the electronic behavior of films while completely inert films are of no use for sensor applications. Scanning probe techniques such as KPFM are simple and efficient measurement tools to probe how sensitive a molecule is to local environmental changes. Further studies can be done to couple KPFM or CAFM techniques with transistor geometries to better spatially correlate sensor performance with sensitivity to a specific analyte.

4 Self-assembly of Indigo Small Molecules at the Air-Water Interface

Abstract

Indigo small molecules were self-assembled at the air-water interface into unique morphologies illustrating the importance of intermolecular interactions in determining the structure of crystalline organic systems. EH-Indigo and EHT-Indigo are organic semiconductors that vary only by the addition of two thiophene groups but each molecule presents a unique nanoscale morphology useful for different organic electronic applications. EH-Indigo exhibits anisotropic self-assembly resulting in discrete rectangular crystallites that are studied for structure and mechanical properties by AFM. The molecular packing and origin of the anisotropy is resolved using GIWAXS. The interplay between hydrogen bonding interactions and π - π stacking leads to preferential growth in one orientation of the air-water surface plane leading to the rectangular shape of the crystallite. The lateral π - π stacking of EH-Indigo and extremely high crystallinity makes it an ideal material for organic field-effect transistors. In the EHT-Indigo case the crystal structure by GIWAXS is revealed to have no heterogeneity in the lateral intermolecular interactions resulting in isotropic film morphologies. The addition of the thiophene unit aligns the EHT-Indigo molecules parallel to the plane of the water and which makes it an ideal geometry for applications requiring planar charge transport contrasted with the perpendicular geometry of EH-Indigo.

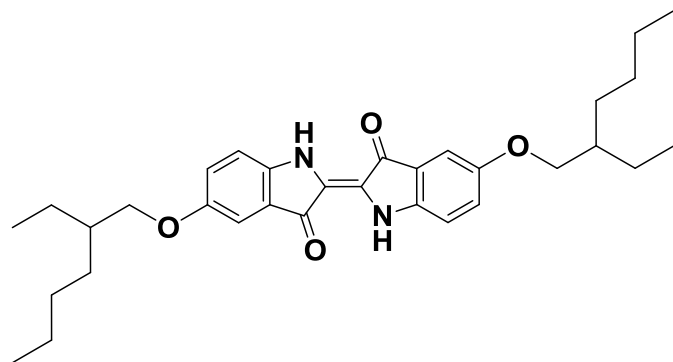
4.1 Introduction

Indigo and its derivatives have been well studied historically for their photophysical properties in the past due to their extensive use in the industry as a colorant.^{120,121,122} In recent times, the use of indigo derivatives in organic electronics has gained much interest due to its promising ambipolar charge transport behavior.^{123,124,125,126} Ambipolar organic semiconductors are of great importance due to their ability to behave as both electron and hole conductors in a single active layer and have been found to be attractive systems for optoelectronic devices.¹²⁴ In addition, indigo's synthetic flexibility allows for the selective modification of the indigo framework to tune the electronic and optical properties of the dyes.

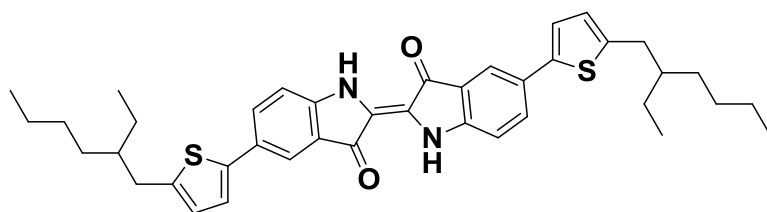
Understanding the self-assembly of nanomaterials is of great importance for the fabrication of high performing electronic devices.¹²⁷⁻¹²⁹ Materials when packed into an ordered state often times exhibit anisotropic charge carrier mobilities that are dependent on the directionality of the packing of individual building blocks. This anisotropy is often the result of simple molecular interaction differences during the self-assembly process.^{130,131,132} A desirable property for the conductive layers in optoelectronic devices is that the charge carrier mobility is preferentially highest along the desired direction for the device (e.g. perpendicular to the source-drain electrodes in a FET). However, fabricating such layers is not trivial with common deposition techniques such as vacuum evaporation, dip coating, or spincoating due to isotropic intermolecular interactions during crystal growth and the important of substrate-molecule interactions. Langmuir-Blodgett is a promising alternative for the formation of crystalline organic layers that avoids the substrate-molecule interaction and can promote anisotropy during self-assembly.¹³³ In an ideal case, an anisotropic conductive film is formed where one specific crystal axis is the dominant conduction pathway and such examples have been demonstrated using solution shearing.¹³⁴⁻¹³⁵ An advantage of Langmuir-Blodgett over other techniques is that the film can be deposited with a preferential geometry onto any device substrate. Forming anisotropic crystals from self-assembly requires fine tuning of the intermolecular and intramolecular interactions of organic semiconductors. The extent of these interactions and how they affect the molecular packing in an organic film can be measured by grazing-incidence wide-angle x-ray scattering in organic films (GIWAXS).¹³⁶ GIWAXS is well suited to probe atomic and molecular distances in thin organic films and the degree of crystallinity can be resolved. Highly anisotropic crystalline films are attractive for organic electronics because they are typically better performing when implemented in a favorable device geometry compared to isotropic films. Controlling the alignment of the charge transport pathway of a device is possible if it becomes feasible to deposit the film consistently in a specific geometry on a pre-patterned substrate.

In this chapter two model indigo small molecules are studied for their ability to form self-assembled microscopic structures that promote charge transport by AFM and GIWAXS. Figure 4.1 shows the two molecules used in this study. The indigo derivative (E)-5,5'-bis((2-ethylhexyl)oxy)-[2,2'-biindolinylidene]-3,3'-dione (EH-Indigo) is representative of the simple indigo molecule with only solubilizing groups attached to the ends. A thiophene derivative of EH-Indigo, (E)-5,5'-bis(5-(2-ethylhexyl)thiophen-2-yl)-[2,2'-biindolinylidene]-3,3'-dione (EHT-Indigo), is also studied to understand how adding substituents to the indigo backbone influences the self-assembly properties. Adding electron donating or electron withdrawing groups is a key

design parameter for organic material it is important to understand how changing the molecular structure affects the crystal structure.



(E)-5,5'-bis((2-ethylhexyl)oxy)-[2,2'-biindolylidene]-3,3'-dione (EH-Indigo)



(E)-5,5'-bis(5-(2-ethylhexyl)thiophen-2-yl)-[2,2'-biindolylidene]-3,3'-dione (EHT-Indigo)

Figure 4.1. Indigo functionalized small molecules used in this study

Indigo small molecule self-assembly at the air-water interface has not been studied as of yet due to the poor solubility of pure indigo in non-polar solvents. Here Langmuir-Blodgett assembly is achieved with EH-Indigo at various compression forces and concentrations. For a small concentration in chloroform with low compression, EH-Indigo self-assembles into highly anisotropic crystallites that result from heterogeneous intermolecular interactions in a plane of the crystallite. GIWAXS reveals that EH-Indigo contains both π - π interactions and hydrogen bonding which compete for crystal growth at the air-water interface. A higher compressive force compresses individual crystallites into denser bundles that are oriented with respect to the water surface. Interestingly a higher concentration of EH-Indigo in chloroform gives a thicker but amorphous morphology and does not form crystallites. The EHT-Indigo Langmuir-Blodgett film shows the dramatic influence thiophene groups have on the self-assembly as an isotropic film forms at the air-water interface. In addition, EHT-Indigo and EH-Indigo π - π stacking orientations are perpendicular to each other at the air-water interface which has an important role for which substrates, geometries, and electronic applications the indigo films are suitable for.

4.2 Experimental

EH-Indigo and EHT-Indigo were separately dissolved in chloroform with a 0.2 mg/mL concentration. Solutions were used for up to six months before a fresh solution was necessary due to molecule degradation. Films of EH-Indigo were prepared on oxygen-plasma cleaned 100-

300 nm SiO₂ silicon wafers using the Langmuir-Blodgett (LB) technique. 150 μ L of 0.2 mg/mL or 2 mg/mL EH-Indigo in chloroform was deposited on the surface of MilliQ water in a Teflon trough. The solution was left to evaporate for approximately 30 minutes or until the surface pressure of the water reached its value prior to chloroform deposition. After the chloroform evaporation, the surface was compressed until a desired surface pressure was reached. After the compression finished, the film was transferred at a rate of 1mm/min onto a hydrophilic substrate while maintaining the surface pressure constant by having the barriers move as required. No further annealing treatment was performed.

Leica DM4000 M (Leica Microsystems, Buffalo Grove, IL, USA) was used for the optical characterization of Langmuir-Blodgett film deposition. Park NX10 system (Park Systems, Santa Clara, CA, USA) was used for AFM imaging of indigo films. AFM images were obtained under ambient conditions using PPP-NCHR probes (Nanosensors, Neuchatel, Switzerland) with a nominal resonant frequency value of 330 kHz. Lateral force AFM images were obtained under ambient conditions using SiNi probes (Budgetsensors, Sofia, Bulgaria) with a nominal force constant of 0.27 N/m and a load of \sim 5nN. AFM images were analyzed using Gwyddion SPM data analysis software. All measurements were performed at 298K.

X-ray scattering was conducted at the Stanford Synchrotron Radiation Lightsource (SSRL) on beamlines 2-1 (high-resolution specular with point detector) and 11-3 (2D grazing-incidence wide-angle with MAR345 image-plate area detector). Incident photon energies of 12 and 12.732 keV were used for beamlines 2-1 and 11-3, respectively. Two mechanical slits (1 mm) and Soller slits (1 mrad) collimated the diffracted beam in the specular diffraction (2-1) and high-resolution grazing-incidence scattering (7-2) geometries, respectively. Two mechanical slits (1 mm) and Soller slits (1 mrad) collimated the diffracted beam in the specular diffraction (2-1). He (g) environments for all measurements were used to minimize air scatter and beam damage to samples. 2D grazing-incidence sample-detector distance was 300mm calibrated with a polycrystalline lanthanide hexaboride (LaB₆) standard at a 3.0° degree angle with respect to the critical angle of the calibrant. For grazing-incidence geometries, the incidence angle was set below the critical angle of the silicon substrate (0.19°) and slightly above that of the organic film (0.10°), ensuring through-thickness sampling of the film. Scattering data are presented in terms of scattering vector $q = 4\pi \sin(\theta) / \lambda$, where θ is half the scattering angle and λ is the wavelength of incident x-rays. Data was processed using Nika 2D data reduction homebuilt WxDiff Software. The terms q_{xy} and q_z denote the component of scattering vector in-plane and out-of-plane with the substrate, respectively. Data from 2D grazing-incidence measurements were corrected for the geometric distortion introduced by a flat, plate detector and processed for subsequent analysis with the software WxDiff.

4.3 Results and Discussion

4.3.1 EH-Indigo crystallite films

EH-Indigo successfully self-assembles at the air-water interface during solvent evaporation. The LB pressure-area curve for EH-Indigo shows no noticeable phase transition

behavior early in the surface compression after the deposition of molecules from a chloroform solution (Figure 4.2). This indicates that the EH-Indigo molecules or assemblies on the water surface do not interact with each other strongly enough to perturb the surface tension. After compressing to half of the available surface area, a rapid increase in surface pressure is seen until a plateau region begins to occur (Figure 4.2). The morphology of the film does not seem to differ at different points along the isotherm until a critical region is reached at high surface pressure (see section 4.3.2). The surface pressure curve is similar to other systems that exhibit self-assembly into crystalline layers at the air-water interface upon solvent evaporation.¹³⁷⁻¹³⁸ As the available surface area for the molecules is decreased, the surface of the water takes on a slight blue color.

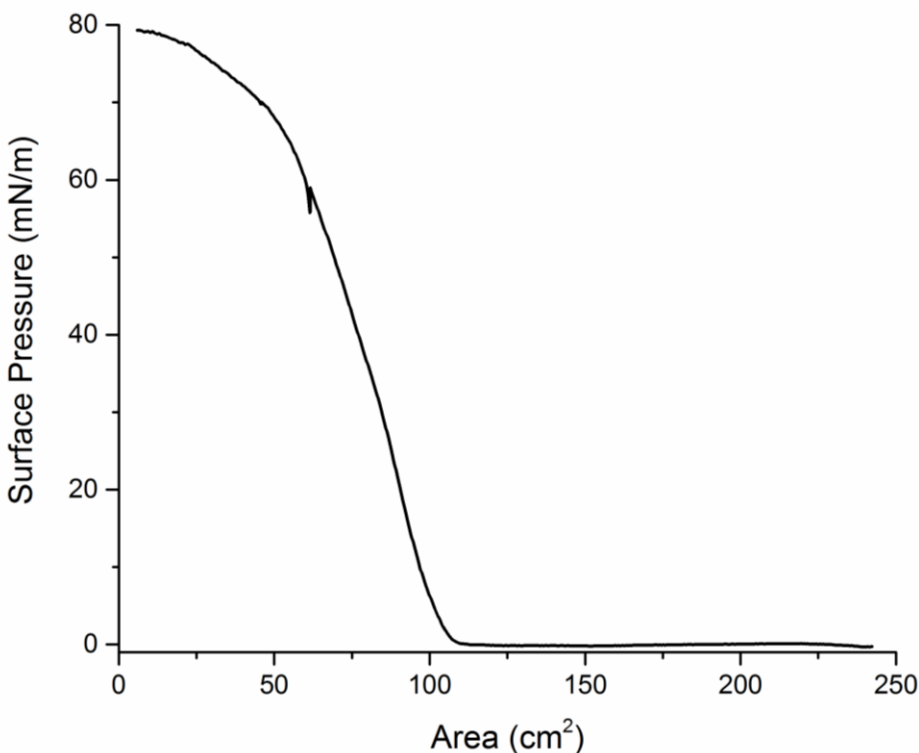


Figure 4.2. Langmuir-Blodgett EH-Indigo pressure-area compression isotherm

At low surface pressures (e.g. 1-3 mN/m) when the film is deposited onto a substrate, the resulting film appears solid over centimeter length scales. To the naked eye, the entire substrate that was in contact with the water surface appears covered with a film. Figure 4.3 shows optical microscope images of the film. The images reveal the film is not entirely continuous. Cracks in the film are present and it is presumed these are the result of the film breaking apart during the deposition process onto the silicon substrate. It is assumed that the film is crack-free prior to the deposition under good compression conditions but falls apart when the external pressure is released or cannot be held sufficiently constant enough during deposition. The film appears conformal in the crack region indicating that on average a complete film was at once present on the water surface rather than pieces of a film compressed together.

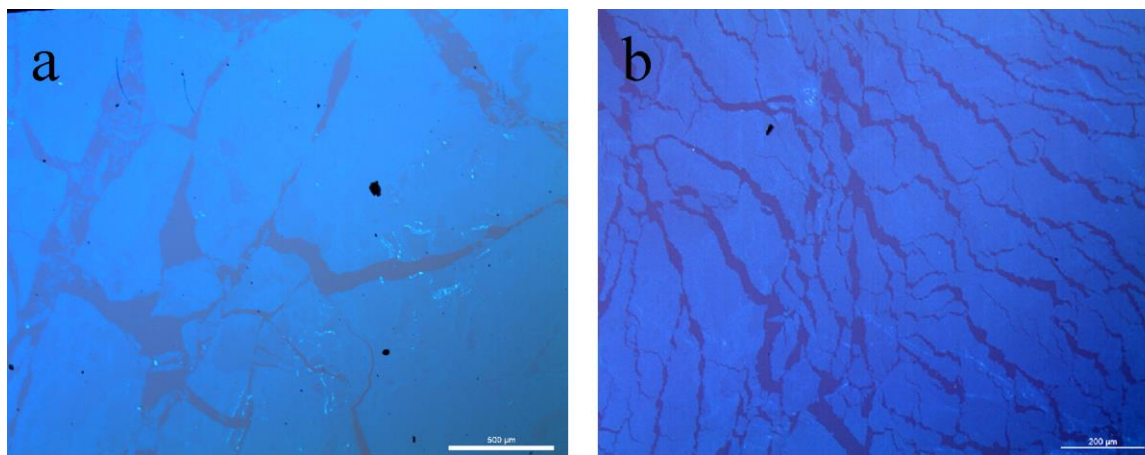


Figure 4.3. Optical microscope images of EH-Indigo films at deposited on silicon oxide at surface compression value of ~ 1 mN/m. (a) Scale bar is 500 microns and (b) different region of same film where scale bar is 200 microns.

It should be noted that the morphology exhibited in Figure 4.3 is consistent only for hydrophilic substrates with a thick insulating oxide (e.g., silicon wafers with 100-300nm silicon oxide or glass slides). Deposition is not possible with highly doped silicon with only native oxide and on conductive substrates such as gold or HOPG. All attempts to image the surface with either optical microscopy or AFM resulted in a bare substrate with no film present. Under the assumption that a film is formed on the water surface prior to deposition onto the substrate it implies there is some inherent factor that is forbidding the film from successfully depositing into the substrates that are higher in conductivity or may have favorable energetic levels for charge transfer. A measurement of HOMO and LUMO levels in EH-Indigo and EH-Indigo crystallites could reveal whether there would be significant charge transfer between the EH-Indigo crystallites and metallic substrates. As will be discussed later (see section 4.3.4), while this is true for EH-Indigo, it is not the case for EHT-Indigo and has to do with the crystal orientation on the water surface.

AFM imaging reveals the crystallite nature of the self-assembled EH-Indigo films in low-compression conditions. Figure 4.4a shows a representative AFM height image for the low-compression film observed in Figure 4.3. Rather than a solid monolayer film or monolayer crystalline islands like oligothiophenes typically exhibit, the AFM height image shows the substrate is densely packed with crystallites that are rectangular in nature. The average length of a crystallite is 700 ± 30 nm and the average width is 150 ± 10 nm. The rectangular nature of the crystallites is unlike that seen in oligothiophenes. Because the chloroform droplet at the water surface is macroscopic and would have no preferential direction of evaporation at the water surface, the anisotropic shape of EH-Indigo crystallites indicates that the molecular packing promotes preferential growth behavior and that the forces governing the self-assembly are not uniform in all directions.

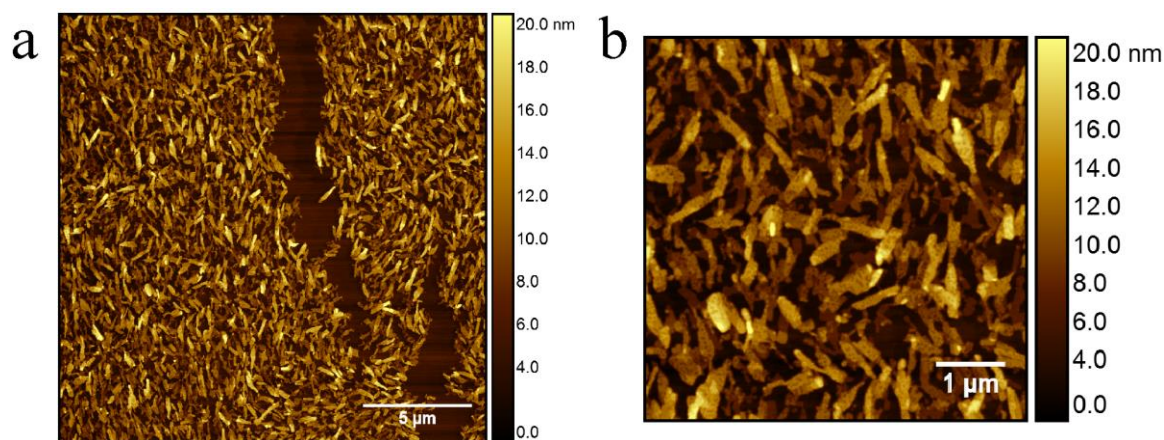


Figure 4.4. AFM imaging of EH-Indigo films at low-compression on silicon oxide. (a) AFM height image of EH-Indigo crystallite film. Scale bar is 5 microns. (b) High resolution image of film. Scale bar is 1 micron.

We observe the lack of uniformity in the thickness of crystallite growth at the air-water interface. While there is consistency between the length and the width from crystallite to crystallite, the thickness of each crystallite varies. One can observe variations in film thickness in Figure 4.3a and in a zoomed in region in Figure 4.3b. In Figure 4.5a, a high resolution AFM height image is shown of the EH-Indigo crystallite film where one can make out the extent of layer by layer growth in more detail. It is apparent that the growth of layers on top of existing layers is always incomplete. The growth is governed by the rate of chloroform evaporation from the water surface as well as the local concentration of EH-Indigo molecules and heterogeneity in this local environment gives rise to the differences in layer growth completion. However, the layer thickness itself is very uniform as shown by the height distribution in Figure 4.5b for the corresponding area shown in Figure 4.5a.

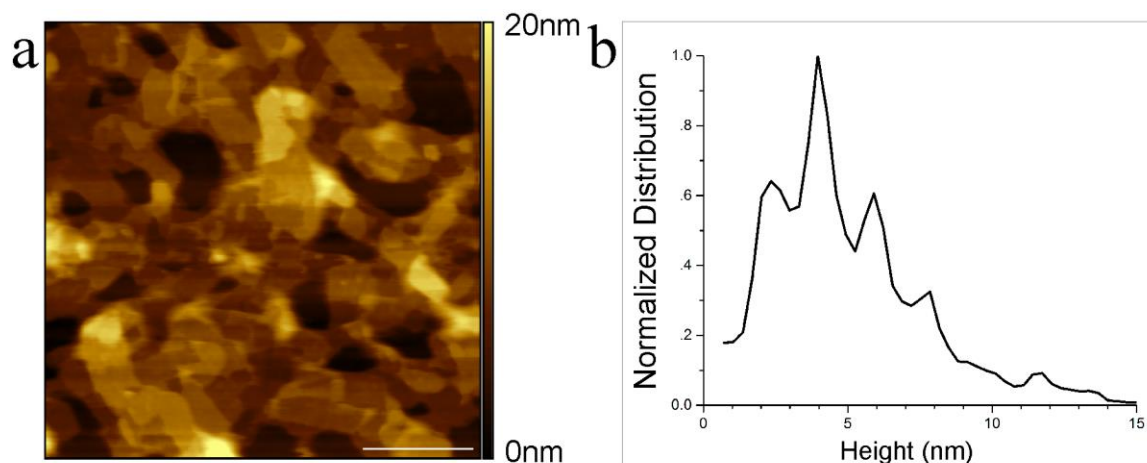


Figure 4.5. EH-Indigo crystallite morphology characterization by AFM. (a) Height image of EH-Indigo crystallites showing layer by layer growth. Scale bar is 500 nm. (b) Height distribution of (a) showing each layer is ~2 nm in height.

Each layer present is approximately 2.0nm thick. Furthermore it seems that the height of a double layer grown at the air-water interface is the same as two monolayer crystallites overlaying

each other indicating similar interactions between the top and bottom of the crystallites regardless of the number of layers in a crystallite. It is assumed from AFM imaging that there is very good order vertically in the layers of EH-Indigo crystallites.

Lateral force AFM imaging indicates that the surface termination of the crystallites is of the alkyl functional groups. Lateral force images allows one to distinguish areas of high and low friction by recording the lateral deflection signal while the AFM tip is in contact with the surface. Figure 4.6 shows a lateral force atomic force microscope experiment where the friction of a surface can be measured. The height image in Figure 4.6a shows regions of EH-Indigo crystallites on silicon oxide with different number of EH-Indigo layers present. In Figure 4.6b the corresponding friction image is shown. One can see dark regions in places where a crystallite seemingly lies flat and the layer surface is measured directly by the tip. These dark areas correspond to low friction compared to the more hydrophilic silicon oxide substrate regions as well as other, more hydrophilic, areas of EH-Indigo material.

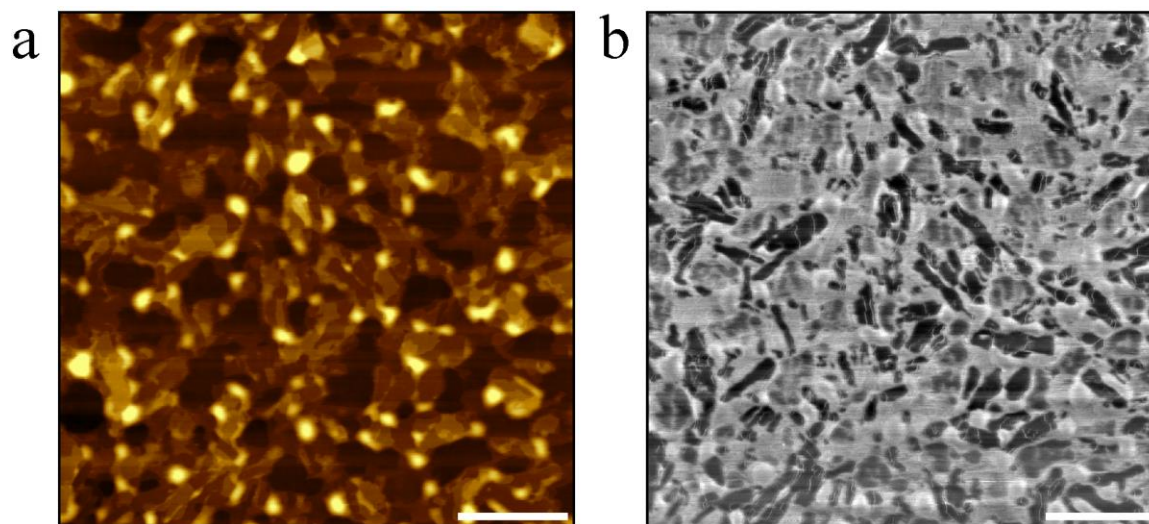


Figure 4.6. Friction imaging of EH-Indigo crystallites. (a) Height image of EH-Indigo crystallites. (b) Friction force of the corresponding image. Darker areas indicate lower friction. Scale bar in both images is 1 micron.

The alkyl chains on both sides of the EH-Indigo molecule are the most likely causes of a hydrophobic interaction with the AFM tip. The friction on the tip would be higher if it were to interact with the amine and carbonyl groups because those functional groups would interact more with the silicon surface of the tip causing more lateral force. By looking at the molecular structure of EH-Indigo one can predict two geometries where the alkyl functional group would be standing upright. One such geometry is where the indigo functional group is flat on the water with the alkyl groups pointing up in a boat-like geometry. A second is an upright geometry with the molecule perpendicular to the water surface. The crystallographic data below confirms the molecules are upright and are perpendicular to the surface. It should be noted there are bright (hydrophilic) regions on the edges of the crystallites indicating there are exposed regions of the hydrophilic groups of EH-Indigo and that the surface termination of the crystallite is different than the edge termination.

GIWAXS reveals the exact molecular packing of the EH-Indigo crystallites and shows the self-assembly at the air-water interface is driven by both π - π interactions and hydrogen bonding. Figure 4.7a shows an example GIWAXS pattern measured for a film of EH-Indigo crystallites on a silicon oxide wafer. Bragg peaks measured on the EH-Indigo crystallite film match well with the crystal structure obtained from EH-Indigo single crystals with only small rotational distortions around the indigo moiety. The crystal structure for EH-Indigo crystallites is shown in Figure 4.7b and Figure 4.7c. Figure 4.7b shows the projection down the (010) axis where the height spacing between two layers can be discerned and is 1.996Å which is in good agreement with the value as measured by AFM in Figure 4.5b. The intermolecular distance in the (100) axis between two EH-Indigo molecules is 5.803Å and in the (010) axis is 6.250Å. Furthermore, the (100) axis is dominated by π - π stacking between neighboring EH-Indigo molecules that sit face-to-face whereas the (010) axis shows no π - π interactions but instead intermolecular hydrogen bonding between the carbonyl and amine groups of two EH-Indigo molecules. The (100) and (010) plane is responsible for the shape and size of the crystallite growth on the air-water interface whereas the (001) axis controls the number of layers in the crystallite.

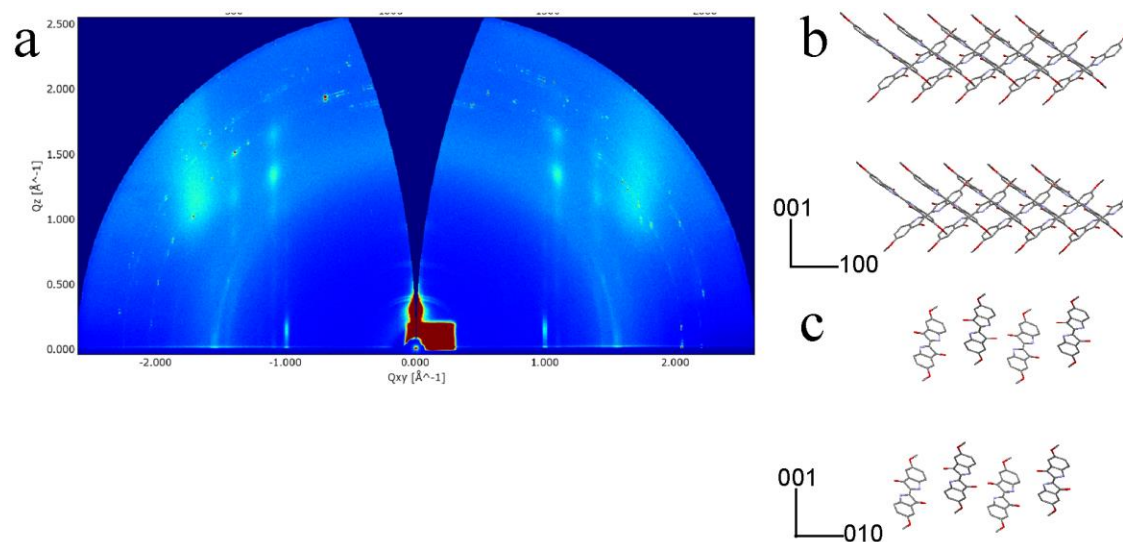


Figure 4.7. EH-Indigo Crystal Structure. (a) GIWAXS pattern of EH-Indigo on silicon oxide. (b) EH-Indigo π - π stacking interaction along the (100) axis. (c) EH-Indigo hydrogen bonding interaction along the (010) axis.

The rectangular nature of the crystallite can thus be reasoned by the competing interactions in the (100) direction and the (010) direction. The dominant interaction is the (100) π - π interaction between EH-Indigo molecules and the crystallite is longer in this direction whereas the short-axis of the crystallite is (010) and the weaker hydrogen bonding interaction. The energetics of π - π and hydrogen bonding can be comparable in polymeric systems.¹³⁹⁻¹⁴⁰ However, the intermolecular hydrogen bonding between indigo molecules is weakened by strong intramolecular hydrogen bonding that gives indigo its distinctive molecular stability.¹⁴¹⁻¹⁴² Because solution grown macroscopic single crystals show virtually the same crystal structure, the presence of water does not seem to significantly alter the energetics of crystal growth as one may expect. However the rate of growth in the (100) versus the (010) direction does become important during the LB process as the solvent evaporation will limit the extent of molecules available and the faster growth rate will dominate. An approximation based on the aspect ratio of the crystallites can be

made that the (100) direction grows ~ 4.5 times faster than the (010) direction. One could imagine if the rate of solvent evaporation was slowed down by lowering the temperature or using a higher boiling-point solvent the aspect ratio could be decreased and a more isotropic crystal shape could be achieved at the air-water interface.

4.3.2 *EH-Indigo crystallite bundle formation*

EH-Indigo crystallite films undergo dramatic morphological changes at the air-water interface if the film is further compressed and the surface pressure is allowed to reach values greater than 20 mN/m. If the same films as seen in Figure 4.3 are further compressed, large scale blue lines form on the water surface as seen in Figure 4.8. The long blue lines on the water surface are highly oriented and are on average parallel to the barriers. These large-scale aggregates are permanent and removing the compression force by removing the barriers does not revert the surface back into a thin crystallite film. These aggregates are also robust and can be deposited on substrates with standard vertical Langmuir-Blodgett deposition as well as Langmuir-Schaefer deposition. The surface pressure value at which these occur varies from experiment to experiment however the total compressed water surface area at which point these bundles form with an EH-Indigo concentration of 0.2mg/mL is consistently $\sim 75\text{cm}^2$.

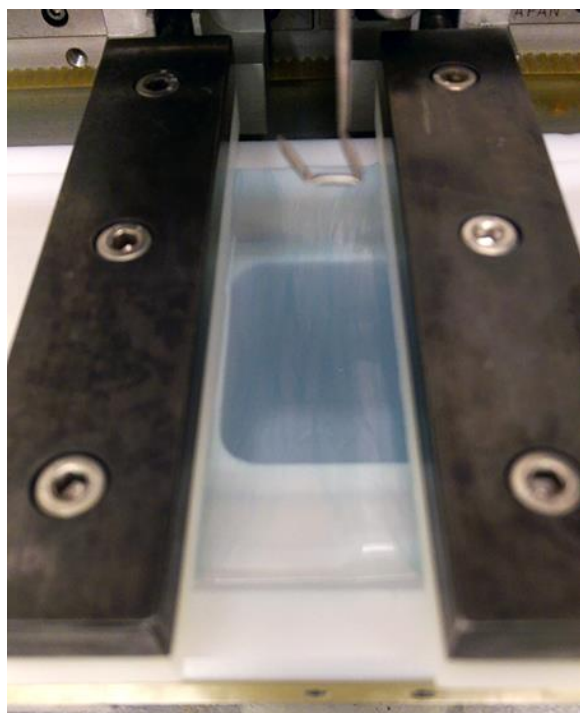


Figure 4.8. EH-Indigo macroscale aggregate formation on the water surface at high LB compression (>20 mN/m)

Imaging these large features under an optical microscope it appears the EH-Indigo crystallites further aggregate into larger bundles that are oriented. As seen by Figure 4.9a and Figure 4.9b, the length of these objects can range from microns to centimeters. The length of the aggregates on the water surface can extend from the top to the bottom of the trough but appear to sometimes crack upon deposition to the substrate. Optimization of deposition speed or the hydrophilicity of the substrate could improve the preservation of the entire length of the aggregate. The width of

individual strands is ~ 0.5 -5 microns and they aggregate together to form bundles. From the optical microscope images it is readily apparent that these films of bundles are significantly different than the thin films deposited at low surface pressure. Whereas the film looked thin and isotropic under an optical microscope with only minimal cracks in the low regime, these long fiber bundles are visibly anisotropic. Furthermore, the long axis of the macroscale bundles as deposited onto the silicon substrate is consistently perpendicular to the compression force (barriers of the Langmuir-Blodgett).

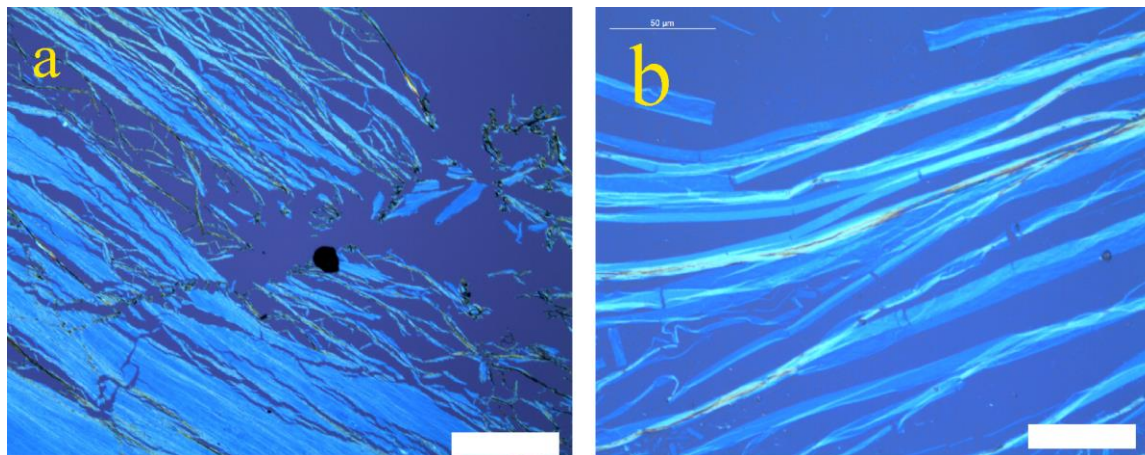


Figure 4.9. Optical microscope images of EH-Indigo bundles formed at surface compression values greater than 20 mN/m. Different regions of the same film on silicon oxide where the (a) scale bar is 500 microns and (b) scale bar is 50 microns.

The AFM height images of the EH-Indigo bundles are shown in in Figure 4.10. Individual strands seem to be composed of very densely packed crystallites that were formed initially during the solvent evaporation. Figure 4.10a shows thin strands that vary in length and height. The strands are very thick compared to the single crystallite with strands ranging 20 to 40 nm indicating single-crystallite strands are most likely not present in these bundles. The AFM image also reveals the long-axis of the strands is not a smooth continuous packing of crystallites but is more disjointed that only on average seems to point in one direction. However, on average the long axis of an individual crystallite seems to be parallel with the long axis of the strand implying that the crystallites are aggregating in an oriented way during the compression. This is also shown in a thicker strand in Figure 4.10b. The strand is approximately six microns wide but individual crystallites can be visualized with AFM that make up the strand. Furthermore, in Figure 4.10b a thin but dense film of crystallites can be observed surrounding the strand. This thin film could be a prerequisite for strand and bundle formation and can be imagined to be the first step of the self-assembly process. Compressing the crystallite film past a critical point could force the film to nucleate a three-dimensional structure that then leads to the long-range strand formation similar to a crystal nucleation prior to growth at the air-water interface.

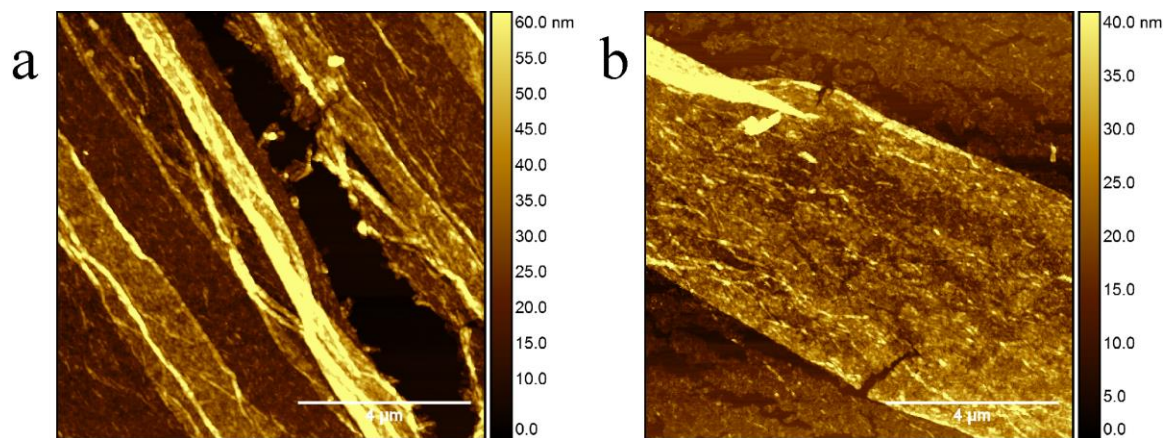


Figure 4.10. AFM imaging of EH-Indigo bundles. (a) and (b) are AFM height images of different regions of a EH-Indigo bundle film on silicon oxide. Scale bar in both images is 4 microns

What is interesting is that the compression aligns the majority of the strands and bundles into one preferential direction. There could be favorable head-to-tail inter-crystallite interactions due to electric dipole forces as this phenomena has been previously reported in nanoparticle systems.^{143,144} However, high resolution imaging to resolve the extent of head-to-tail packing was not possible on these bundles. One hypothesis for the formation of these large-scale bundles is the highly compressed monolayer or few-layer crystallite film wraps on top of itself, mimicking a scroll, which would always happen parallel with the compression barriers. Further compression induces more wrapping on top of itself and ultimately leads to a dense bundle that is visible by the naked eye. If this fiber bundle formation can be formed also by more conductive indigo semiconductor molecules, one could imagine the possibility of using this type of assembly to form highly conductive fiber bundle films and having a high degree of control of the alignment of the films relative to the charge transport direction. It is not clear as of now how much orientation exists within the bundle or strand and whether the anisotropy of the individual crystallite is extended to the macroscale aggregate. It is expected there is some degree of orientation and this orientation can be probed further with x-ray scattering and polarized photoluminescence measurements.

4.3.3 *EH-Indigo self-assembly with high solution concentration*

Preliminary work was done to study the effect of concentration and available surface area on the self-assembly of EH-Indigo. By increasing the EH-Indigo concentration in chloroform and decreasing the available surface area simultaneously the intended result is to promote the growth of larger crystals in the hopes of eventually growing single-crystals which are free of the structural defects that worsen organic device performance. The initial expectation with an order of magnitude higher in concentration is that the growth of larger anisotropic rectangular crystallites. Other effects that could contribute to self-assembly process are temperature¹⁴⁵ and choice of solvent¹⁴⁶. Instead of 0.2mg/mL EH-Indigo in chloroform, 2mg/mL solutions are prepared and deposited in pre-compressed troughs where the starting available surface area is $\sim 50\text{cm}^2$ rather than $\sim 250\text{cm}^2$ as previously seen in Figure 4.2. The EH-Indigo film that grew from these conditions and deposited onto a silicon oxide wafer is shown in Figure 4.11. Because of the increase in macroscopic aggregation and particle formation on the water surface, the entire

water surface was not covered by the film which resulted in an inhomogeneous coverage on the substrate.

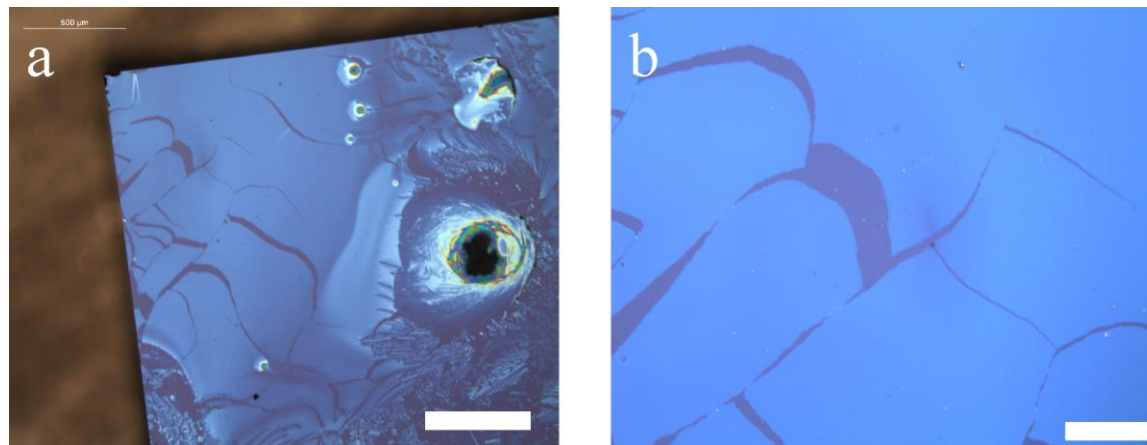


Figure 4.11. EH-Indigo film formed from 2 mg/mL concentration in a pre-compressed Langmuir-Blodgett trough. (a) EH-Indigo film where the scale bar is 500 microns. (b) Zoom in region of the film where the scale bar is 100 microns.

The immediate difference between the 2 mg/mL pre-compressed EH-Indigo film shown in Figure 4.11a and that seen in the 0.2 mg/mL concentration film in Figure 4.3 is the thickness of the film. In Figure 4.3a the thickness variation visible by optical microscopy results from different amounts of EH-Indigo crystallites from region to region. The thicker film visible in Figure 4.11a is more uniform and there does not seem to be any thickness variation over the same length scale as that in Figure 4.3. This can be better seen by the zoomed in region of Figure 4.11b, the optical contrast is constant over the entire image except for the visible cracks in the film. Also, the quantity of cracks in the film seems less than that for the lower concentration films indicating greater mechanical stability during deposition. These macroscopic observations imply that the morphology of the two EH-Indigo films is different.

AFM imaging of the more concentrated, pre-compressed EH-Indigo film reveals the increase in concentration leads to a different regime in the self-assembly of EH-Indigo at the air-water interface. Figure 4.12a shows an AFM height image of the dense film region shown in Figure 4.11b. The height of the majority of the film is ~14 nm which is approximately the size of seven EH-Indigo molecules stacked on top of each other if one assumes a similar vertical stacking geometry. Also visible is the growth of the next layer. The height of this second layer is ~2 nm which is consistent with the height of single layers of EH-Indigo molecules and crystallites formed at low concentration. The nucleation of the next layer also seems random which implies the lack of long-range order in the layers.

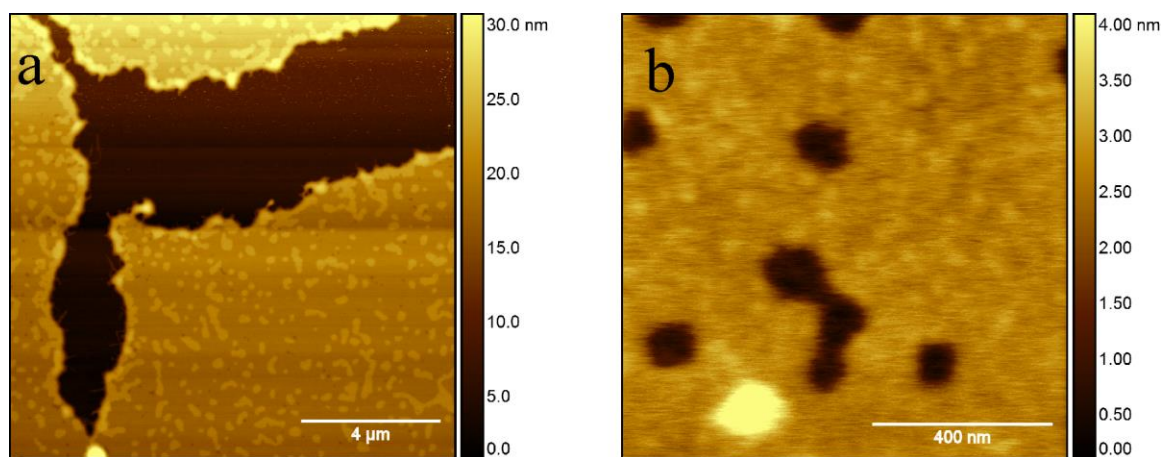


Figure 4.12. AFM height image of 2 mg/mL EH-Indigo films on silicon oxide. (a) Height image of a region with a visible crack in the film. (b) High resolution AFM height image of the EH-Indigo film morphology.

Figure 4.12b shows a zoomed in region of the AFM height image of the 2 mg/mL EH-Indigo film. The film is not atomically smooth and small height fluctuations of the film can be observed. These height fluctuations are on the order of $\sim 2\text{\AA}$ which is too small to be entire EH-Indigo molecules. The small but noticeable height variations on the longitudinal length scale of $\sim 50\text{-}100$ nm most likely means the packing of the molecules is not as crystalline as in the low-compression films. The layer is also incomplete as gaps on the order of 100 nm can be seen. These gaps have a circular or amorphous shape without straight edges implying that the termination and perhaps growth is not also not as ordered as for the low-concentration crystallites. Although this film is more uniform and thicker, if this film is indeed less crystalline than individual EH-Indigo crystallites the electronic properties would most likely suffer. Photoluminescence studies in chapter five will show the optical properties of this EH-Indigo thicker film do not match that of the low-concentration crystallites but rather match that of single molecule EH-Indigo.

4.3.4 EHT-Indigo film self-assembly

EHT-Indigo is similar to EH-Indigo except for the substitution of a thiophene functional group for the ether linking the indigo moiety to the solubilizing hydrocarbons. Thiophenes are useful for modifying the electronic structure of organic semiconductors and can influence the packing geometry of crystalline materials.⁶⁷ Preliminary studies show that EHT-Indigo does not have the same self-assembly driving forces as EH-Indigo. Figure 4.13a shows the pressure-area isotherm for 150 μL of 0.2 mg/mL EHT-Indigo after deposition from chloroform. Similar to EH-Indigo there is no noticeable difference until a sharp increase begins around 150 cm^2 . Figure 4.13b shows an optical microscope image of an EHT-Indigo film deposited at a surface pressure value of ~ 1 mN/m. There are small but noticeable differences in the EHT-Indigo films compared to EH-Indigo. Firstly, the amount of gaps in the film from cracking is less. The EHT-Indigo film seems much more continuous. Secondly, the optical contrast is much less between the silicon oxide substrate and the film indicating that the thickness of the film is less than that of the EH-Indigo films. The appearance of striation patterns in Figure 4.13 could be due to varying thickness of the film but it is much more uniform than that seen in Figure 4.3 for EH-Indigo. Whereas for EH-Indigo the areas of varying thickness seemed to be random, EHT-Indigo seems

to vary in thickness in an oriented direction. However, is not clear from these preliminary studies whether the variation in thickness is due to the film growth during chloroform evaporation or is from the compression of the film prior to deposition.

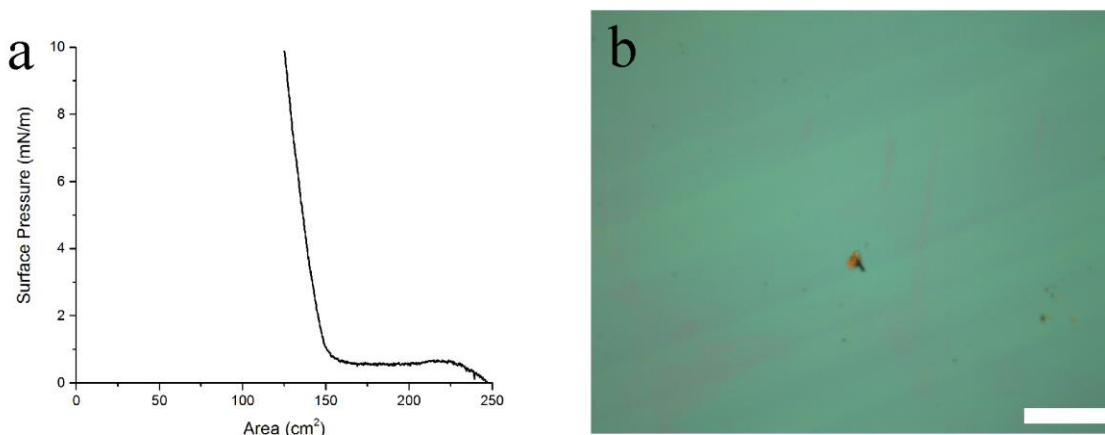


Figure 4.13. EHT-Indigo Langmuir-Blodgett film self-assembly. (a) Surface pressure-area compression isotherm. (b) Optical microscope image of an EHT-Indigo film on silicon oxide. Scale bar is 200 microns.

AFM height images of EHT-Indigo films reveal different nanoscale morphology than that of EH-Indigo. Whereas EH-Indigo self-assembled into individual anisotropic crystallites, EHT-Indigo seems to form much more isotropic islands. Figure 4.14a shows an AFM height image of a dense EHT-Indigo film with a crack present in the lower right side of the image. The thickness of the EHT-Indigo film is approximately 1 nm. Figure 4.14b shows a different region of the same film that is less dense and individual islands can be discerned. Similar to oligothiophene islands in chapter three, EHT-Indigo forms more rounded islands than that of the rectangular EH-Indigo crystallites.

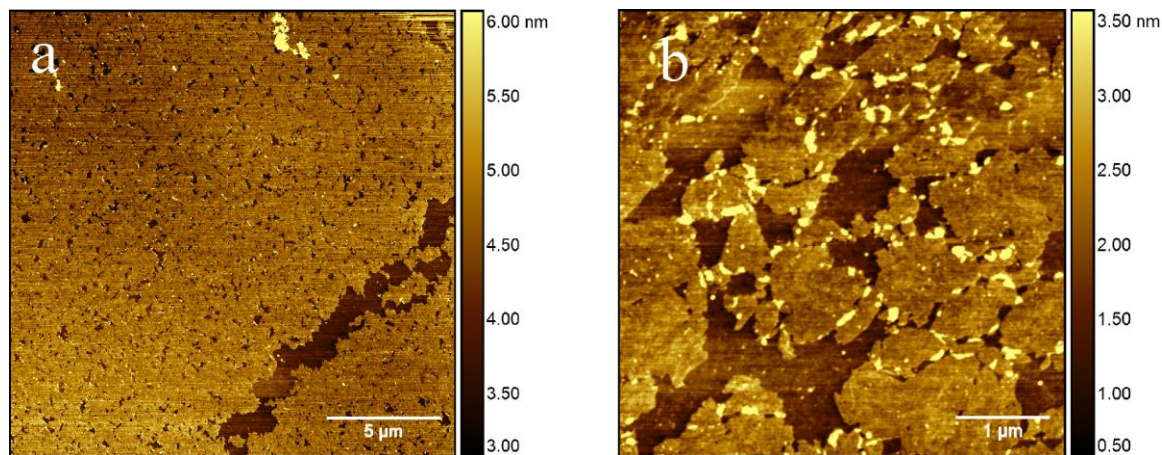


Figure 4.14. AFM height imaging of EHT-Indigo film on silicon oxide. (a) AFM height of a EHT-Indigo film with a crack present in the film. (b) Region of film with less dense regions of the EHT-Indigo film.

A GIWAXS measurement of EHT-Indigo films on silicon oxide is shown in Figure 4.15a. A smeared Bragg peak can be faintly seen at a value of 1.005 \AA^{-1} . This corresponds to a periodicity at $6.44 \text{ \AA} \pm 0.19 \text{ \AA}$. The calculated crystal structure of an EHT-Indigo single crystal grown from THF is shown in Figure 4.15b-d. Figure 4.15b shows the projection of the crystal structure along the b-axis which shows the spacing between two neighboring EHT-Indigo molecules if the molecules were lying flat on the substrate. This spacing is measured as 6.32 \AA . While not a complete characterization of the EHT-Indigo film on silicon oxide, the good agreement implies the EHT-Indigo molecules are lying flat on the substrate in a similar geometry to the single crystal structure. In this way, EHT-Indigo shows a similar tendency to EH-Indigo at the air-water interface to mimic the single crystal structure and could be due to the strong intermolecular π - π interactions in both systems.

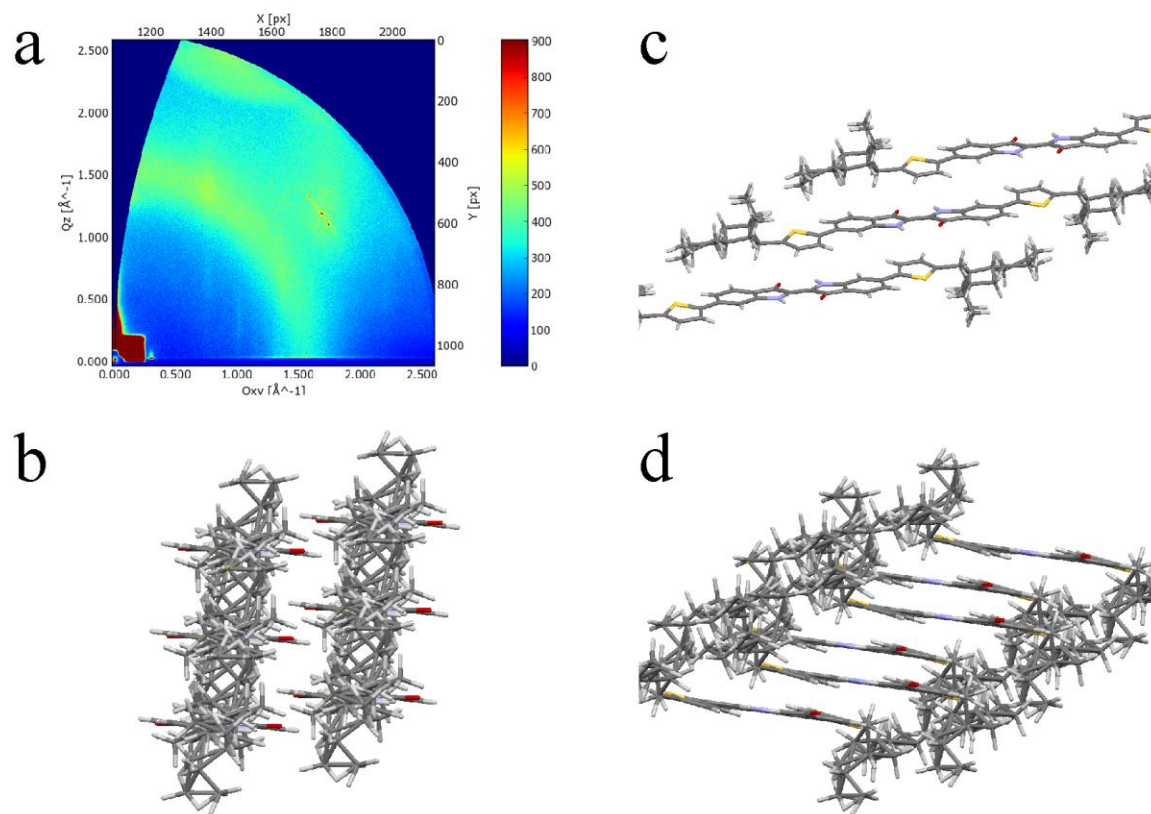


Figure 4.15. EHT-Indigo X-ray scattering. (a) GIWAXS pattern of few-layer EHT-Indigo on silicon oxide. (b)-(c) Visualization of crystal structure calculated from GIWAXS of an EHT-Indigo single crystal from a saturated solution in THF.

However unlike EH-Indigo, EHT-Indigo has entirely isotropic intermolecular interactions in the lateral plane of the film. Laterally there are only weak hydrogen bonding interactions whereas the z-direction of the film is the π - π stacking direction. Because of this one can understand why the morphology of the EHT-Indigo islands match those of oligothiophenes as there is no competition between different intermolecular forces as there is in the case of EH-Indigo. Furthermore, the vertical stacking does not show complete overlap between neighboring EHT-Indigo molecules as there is a slight lateral shift. The shift is due to the donor-acceptor nature of

EHT-Indigo. The thiophene group on one molecule can act as donor group to the indigo group on another molecule which acts as the acceptor.

EHT-Indigo shows a completely different behavior with conductive substrates than that of EH-Indigo. EH-Indigo cannot be transferred from the air-water interface to conductive substrates whereas EHT-Indigo seemingly can. Figure 4.16 shows two examples of an EHT-Indigo film that was successfully deposited on a conductive substrate. Figure 4.16a shows an AFM height image of EHT-Indigo on highly doped p-type silicon with only native oxide. The lack of a thick silicon oxide prevents EH-Indigo from depositing but not EHT-Indigo. The same is true for HOPG as can be seen in Figure 4.16b.

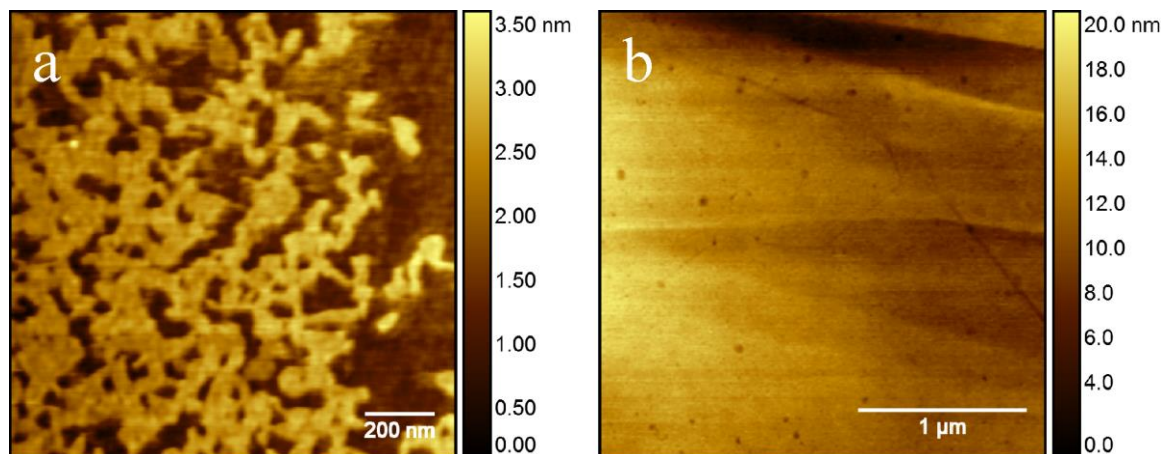


Figure 4.16. EHT-Indigo films on conductive substrates. (a) AFM height image of EHT-Indigo film on highly doped p-type silicon with native oxide. (b) AFM height image of EHT-Indigo film on HOPG.

The exact nature of this discrepancy most likely is due to difference in the orientation of the π -plane of the molecule in the packed crystal relative to the water surface. One can imagine that EHT-Indigo film on the water surface has the electrical dipole oriented on the water surface in a direction that is favorable for interaction with conductive substrates when deposited whereas EH-Indigo is perpendicular to this orientation and this is unfavorable.¹⁴² However, it is also possible that the EHT-Indigo molecules somehow rearrange during the deposition process into a more favorable electronic geometry whereas EH-Indigo is not due to the higher crystallinity of EH-Indigo crystallites. Performing in-situ x-ray characterization¹⁴⁷⁻¹⁴⁸ at the air-water interface for both EHT-Indigo and EH-Indigo would reveal the true crystal structure after self-assembly but prior to deposition.

4.4 Conclusion

Indigo small molecules were studied for their self-assembly properties at the air-water interface. After solution deposition onto the water surface, EH-Indigo grows into crystallite films. The crystallite films range from one monolayer to few-layers thick. The morphology of the film is anisotropic and rectangular in nature. The average aspect ratio of the rectangular crystallite is ~ 4.5 and the anisotropic self-assembly is driven by the different intermolecular interactions

present in the crystal structure. The long-axis of the crystallite is the π - π stacking direction where the molecules are closer to each other than the short-axis with predominately weaker hydrogen bonding interactions. However, further compression of the EH-Indigo crystallite films wraps the crystallites together into a bundle that spans the length of the air-water interface producing compact assemblies of individual crystallites. The anisotropy is not preserved when a EH-Indigo solution an order of magnitude higher in concentration is used in a pre-compressed Langmuir-Blodgett trough. Rather than forming larger crystallites, the entire morphology is different as the EH-Indigo grows into a multilayer film that is continuous but not crystalline. The role of local concentration in the crystallization process of EH-Indigo should be further studied to understand the nature of the anisotropic growth and how to promote larger crystallite growth

Furthermore, the anisotropy of EH-Indigo is contrasted with the more isotropic self-assembly behavior of EHT-Indigo. EHT-Indigo forms a uniform macroscale film as the nanoscale geometry of the islands is isotropic in nature and can be more easily compressed into a quasi-smooth film. The growth of rounded islands is expected as there is no anisotropy in the lateral plane of the crystal structure. Interestingly the GIWAXS crystal structure indicates that the addition of the thiophene unit aligns the molecules parallel to the water surface rather than perpendicular as in the EH-Indigo case. Whereas for field-effect transistors a perpendicular geometry is necessary, for photovoltaics or diodes a planar geometry is required with the π -plane lying flat on the substrate. The insertion of thiophene groups makes the indigo small molecule applicable for two different geometries and electronic applications. This synthetic flexibility is important for optimizing the ideal material for the ideal organic electronic application.

5 Optoelectronic Active Aggregate Formation in Indigo Films and Graphene Field-Effect Transistors

Abstract

The photophysics and electrical properties of EH-Indigo and EHT-Indigo films were studied in this chapter as well as a graphene-based field effect transistor was fabricated and tested for the purposes of studying monolayer and few-layer organic films. Solid-state photoluminescence measurements on EH-Indigo and EHT-Indigo exhibit optical signatures of H-aggregate formation in the form of a large photoluminescence redshift compared to single molecule in solution. In addition, time resolved photoluminescence spectroscopy reveals the lifetime of EH-Indigo is significantly shortened when in crystallite form compared to single molecule in solution. The structure of the EH-Indigo crystallites and EHT-Indigo film combined with the photoluminescence measurements indicate the presence of H-aggregation between neighboring molecules. Electrical characterization by KPFM further indicates there is electrical connection between EH-Indigo molecules within a crystallite and between crystallites when in a dense film. The necessity of flat field-effect transistors is discussed and a suitable graphene fabrication process for achieving flat field-effect transistors is presented.

5.1 Introduction

The local environment has a large influence on the optical properties of organic dye molecules.¹⁴⁹ Specifically, the extent of aggregation in an organic molecular dye system has been shown to exhibit unique absorbance and photoluminescence properties relative to that of the single molecule.¹⁵⁰⁻¹⁵⁴ For organic electronics the coupling of molecules together is a desirable trait as the amount of coupling determines how efficient charge transfer can be monomers in an active film.¹⁵¹⁻¹⁵² Certain molecular aggregates can be described by J-aggregates and H-aggregates.¹⁵⁵⁻¹⁵⁶ In J-aggregates the absorption band of the aggregate is red-shifted with respect to the single molecule whereas in H-aggregates the absorption blue-shifts. In J-aggregates, two chromophores are oriented head-to-tail whereas in H-aggregates it is face-to-face as shown in Figure 5.1.

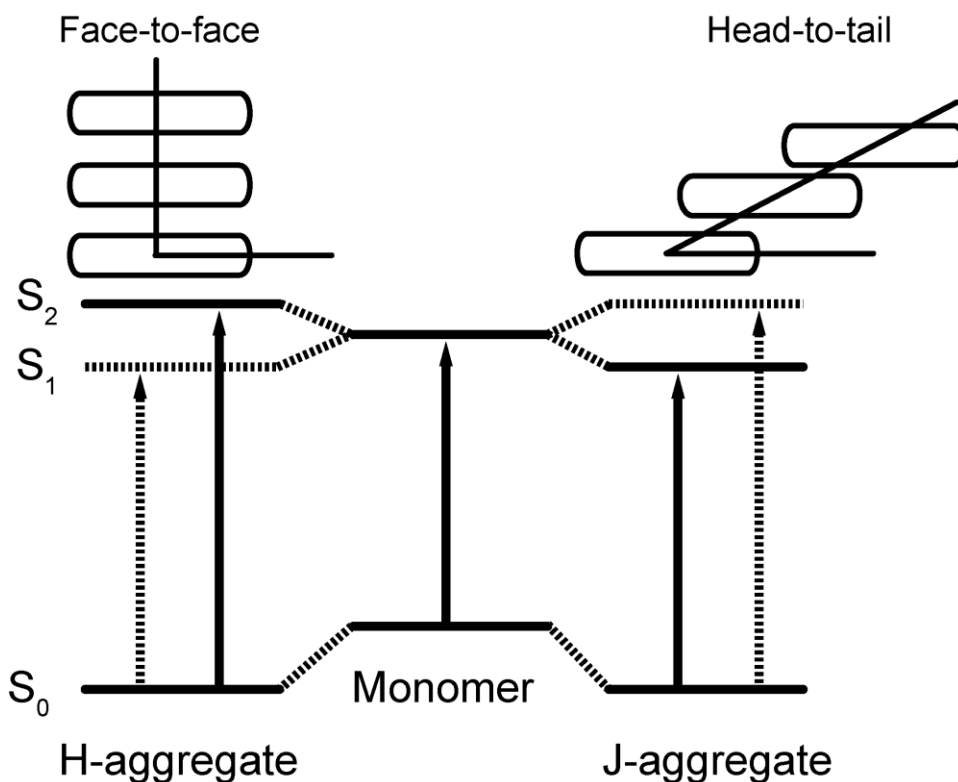


Figure 5.1. Energy diagram of H-J aggregate formation in a molecular dimer system. In J-aggregates the molecule packing is head-to-tail and causes an absorbance and fluorescence redshift. In H-aggregates the packing is face-to-face and the fluorescence shows a blueshift.¹⁵⁶

In addition to the change in the absorbance and emission peaks, the excited-state radiative decay rate is decreased in H-aggregates and increased in J-aggregates. Photoluminescence spectroscopy is a good technique to probe HJ-aggregate formation in organic molecular systems such as thiophenes.¹⁵⁷⁻¹⁵⁸ Although the properties of molecular indigo and indigo derivatives have been extensively studied in the solution phase^{120, 159-160}, aggregation effects on the photophysics of crystalline indigo molecular solids have not

been as developed. Costa and coworkers¹⁶¹ reported the presence of J-aggregates in a layered indigo-carmin hybrid material indicating that indigo is indeed capable of aggregation. With recent developments in active indigo materials for organic electronics, it is important to better understand the coupling of indigo molecule to each other to increase the charge transfer efficiency and improve device performance.

In addition to the optical coupling it is important to study the electronic coupling of organic molecules for optoelectronic applications. Field-effect transistors are an important tool to study the electronic properties of conductive films.¹⁶²⁻¹⁶⁴ Top-contact electrodes are fabricated using shadow masking and result in the deposition of electrodes on top of the active material. However, the fabrication process often times yields poorly defined electrode boundaries as well as introducing metal contaminants that can damage the integrity of the organic film.¹⁶⁵ While bottom-contact electrode geometries have proven very successful, the use of standard bottom-contact FETs are not practical for studying very-thin organic films as the thickness of the film may be an order of magnitude smaller than the height of the electrode. Figure 5.2a demonstrates the situation of a conductive organic monolayer deposited between two electrodes that are taller than the actual height of the monolayer. The conduction pathway between molecules is broken and the monolayer will no longer be conductive. A better alternative is to use coplanar or flat electrodes as shown in Figure 5.2b. In this example the electrodes are coplanar with the insulating channel material and there is no step height between the electrode and the channel region.

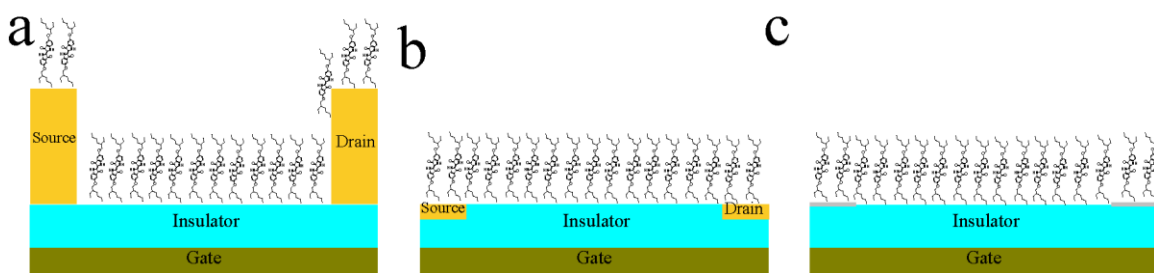


Figure 5.2. Field-effect transistor geometries for thin organic films. (a) Standard fabrication with bottom-contact source and drain electrodes. The electrodes are typically tens of nanometers in height above the insulator. (b) Coplanar source-drain electrodes with the insulating oxide layer. (c) Graphene field-effect transistor with monolayer graphene (~1 nm in height) on top of the insulator layer.

This is an ideal situation where the structure of the monolayer or thin film is preserved. Protocols exist for the fabrication of coplanar or flat electrodes but the reproducibility and ease in achieving working FETs leaves a desire for a more practical approach.¹⁶⁶⁻¹⁶⁷

Graphene electrodes have been shown to perform remarkably well when utilized as FETs¹⁶⁸⁻¹⁶⁹ and graphene patterning has become routine with photolithography.¹⁷⁰ As Figure 5.2c shows, the graphene electrode on top of the oxide is not coplanar with the channel region but is less severe compared to the situation presented in Figure 5.2a. The theoretical height of one graphene layer is only 3.35Å and would not cause a large perturbation to the film structure. Combining the advancement in photolithography with the excellent electronic properties of graphene will allow for the fabrication of graphene

FETs that serve as an easy platform to perform fundamental electronic studies on very thin (<5 nm) films.

This work studies the photophysical properties of the self-assembled EH-Indigo and EHT-Indigo films. The absorbance and photoluminescence of the indigo films made in chapter four are measured and contrasted with the solution properties. EH-Indigo crystallites are shown to contain H-aggregates by photoluminescence spectroscopy. The absorbance of EH-Indigo in crystallite phase shows a small blue-shift in absorbance but also a very large red-shift in photoluminescence. Furthermore the radiative lifetime is an order of magnitude less in the crystallite phase. Equally, EHT-Indigo is found to show photoluminescence signatures of aggregation and most likely H-aggregate formation as well. On the other hand the highly concentrated, pre-compressed EH-Indigo film is found to contain no aggregates by photoluminescence spectroscopy. The electronic properties of EH-Indigo are studied using bottom-contact gold field-effect transistors by KPFM and CAFM. KPFM measurements provide evidence for electrical connection between distinct crystallites when in a dense film assembly. With the bottom-contact geometry CAFM was not able to measure lateral current across the crystallite film as standard gold electrodes are too tall for such a short film. Alternatively the fabrication of graphene field-effect transistors is presented using routine photolithography techniques found in standard fabrication facilities. The graphene FETs are characterized for their cleanliness and electrical properties as well as preliminary tested using EHT-Indigo films.

5.2 Experimental

Photoluminescence spectroscopy and imaging were performed on an inverted confocal microscope. The sample was optically excited using linearly polarized, pulsed (5 ps; 40 MHz) excitation centered at 630 nm with continuous-wave equivalent powers ranging from 1 - 20 μ W. Optical excitation was focused and photoluminescence was collected by the same objective (Nikon 100 \times , 0.95 NA) in a reflection configuration. The collected photoluminescence was passed through multiple interference filters to remove the laser excitation and then collected on a single-photon counting avalanche photodiode (MPD Technologies) for imaging or spectrally analyzed with a spectrometer (Acton) connected to a charge-coupled device (CCD) camera (Princeton Instruments). A time-correlated single-photon counting (TCSPC) device (PicoHarp) was used to record the photoluminescence decay dynamics with a temporal resolution of \sim 50 ps. Measurements of the film were performed on glass substrates. Solution measurements were performed using a cuvette with an optically polished bottom surface. For imaging, the same inverted confocal microscope was used, but the sample was instead optically excited using 700 μ W of linearly polarized continuous-wave (CW) excitation at 633 nm.

AFM images were obtained on an Agilent 5500 (Keysight Technologies, Santa Rosa, CA, USA) using OMCL-AC240TM probes (Olympus Micro Cantilevers, Japan) which have a 20 nm platinum coating with a titanium adhesion layer on the tip side and a nominal resonant frequency value of 70 kHz with a nominal spring constant of 2 N/m. The tip radius is 15 nm. Kelvin probe force microscopy was performed using a tip bias of

$V_{AC} = 2V$ with a frequency of 2 kHz using a HF2LI lock-in amplifier (Zurich Instruments AG, Switzerland). Conductive AFM images were obtained under ambient conditions using CONTV-PT probes (Bruker, Camarillo, CA, USA) with a nominal force constant of 0.2 N/m and a load of $\sim 5nN$. Voltage biases were applied to the sample and the current was collected through the tip which was held as ground. Humidity was controlled by blowing dry nitrogen or nitrogen bubbled through water into the enclosed AFM chamber. AFM images were analyzed using Gwyddion SPM data analysis software. All measurements were performed at 298K.

Highly doped p-type silicon wafers with 300 nm thermal oxide served as FET substrates for conductive measurements. Source/drain electrode fabrication was performed in the UC Berkeley Nanolab facility. UV photolithography is used to pattern the wafer and 5 nm Ti / 50 nm Au was deposited before removing the photoresist with acetone. Channel length is 20 microns and the channel width is 1mm for the mask used. The FET substrates were used as deposition substrates during EH-Indigo Langmuir-Blodgett.

Graphene field-effect transistors were fabricated using standard UV photolithography techniques. Monolayer graphene on 300 nm silicon oxide / highly doped silicon substrates were purchased from Graphene Supermarket (Calverton, NY, USA). The graphene was copiously rinsed with isopropanol and acetone prior to use. A layer of ma-P 1215 photoresist (micro resist technology GmbH, Germany) was pipetted onto the graphene and spuncoat for 30 seconds at 3000rpm. The photoresist was exposed to 340 nm UV light for 10 seconds ($\sim 140 \text{ mJ/cm}^2$) and developed using mAD 331 (micro resist technology GmbH, Germany). The exposed graphene was etched using 50W oxygen plasma for 15 seconds. The residual photoresist was removed with acetone. The graphene substrate was further soaked in 1M hydrochloric acid for 30 minutes to clean off residual carbon species.

5.3 Results and Discussion

5.3.1 *Optical H-aggregate formation in EH-Indigo and EHT-Indigo Films*

EH-Indigo forms crystalline solid structures that change the photoluminescence properties compared to the single molecule behavior in solution. Figure 5.3 shows the optical properties of a 0.2 mg/mL solution of EH-Indigo in chloroform. The solution absorbance spectrum shows an absorbance peak maximum at 647 nm and the photoluminescence spectrum of the solution shows an emission peak maximum at 679 nm which is consistent with the small Stokes shift typically seen in dilute solutions of organic dyes. Previous measurements report the $\lambda_{abs(max)}$ is 610 nm and the $\lambda_{PL(max)}$ is 653 nm for the free indigo molecule in dimethylformamide.¹²¹ While different, the values are close enough to expect the addition of hydrocarbons to not play a significant role in the solution photophysics of EH-Indigo and that the solution measurement represents single molecule behavior.

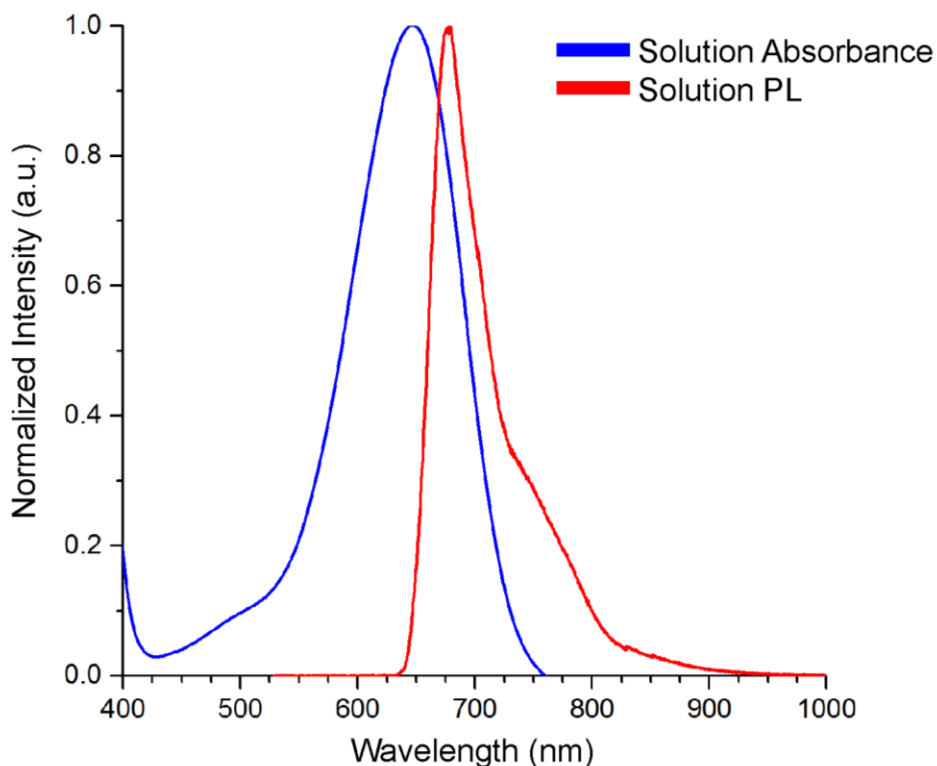


Figure 5.3. EH-Indigo solution in chloroform absorbance and photoluminescence spectrum

The effect of placing EH-Indigo into crystalline structures has on the photophysics can be studied by measuring the PL of Langmuir-Blodgett films. Figure 4.5a shows an AFM height image of an EH-Indigo crystallite film on silicon oxide as seen in chapter four. Figure 5.4b shows an example map of the PL of the same EH-Indigo crystallite film. The sample position is raster scanned (i.e. the point of laser excitation and emission changes) in the same way an AFM raster scans for topographical features. With a 633 nm excitation the laser should excite EH-Indigo close to the absorbance peak and the photons emitted as a result collect on the detector. However, every pixel is still diffraction limited so the spatial resolution is not as high as that of an AFM height image. For a 30 micron scan and 128 pixels, the average pixel size is $\sim 230 \text{ nm}^2/\text{pixel}$. However, even with this diffraction limited mapping it is still possible to see PL variation among the film. Also, a large bright region is seen in the lower right region of the image. This heterogeneity is most likely due to a difference in the amount of crystallites in the different areas of the image, where more crystallites would lead to more excitation and emission. It should be noted the location of the two images is not the same as finding the same area without guiding markers is difficult however the photoluminescence behavior of EH-Indigo crystallites is not expected to change across the substrate.

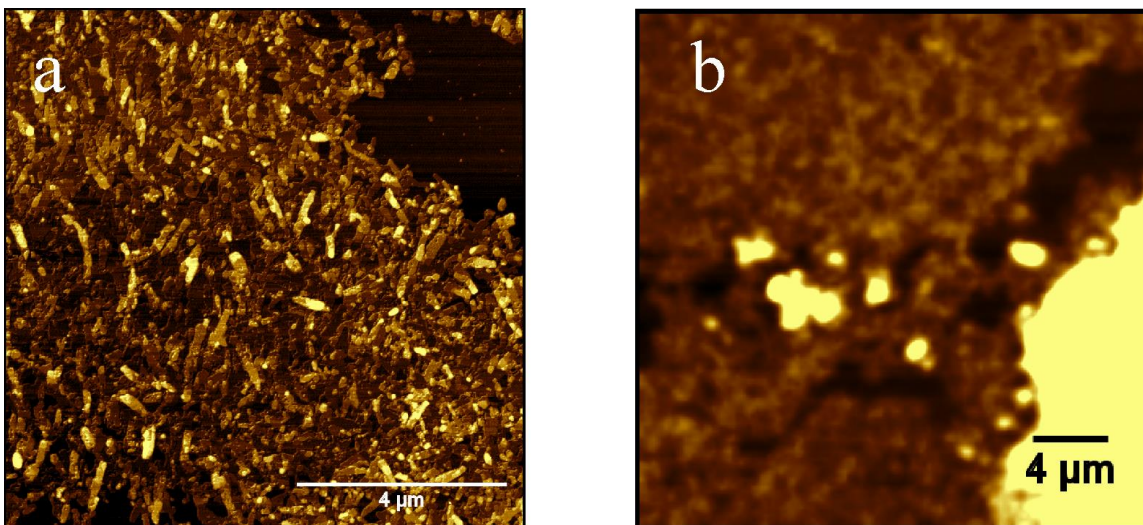


Figure 5.4. EH-Indigo crystallite film on silicon oxide. (a) AFM height image. (b) Map of photoluminescence in a different region of the same film. The color intensity scales linearly with photon counts.

More detailed analysis of the absorbance and PL spectra of EH-Indigo crystallite films reveal the effects aggregation has on the photophysical behavior of EH-Indigo. Compared to EH-Indigo single molecules in chloroform, the EH-Indigo crystallite absorbance shows a small blue-shift with an absorbance peak maximum at 641 nm (Figure 5.5). A blue-shift in the absorbance is expected in the case of H-aggregates when the dipoles of dye molecules are aligned in a parallel geometry whereas a red-shift is expected in the case of J-aggregates when the dipoles are aligned in a head-to-tail fashion.^{171,151} The amount of blue-shift or red-shift depends on the degree of alignment. More perfect alignment yields a larger shift. The PL spectrum of EH-Indigo crystallites reveals the photoluminescence of crystallites is significantly different than that of the solution phase. Figure 5.5 shows the EH-Indigo crystallite photoluminescence has its peak maximum at 777 nm which is a large red-shift ($\sim 320\text{meV}$) compared to the solution measurement. Furthermore, inhomogeneous broadening at lower energies due to phonon sidebands can be seen as a result of EH-Indigo being self-assembled into a solid crystal state.¹⁷² The origin of the large red-shift in the crystallite state is not assumed to be due to excimers because both the solution and crystallite PL show similar vibronic progression.¹⁷³⁻¹⁷⁴ Because the EH-Indigo crystallite absorbance spectrum does not exhibit a significant red-shift compared to the solution, as one may expect from J-aggregation, we propose that the large red-shift for the crystallite PL is due to the presence of H-aggregates and not J-aggregates. This H-aggregation would also coincide with the face-to-face molecular packing geometry of the crystallites seen in chapter four.

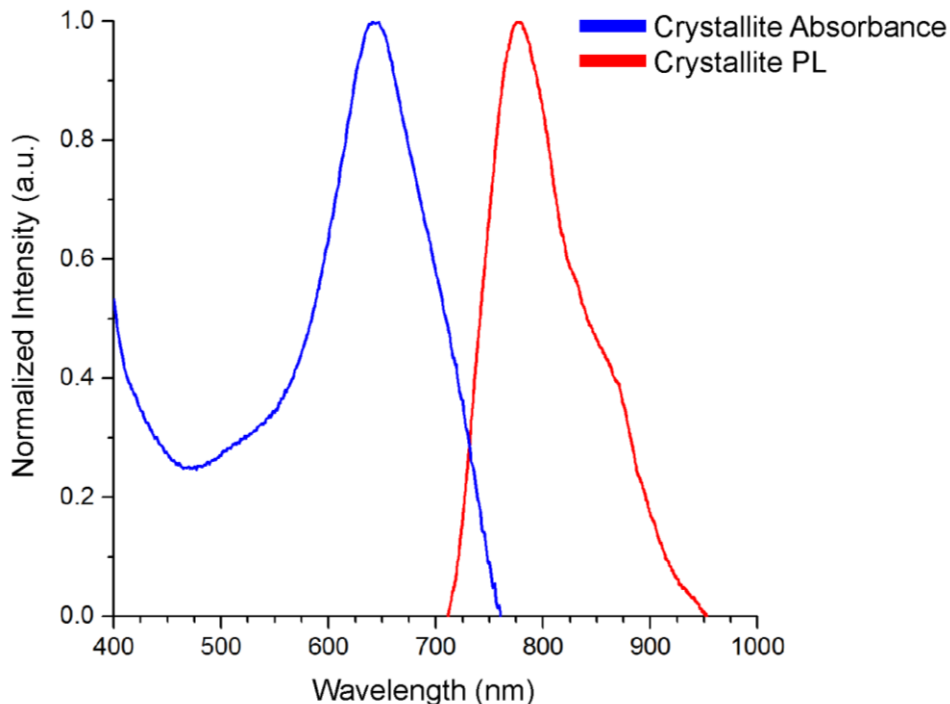


Figure 5.5. EH-Indigo crystallite film absorbance and photoluminescence spectrum

Time resolved photoluminescence measurements can be used to elucidate further the nature of the type of molecular aggregation in crystallite EH-Indigo. In H-aggregates, the excitons relax to the bottom of the excited band after excitation and the radiative rate in turn becomes low due to the dipole forbidden transition.¹⁵¹ It has already been shown that the indigo group favors radiationless transition due to the small energy gap between S_1 and S_0 .^{121,120} Figure 5.6 shows the PL decay curves for the solution of EH-Indigo and the EH-Indigo crystallite film. The PL decay of the EH-Indigo solution is monoexponential with a lifetime of 1.26 nanoseconds. Measuring the PL decay of the EH-Indigo crystallites reveals that the crystallite decay is comparable to that of the instrument response function (IRF), which is the fast limit of detection for lifetime. Taking the IRF into account, a conservative estimate for the EH-Indigo crystallite lifetime is ~ 50 picoseconds. The spacing between two EH-Indigo molecules in the (100) direction is approximately 5.8\AA which means for a perfect crystallite ~ 700 nm in length there are close to 1200 EH-Indigo monomers face-to-face. The order of magnitude decrease in lifetime for the crystallites is to be expected as the lifetime of excited states in organic dyes scales inversely with the number of individual monomers in an aggregate.¹⁷⁵ The photoluminescence properties of EH-Indigo crystallites formed at 0.2 mg/mL vary greatly from those formed from 2.0 mg/mL solutions.

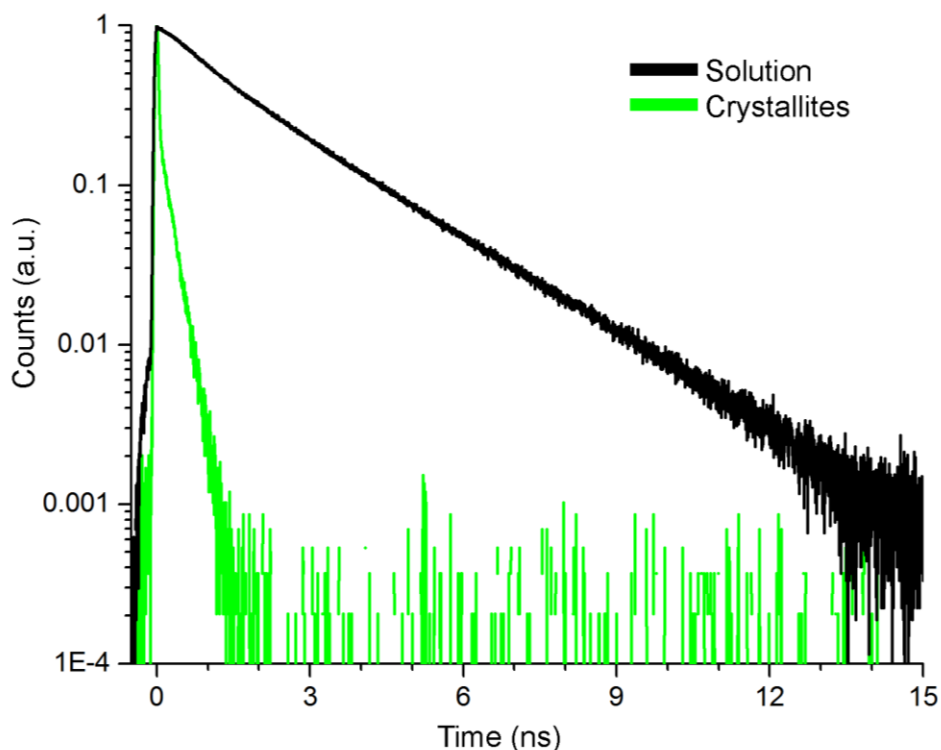


Figure 5.6. Photoluminescence lifetime of EH-Indigo in solution and EH-Indigo crystallites

A preliminary PL measurement of the concentrated EH-Indigo film reveals the lack of crystallinity and optical aggregates in the thick film. Chapter four showed the morphology of concentrated films formed at the air-water interface when 2.0 mg/mL EH-Indigo solution is deposited in a pre-compressed surface area and that the morphology is much different than that of individual crystallites formed at lower concentrations. Figure 5.7 shows the PL spectrum of the concentrated EH-Indigo film compared to the absorbance of EH-Indigo solution (0.2 mg/mL). The emission peak maximum matches closely to that of EH-Indigo in solution indicating that there is no aggregation between EH-Indigo molecules in the thick film geometry. However, the emission peak for the concentrated film is significantly broadened. This broadening hints at a large concentration of defects and heterogeneous local environments for single EH-Indigo molecules in the concentrated film.¹⁷² In addition, the laser excitation power used for the concentrated film is $\sim 20 \mu\text{W}$ whereas for the EH-Indigo solution it is only $\sim 1 \mu\text{W}$. The increase in power could raise the local temperature of the film and also induce broadening of the emission peak due to the excitation of other phonon bands.

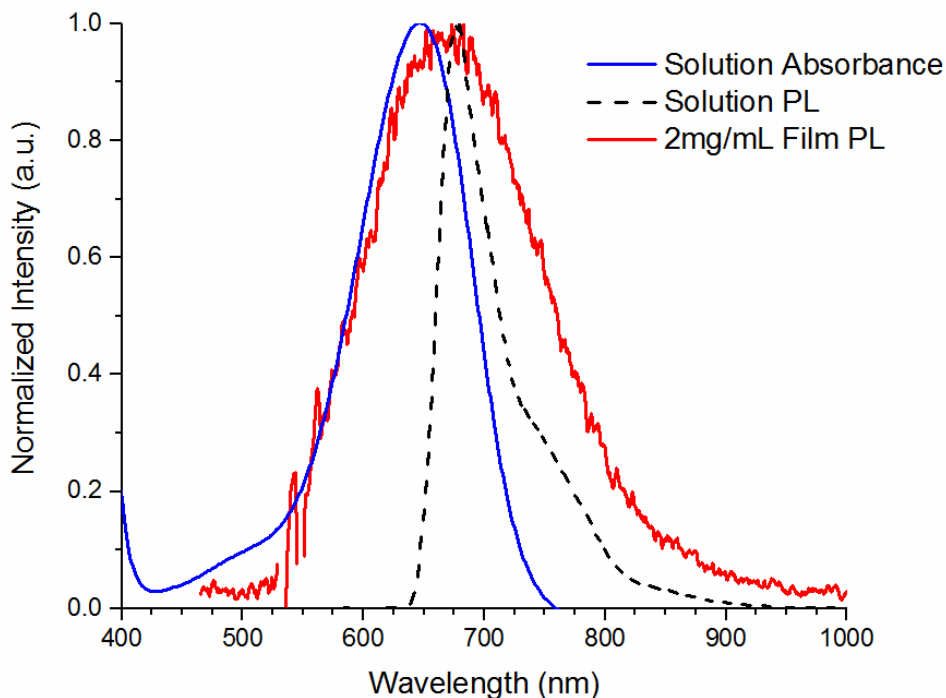


Figure 5.7. Photoluminescence of a concentrated 2 mg/mL EH-Indigo Langmuir-Blodgett film compared with the photophysics of EH-Indigo in solution

EHT-Indigo films also exhibit signatures of H-aggregate formation. As previously shown in chapter four, EHT-Indigo self-assembles with significant π - π interaction between neighboring molecules vertically in a face-to-face geometry. Figure 5.8 shows the absorbance spectrum of a 0.2 mg/mL EHT-Indigo in chloroform. When a 630 nm laser is used to excite EHT-Indigo films an emission peak with a maximum at 721 nm is observed. This is a large redshift of ~ 296 meV which, while smaller than the red-shift observed in EH-Indigo crystallite, is still considerably larger than the expected stoke shift. The broader nature of the emission of EHT-Indigo compared to EH-Indigo corresponds to the lesser degree of crystallinity in EHT-Indigo films as expected from the crystal structure and AFM morphology. The full width half max (FWHM) of the emission peak is related to the fluorescence lifetime.¹⁷² The increase in FWHM for the EHT-Indigo film is also observed as in the case of EH-Indigo crystallites and so a similar a decrease in lifetime is expected.

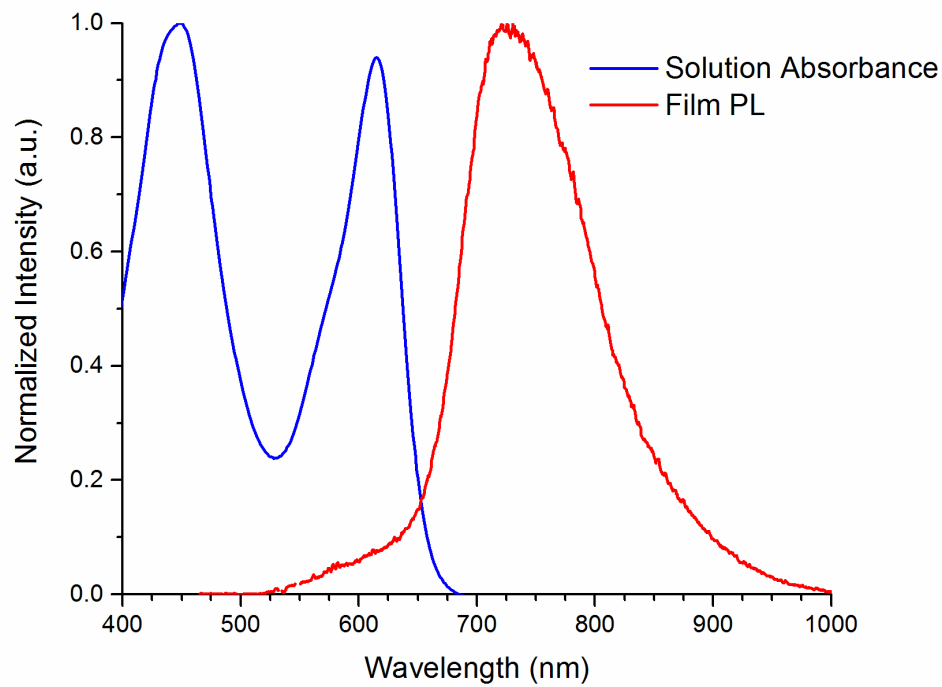


Figure 5.8. EHT-Indigo film photoluminescence

5.3.2 Conductive AFM and KPFM of EH-Indigo

The charge transport properties of EH-Indigo can be studied using KPFM and CAFM. EH-Indigo crystallite films have the π - π stacking direction parallel to the substrate after deposition from a Langmuir-Blodgett trough so when the crystallite films are placed in the channel of a FET the charge transport should be preferential across the source-drain electrodes. A compilation of KPFM measurements of a Langmuir-Blodgett EH-Indigo film deposited between gold electrodes at different electrical biasing is shown in Figure 5.9. The gold electrode contact is approximately 50nm in height and the height scale is cropped to give better contrast to the EH-Indigo film. The region shown in Figure 5.9a film is very densely packed with crystallites and there is a minimal amount of exposed silicon oxide substrate. The CPD shows that the EH-Indigo film and the gold are approximately at the same potential with additional bias applied to the source or gate electrode. After establishing the CPD of the film with no bias applied, a -9V bias is applied to the highly doped silicon gate underneath the film. Figure 5.9b shows the CPD after 20 minutes of applying a constant -9V gate bias.

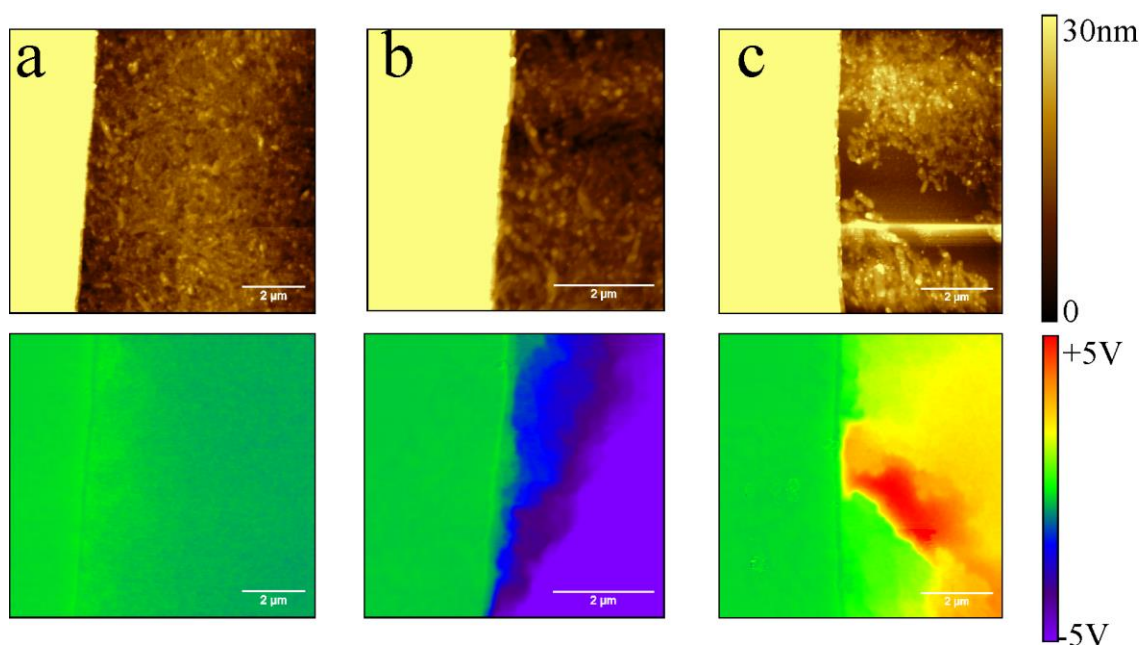


Figure 5.9. KPFM of EH-Indigo crystallite film deposited on bottom-contact field-effect transistors. Height (top) and CPD (bottom) at (a) no bias conditions, (b) 20 minutes after constant -9 V bias applied to the gate, (c) 18 hours after constant -9 V bias applied to gate. For this image the gate bias was turned off and no bias was applied at any electrode.

The gold electrode is grounded and the gold potential does not follow the gate bias as expected. On the other hand, the EH-Indigo film and channel region significantly drops in CPD indicating that the channel region electrically follows the gate and that the EH-Indigo crystallite film is not sufficiently electrically connected to the gold electrode to shield the gate bias. However, one can notice the CPD is not as negative in the EH-Indigo region nearest to the gold electrode indicating that there is indeed some electrical connection between the crystallites closest to the gold. The CPD contrast is most

dramatic upon turning off the gate bias after 18 hours of constant application. Figure 5.9c shows the electrode-channel interface with no bias applied immediately after turning off the gate bias. The exposed silicon oxide region is heavily doped from the bias voltage but more interestingly the EH-Indigo film shows region with the same CPD as the gold electrode. After 18 hours, charge had enough time to percolate between the gold and EH-Indigo and electrically align EH-Indigo crystallites to the source electrode while the bare substrate continued to charge. The long period of time for charging to occur is expected as EH-Indigo is expected to have a low charge mobility values matching that of indigo itself ($\sim 0.01 \text{ cm}^2\text{V}^{-1}\text{s}^{-1}$).¹⁷⁶ The initial measurement in Figure 5.9b reflects the low mobility as there is not sufficient time for charge to move between the gold electrode and EH-Indigo crystallites far into the channel region but Figure 5.9c shows electrical connection does exist in principle. While KPFM is suitable to probe electrical connection between neighboring EH-Indigo crystallites, a more direct measure of conductivity is to perform CAFM.

Conductive atomic force microscopy measurements of EH-Indigo crystallite films on bottom-contact gold FETs reveal the necessity for flatter electrode geometries. Figure 5.10 shows a CAFM experiment performed with an EH-Indigo crystallite film using the same sample as measured by KPFM previously (Figure 5.9). The gold electrodes are top-down fabricated and the height difference between EH-Indigo on top of the electrode and in the channel region can be understood by comparing Figure 5.10a to Figure 5.10b. There is a large step height between the gold and the oxide which most likely means none of the crystallites directly on the electrode are ever in contact with those in the channel region.

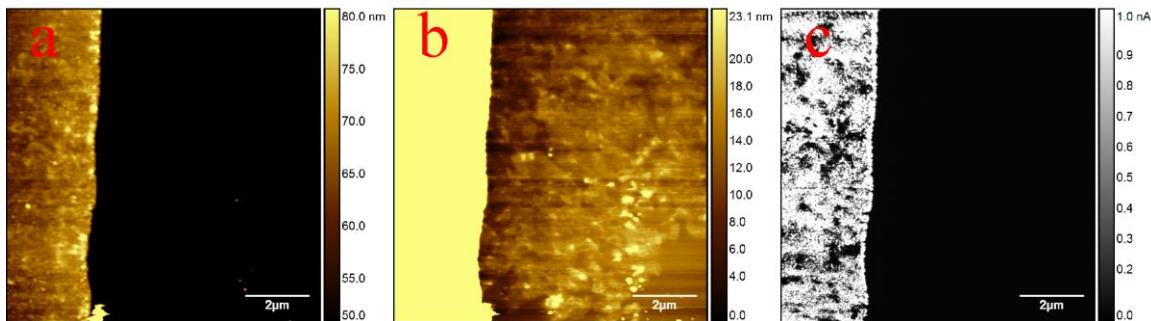


Figure 5.10. CAFM of EH-Indigo crystallite film. (a) Height image scaled to show the 50 nm gold electrode. (b) Height image scaled to show the thin film of EH-Indigo crystallites. (c) Current image measured with a +5 V bias applied to the gold electrode.

As Figure 5.10c shows, no current is measured in the channel region. The only current that is measured is when the tip is in direct contact with the gold electrode itself indicating a loss in electrical contact at the electrode interface. Furthermore, the CAFM measurement shows that the vertical conductivity in the EH-Indigo crystallites is low to none as the dark regions on the electrode correlate with areas of crystallites in Figure 5.10a. This indicates that the charge transport in the (001) direction of EH-Indigo is not favorable which is consistent with the lack of π - π interactions in this axis compared to the more favorable (100) direction. In the (001) direction the charge would have to tunnel through insulating hydrocarbons to transport charge. If current could be transported

laterally across the crystallite the conductivity would be more favorable. Such a measurement requires a flat geometry for the metal contacts into the channel.

5.3.3 Graphene field-effect transistors

The ease of fabricating graphene field-effect transistors allows for important optoelectronic studies of thin systems without sacrificing the structural integrity of the film. The fabrication process of single layer graphene on silicon into a patterned electrode geometry is shown in Figure 5.11. Graphene deposited on silicon oxide and highly doped silicon is covered with photoresist. A bright field mask is necessary for the use of a positive photoresist. Oxygen plasma is the crucial step to etch graphene and care must be taken to optimize the exact dosage. A too powerful of an oxygen plasma for too long will etch the photoresist and the graphene underneath so a 50W 15 second etch is empirically determined to be ideal. A weaker etch will not sufficiently etch the graphene and leave a larger amount of graphitic carbon aggregates in the channel regions. Further washing of the electrodes in acetone and hydrochloric acid helps remove residual photoresist and etching graphene products without disrupting the un-etched graphene. This process can be achieved in less than 30 minutes from start to finish and is very reproducible leading it to be a highly advantageous process for device fabrication on a large scale.

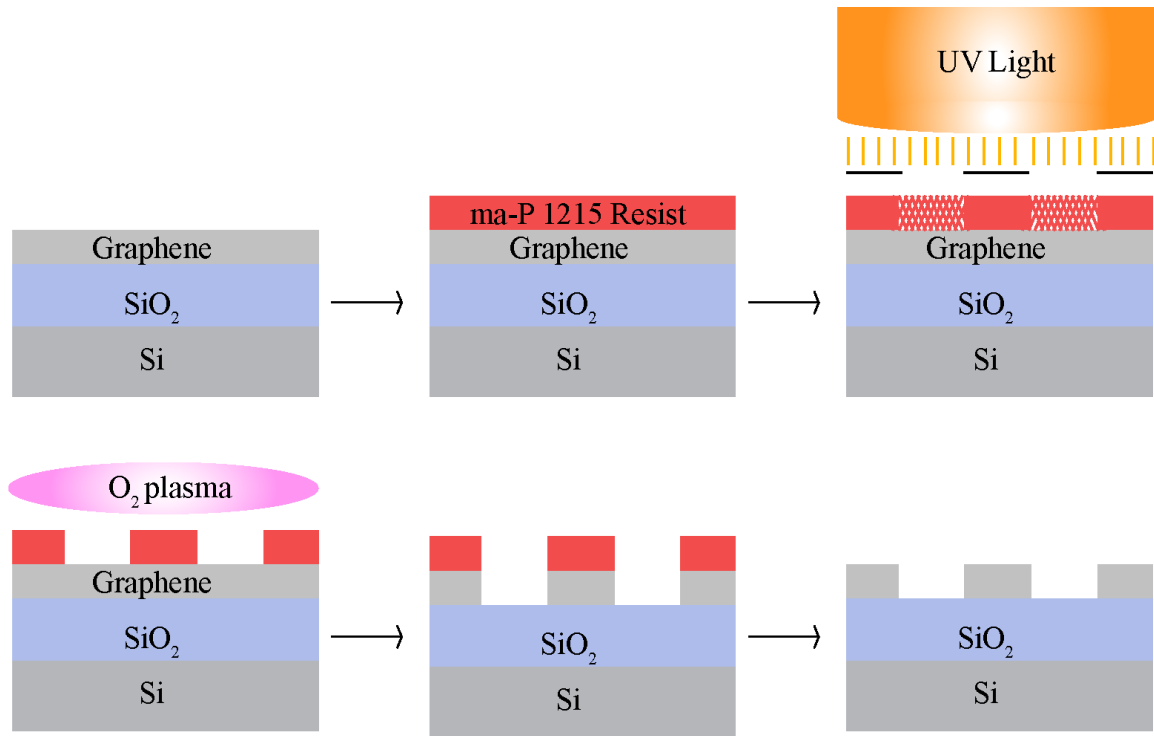


Figure 5.11. Graphene field-effect transistor fabrication process. The photoresist is deposited on the graphene before patterning by UV light and development. Oxygen plasma etches the exposed graphene leaving only the electrode features. Acetone and hydrochloric acid cleans the graphene electrodes and channel regions of silicon oxide.

The graphene FETs are shown in Figure 5.12. The specific pattern seen has large pads for macroscopic wire contact (outside of the image in Figure 5.12a and visible in

Figure 5.12c) that taper to small electrodes with a circular contact region (Figure 5.12b). A significant factor for successful graphene optoelectronic devices is suitable electrical contacts to the graphene itself for voltage biasing or current collection. Many forms of metal plating have been shown to be successful and the contact resistivity can be as low as $\sim 700 \Omega\mu\text{m}$.¹⁷⁷⁻¹⁸⁰ However, metal deposition on pre-patterned graphene electrodes is not trivial and care must be performed to not further damage the graphene structures during subsequent photolithography to achieve patterned metal electrodes. In addition, this additional step slows down the overall fabrication. Also, other mask geometries are possible and the mask used here is only due to availability and its small electrode features. Preliminary work was performed with negative photoresist and dark field masks however negative photoresist (ma-N 400 class) interacts more strongly with graphene than positive resist and the development/removal steps often times removed the underlying graphene significantly or completely. Further optimization of negative photoresists should yield suitability for graphene fabrication.

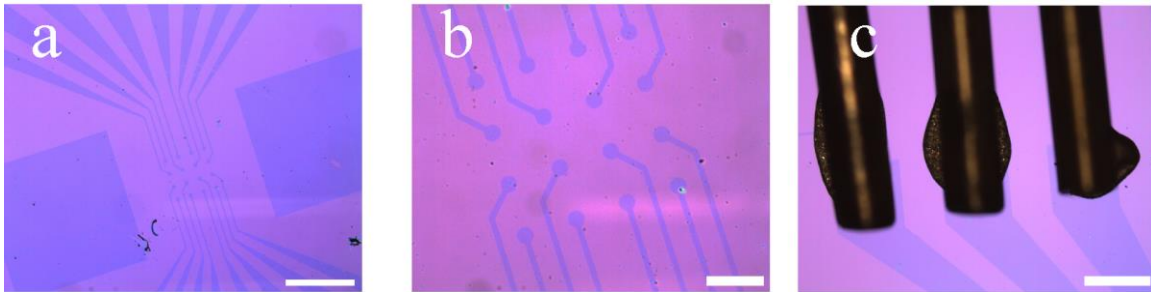


Figure 5.12. Graphene field-effect transistors. (a) Scale bar is 500 microns. (b) Electrode contacts. Scale bar is 100 microns. (c) Stainless steel tubes with copper wire silver pasted on to graphene pads. Scale bar is 500 microns.

AFM reveals the nanoscale morphology of graphene after photolithography patterning. Figure 5.13a shows an AFM height image of a circular graphene electrode after acetone treatment to remove the photoresist. The surface of graphene is fairly pristine and does not contain significant amounts of photoresist residue. The step height between graphene and the oxide is shown in Figure 5.13b for the line profile drawn in Figure 5.13a. The height difference is approximately 1nm. However, the channel region (silicon oxide) is full of particles which are most likely due to the etching of graphene in that region. The graphene that is etched by oxygen plasma is not fully converted to gaseous species and more stable graphitic carbon aggregates remain adhered to the silicon oxide. Hydrochloric acid can be used to remove these residues. Figure 5.13c shows the graphene-silicon oxide interface after 30 minutes of soaking the substrate in 1M hydrochloric acid. The silicon oxide region shows noticeably less amounts of particles. Furthermore, the presence of patches on the graphene seen by a difference in height in Figure 5.13c could indicate further etching by the hydrochloric acid of leftover polymer on graphene. This polymer could be from the chemical vapor deposition process during the graphene growth or it could be from the photoresist during the photolithography. To achieve better electrical contact it is necessary to remove this additional carbon layer as much as possible.

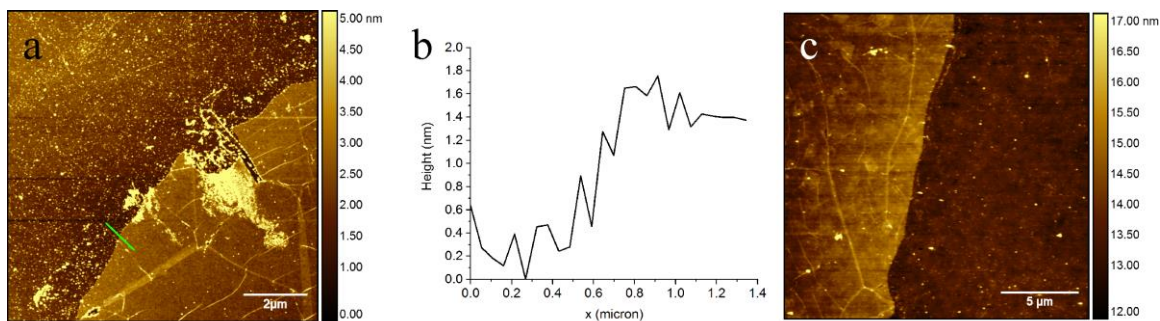


Figure 5.13. AFM characterization of graphene after electrode fabrication. (a) Height image of graphene on silicon oxide. (b) Height profile of green line in (a) which shows the step height of graphene is approximately 1 nm. (c) Height image of graphene after 30 minute soak in 1 M hydrochloric acid.

The fabrication process of the electrode results in a continuous monolayer graphene layer that can be electrically contacted to a voltage source for biasing. Figure 5.14a shows an AFM height image of a kink in the electrode pattern that can also be seen in figure 5.12a. When the fabrication process is successful there is a continuous single layer of graphene from the wire contact pad to the circular electrode feature at the center of the substrate. Placing an electrical bias through the wire to the graphene pad should result in a uniform potential across the entire graphene electrode. This is indeed observed in pristine graphene¹⁸¹ and one can see a fairly uniform contrast in Figure 5.14c in the bottom half of the graphene. However, one can also see the importance of mechanical stability during the photolithography process as during the fabrication process a crack developed in the graphene near the region where the electrode started to taper (Figure 5.14a and Figure 5.14b).

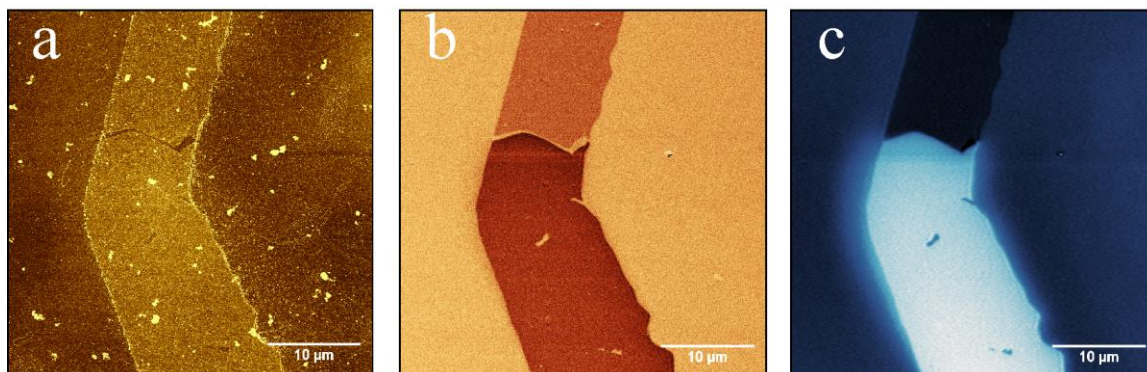


Figure 5.14. KPFM characterization of the graphene electrode. (a) Height image showing a crack in the electrode just above the kink. (b) Phase image showing the distinct crack. (c) CPD image of the electrode. The bottom half of the electrode is still connected to the voltage source and is biased to a higher potential.

The upper portion of the electrode is no longer connected to the lower portion and the underlying silicon oxide substrate in the crack region is now visible. In Figure 5.14c, one can see that the contrast on the upper region (dark) is not the same as the lower portion (bright) which is indicative of different CPD values measured by KPFM. Different CPD

values are the result of the lower half of the electrode still in electrical contact with the voltage source applying a large positive bias. The sharp crack in the height image and phase image is also visible in the CPD image. The slight gradient near the boundaries of the electrode is most likely due to a tip artifact as the measurement is performed in amplitude modulated KPFM and thus the spatial resolution is low indicating the measurement of both graphene and the area around it simultaneously. One would expect a continuous potential across the entire graphene and an abrupt change at the graphene boundary.

Langmuir-Blodgett depositions and electrical characterization by KPFM are used to test the suitability of graphene FETs for further optoelectronic studies of organic thin films. Figure 5.15a shows an AFM height image of an EHT-Indigo film deposited onto fabricated graphene FETs using the Langmuir-Blodgett process. In the lower-left region of the image one can see the graphene electrode with EHT-Indigo film covering most of the electrode. In the rest of the image one can see the particle-full channel region as this substrate was not soaked in hydrochloric acid prior to film deposition. The EHT-Indigo film covers the channel except for a large gap in the middle of the image. There is no evidence that the graphene is mechanically damaged from the Langmuir-Blodgett deposition process of being submerged into water and having a thin film deposited on top. In Figure 5.15b the CPD is measured at no applied bias. The region where graphene is present shows a distinct CPD contrast with a value of approximately -270meV. The EHT-Indigo film directly touching the graphene is higher in CPD compared to that further into the channel region. It appears from the height image that the EHT-Indigo film on the right of the image may not be in contact with the film closest to the graphene electrode. These preliminary findings indicate that the graphene does have an electrical effect on EHT-Indigo when they are in direct contact and that electrical connection between graphene and a few-layer thin organic film can be established.

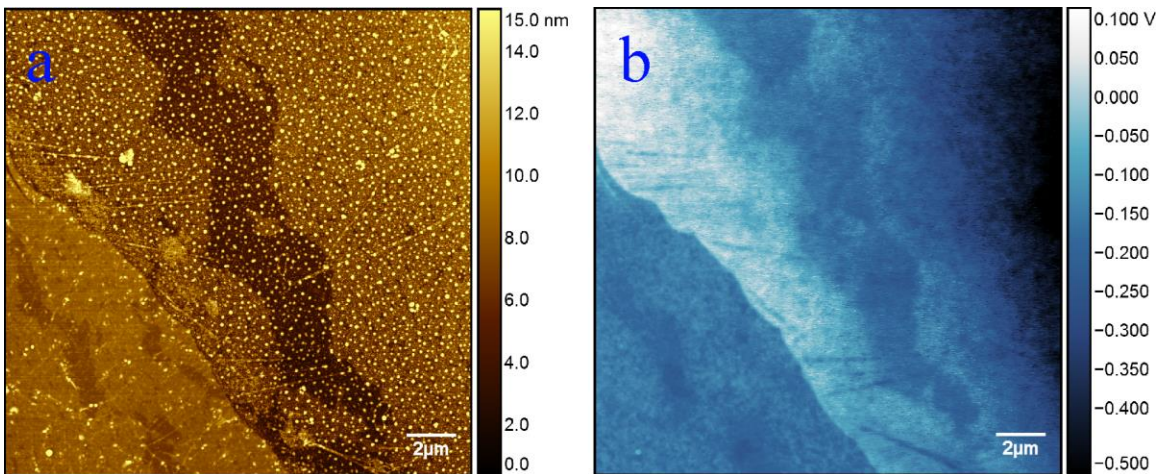


Figure 5.15. KPFM of EHT-Indigo on graphene field-effect transistors. (a) Height image of EHT-Indigo thin film deposited on graphene electrodes. (c) CPD image showing different surface potentials of EHT-Indigo in electrical contact with graphene. No bias is applied to the graphene or the gate.

5.4 Conclusion

EH-Indigo and EHT-Indigo were successfully studied for their optical properties when self-assembled into a solid film. EH-Indigo crystallite films absorb similar to EH-Indigo in solution with only a minor shift to the absorbance peak position. However, the photoluminescence shows a large redshift indicating the presence of optical aggregates. Time-resolved measurements show the lifetime of the crystallites is orders of magnitude lower than that of free EH-Indigo. These findings indicate that EH-Indigo crystallite films contain H-aggregates which also fit the molecular packing of the crystal structure determined in chapter four. Further characterization of the more concentrate pre-compressed EH-Indigo film revealed no optical aggregate formation and photoluminescence similar to single molecule behavior. The photoluminescence of EHT-Indigo showed also a large redshift similar to EH-Indigo however linewidth analysis indicates the extent of packing is not as high as for EH-Indigo which is most likely due to a lesser degree of crystallinity resulting from EHT-Indigo's more isotropic self-assembly. Further studies could be done to elucidate the difference in orientation of emission between EH-Indigo crystallites and EHT-Indigo thin films as their crystal structure and more importantly π - π stacking direction are normal to each other. This could be important for device geometry planning as optimizing the emission orientation could lead to more efficient light emitting diodes.

KPFM studies on the extent of electrical connection in self-assembled indigo films reveal the necessity of better FET devices for organic thin films. KPFM revealed EH-Indigo films contain crystallites that are electrically connected to each other when in physical contact. However the conductivity of such films cannot be probed using conventional bottom-contact FETs with tall source/drain electrodes. Such tall electrodes disrupt the conducting pathway in these films and prevent current from flowing between electrodes across the channel. Graphene FETs is a promising platform that is a suitable alternative to coplanar FETs that are difficult to fabricate. Graphene FETs can be fabricated with ease quickly and reproducibly on a large scale with any pattern desired. The resulting graphene structures are very low in height ($\sim 1\text{nm}$) and more importantly behave the same as monolayer graphene electrically. The use of flat graphene FETs is exciting for use in flexible electronics as the thickness of the device can be reduced substantially.

6 Summary and Outlook

Abstract

This chapter summarizes the research and important findings in this work. Conclusions are made relating the findings to a generalized understanding about the principles that govern structure and electronic properties in organic semiconductor films. Follow up experiments are proposed and future directions are discussed

6.1 Summary

This research has focused on the nanoscale investigation of fundamental physical chemistry principles governing structural and electronic properties in low-dimensional organic semiconductor systems. Two different groups of semiconducting oligomers were studied for their ability to form self-assembled monolayer or few-layer systems and further characterized for their optical and electronic properties.

The first class of organic semiconductors studied was oligothiophenes. The quaterthiophene hydroxyl derivative HD4TBA self-assembled into crystalline islands showing similar behavior to the methyl pentathiophene oligomer D5TBA. The LB experiments confirmed that thiophenes are the dominant driving force of oligothiophene self-assembly at the air-water interface and that the presence of two hydrophilic groups at the end of the molecule does not disrupt the formation of crystalline islands. However, the reduction by one thiophene group and the presence of a hydroxyl termination group does introduce important differences compared to the methyl pentathiophene. HD4TBA yielded fewer and smaller-sized islands due to predicted weaker intermolecular thiophene interactions as well as exhibiting a larger hydrocarbon chain tilt making the HD4TBA monolayer self-assemble into a less standing-straight geometry compared to D5TBA. By measuring the extent of attraction between the AFM tip and the surface of the monolayer, AFM confirmed the surface termination is more hydrophilic for the HD4TBA monolayer than for D5TBA. Furthermore, mixed monolayer films were successfully made on the water surface and transferred to silicon substrates. Further studies in the friction properties of the mixed films would reveal the extent of hydrophilicity at the surface of each film and help explain how one oligothiophene is possible to grow on another. Also, the process of solution deposition can be varied to deposit a mixed solution with both molecules dissolved in one chloroform solution. It would be interesting to observe possible intercalation of one oligothiophene into the crystal of a second oligothiophene to get truly mixed monolayers with unique properties.

The functionalization of HD4TBA resulted in a sensitivity of the electronic properties to the presence of water vapor. In-situ KPFM demonstrated that the surface potential of HD4TBA changes when the relative humidity is varied. There is a net increase of approximately +100 meV to the contact potential difference when the humidity is increased from ~3% to 45%. Furthermore, KPFM showed that for a mixed HD4TBA/D5TBA film the HD4TBA surface potential changes but the D5TBA does not. The hydroxyl group can undergo hydrogen bonding with the water molecules whereas the methyl group is completely inert at these low to moderate humidity values. Finally APXPS showed that compared to ultra-high vacuum conditions, low humidity does not show any significant changes to the binding energy of sulfur in the thiophene groups of a thiol oligothiophene SAM (TD4TBA). The water vapor only has an effect on the hydrophilic carboxylic group that is at the surface of the monolayer indicating again the presence of hydrogen bonding between water and the hydrophilic terminal group of an oligothiophene. These findings are important considerations in further oligothiophene and organic semiconductor material design for sensors and photovoltaic applications as humidity is one of the most common causes of degradation for organic electronic.

Indigo semiconducting small molecules were then studied for their self-assembly properties. Similar to oligothiophenes, EH-Indigo self-assembles into crystalline structures that are approximately micron sized at the air-water interface. However, unlike the isotropic crystals that oligothiophenes form, EH-Indigo self-assembles into anisotropic crystallites. The crystallites have a distinct rectangular shape and can range from a single layer to a few layers at a time per crystallite. Friction AFM imaging reveals that the surface termination of the crystallite is hydrophobic whereas the edges are more hydrophilic indicating that the self-assembly at the air-water interface is not driven by an amphiphilic geometry as a hydrophobic top of the film would imply a hydrophobic bottom of the film due to the molecule's symmetry. GIWAXS revealed that the packing geometry contains two distinct intermolecular interactions in the lateral plane of the crystallite. The (100) axis contains the π - π interaction between indigo groups in a face-to-face geometry. This axis is also the long-axis of the crystallite. The short-axis of the crystallite is the (010) axis and is the result of hydrogen bonding between neighboring EH-Indigo molecules. The aspect ratio indicates that the (100) π -stacking interaction is ~4.5 times more favorable to grow compared to the (010) hydrogen bonding direction. Interestingly, the (001) axis is very uniform and has almost perfect alignment of molecular layers. However, an increase in EH-Indigo concentration during the solution deposition step does not result in larger crystallite sizes but rather a new morphology. This morphology by AFM does not show the same anisotropy but rather very uniform and thick film growth instead. Furthermore to contrast the EH-Indigo self-assembly to that of the oligothiophene examples, EH-Indigo crystallites on the water surface can go through a further phase transition during the LB compression if high surface pressures are reached. Whereas in the case of oligothiophenes where crystal islands simply collapse and form isolated bilayer structures, EH-Indigo crystallites forms long-range bundles of crystallites on the water surface that can also be transferred to a substrate. These bundles can be very large (>1cm) and hint at favorable inter-crystallite interactions. Further measurements on these bundles in the form of small-angle x-ray scattering or polarization dependent optical spectroscopy should reveal the extent of orientation and aggregation in these bundles. An ideal scenario is perfectly oriented crystallites in each bundle. If such a bundle is possible with more conductive indigo molecules then rather than use a single crystal for an active layer for conducting materials, one could utilize conductive bundles which could be deposited on substrates with precise orientation control.

The anisotropy of EH-Indigo self-assembly at the air-water interface is contrasted with the isotropy of EHT-Indigo. EHT-Indigo only differs by the addition of two thiophenes to the molecular structure but the self-assembly behavior change is significant. The most important change is that the orientation of the molecule at the air-water interface is perpendicular to that of EH-Indigo at the air-water interface. Preliminary measurements by AFM and GIWAXS indicate that EHT-Indigo has the molecule lying flat on the water whereas for the EH-Indigo case the molecule is closer to perpendicular to the water. Furthermore, EHT-Indigo crystal islands are more round and isotropic than EH-Indigo which is explained by GIWAXS measurements showing no heterogeneity in the intermolecular interactions in the lateral plane of the film. The π -stacking direction seems to be parallel to the water surface and the lateral plane of the film is of isotropic hydrogen bonding interactions. Interestingly if a LB deposition is attempted with EH-Indigo the film does not transfer to substrates such as HOPG or highly doped silicon with

only a native oxide. The opposite is true for EHT-Indigo and very uniform coverage is achieved with EHT-Indigo deposition onto HOPG. Further experiments and theoretical calculations to determine the exact electrical crystal dipole orientation would help understand the extent of electrostatic interaction between the surface and the crystal dipoles.

The optical properties of EH-Indigo and EHT-Indigo crystals were investigated by photoluminescence spectroscopy. EH-Indigo and EHT-Indigo were both found to exhibit a large photoluminescence redshift when self-assembled into a crystal compared to single-molecule behavior in solution. The redshift for EH-Indigo was found to be ~ 320 meV and for EHT-Indigo ~ 296 meV. Furthermore, time-resolved photoluminescence spectroscopy determined the fluorescence lifetime of EH-Indigo crystallites is comparable to 50 picoseconds which is orders of magnitude faster than the solution lifetime of 1.26 nanoseconds. These findings indicate that EH-Indigo and EHT-Indigo are H-aggregate dyes which coincides well with the crystal structure determined by GIWAXS. Optical aggregation behavior was not observed in the concentrated EH-Indigo film as the photoluminescence behavior matches well with that observed for the solution. Further photoluminescence measurements on the EH-Indigo bundles would show how well the macroscopic assemblies aggregated and whether they are suitable for further electrical and optical studies with the purpose of ultimately using them in devices.

Lastly the electronic properties of EH-Indigo and EHT-Indigo films were investigated by CAFM and KPFM, in the process also demonstrating the need for a more suitable platform to study thin organic electronics by the way of graphene field-effect transistors. EH-Indigo crystallite films were shown to exhibit inter-crystallite electrical contact by KPFM. When applied with a gate voltage, the EH-Indigo crystallite film is able to stay electrically grounded to the source/drain electrodes albeit not very efficiently due to EH-Indigo's low conductivity. The inability to conduct current in the bottom-contact gold FET geometry however is due to the scale of the electrode compared to the height of crystallites. To mediate such thin organic semiconducting films, graphene field-effect transistors are fabricated using common nanofabrication techniques. Monolayer graphene deposited on thick silicon oxide to behave as source and drain electrodes and the highly doped silicon which acts as a gate electrode. The graphene after patterning shows only a small step height that will not disrupt the conducting of current across monolayer films. Preliminary measurements with EHT-Indigo and graphene FETs indicate that there is electrical contact between the graphene and EHT-Indigo.

6.2 Future Directions

The in-situ characterization of functional organic semiconducting monolayers is an important field that deserves attention. An AFM chamber that can reliably change the environment during scanning probe measurements is a necessity for research labs investigating the next generation of organic molecules for electronic applications. It is not enough to measure the performance of semiconductors in vacuum or dry conditions if one wants to understand true device performance. One of the fundamental issues holding

organic electronics back is the degradation of organic material quicker than their inorganic counterparts and in-situ AFM can provide answers as to how to better design materials that can withstand these changing environmental effects. Alternative, these in-situ AFM techniques also help understand how to design better organic film sensors.

The advent of flat field-effect transistors for the study of thin organic films is also very promising for fundamental structure-property investigations. Monolayer organic films can now be better studied for their electronic properties in a transistor geometry without the worry of disrupting the molecular orbital overlap between neighboring molecules. With a step height less than one nanometer, graphene field-effect transistors can be used with oligothiophenes, indigo small molecules and others to measure the properties in low-dimensional systems. The field of molecular electronics will make a significant leap when it is possible to identify a specific class of molecules with high performance in a model system and then form a crystalline film with a specific geometry and orientation that can be deposited into a device architecture that is predetermined.

References

1. Eley, D., Phthalocyanines as semiconductors. *Nature* **1948**, 162 (4125), 819-819.
2. Kallmann, H.; Pope, M., Positive Hole Injection into Organic Crystals. *The Journal of Chemical Physics* **1960**, 32 (1), 300-301.
3. O'Regan, B.; Grätzel, M., A low-cost, high-efficiency solar cell based on dye-sensitized colloidal TiO₂ films. *Nature* **1991**, 353 (6346), 737-740.
4. Hagfeldt, A.; Grätzel, M., Molecular Photovoltaics. *Accounts of Chemical Research* **2000**, 33 (5), 269-277.
5. Schmidt-Mende, L.; Fechtenkötter, A.; Müllen, K.; Moons, E.; Friend, R. H.; MacKenzie, J. D., Self-Organized Discotic Liquid Crystals for High-Efficiency Organic Photovoltaics. *Science* **2001**, 293 (5532), 1119-1122.
6. Nunzi, J.-M., Organic photovoltaic materials and devices. *Comptes Rendus Physique* **2002**, 3 (4), 523-542.
7. Dodabalapur, A., Organic light emitting diodes. *Solid State Communications* **1997**, 102 (2), 259-267.
8. Sekitani, T.; Nakajima, H.; Maeda, H.; Fukushima, T.; Aida, T.; Hata, K.; Someya, T., Stretchable active-matrix organic light-emitting diode display using printable elastic conductors. *Nat Mater* **2009**, 8 (6), 494-499.
9. Reineke, S.; Lindner, F.; Schwartz, G.; Seidler, N.; Walzer, K.; Lussem, B.; Leo, K., White organic light-emitting diodes with fluorescent tube efficiency. *Nature* **2009**, 459 (7244), 234-238.
10. This plot is courtesy of the National Renewable Energy Laboratory, Golden, CO.
11. Bao, Z.; Feng, Y.; Dodabalapur, A.; Raju, V.; Lovinger, A. J., High-performance plastic transistors fabricated by printing techniques. *Chemistry of Materials* **1997**, 9 (6), 1299-1301.
12. Briseno, A. L.; Mannsfeld, S. C.; Ling, M. M.; Liu, S.; Tseng, R. J.; Reese, C.; Roberts, M. E.; Yang, Y.; Wudl, F.; Bao, Z., Patterning organic single-crystal transistor arrays. *Nature* **2006**, 444 (7121), 913-917.
13. Sze, S. M.; Ng, K. K., *Physics of semiconductor devices*. John Wiley & sons: 2006.
14. Brédas, J. L.; Calbert, J. P.; da Silva Filho, D. A.; Cornil, J., Organic semiconductors: A theoretical characterization of the basic parameters governing charge transport. *Proceedings of the National Academy of Sciences* **2002**, 99 (9), 5804-5809.
15. Brédas, J.-L.; Beljonne, D.; Coropceanu, V.; Cornil, J., Charge-transfer and energy-transfer processes in pi-conjugated oligomers and polymers: a molecular picture. *Chemical reviews* **2004**, 104, 4971-5004.
16. Brédas, J.-L., Charge transport in organic semiconductors. *Chemical reviews* **2007**, 107, 926-952.
17. Hasegawa, T.; Takeya, J., Organic field-effect transistors using single crystals. *Science and Technology of Advanced Materials* **2009**, 10 (2), 024314.
18. Murphy, A. R.; Frechet, J. M. J., Organic semiconducting oligomers for use in thin film transistors. *Chemical reviews* **2007**, 107 (4), 1066-1096.
19. Bao, Z.; Dodabalapur, A.; Lovinger, A. J., Soluble and processable regioregular poly (3 - hexylthiophene) for thin film field - effect transistor applications with high mobility. *Applied Physics Letters* **1996**, 69 (26), 4108-4110.

20. Chua, L.-l.; Zaumseil, J.; Chang, J.-f.; Ou, E. C.; Ho, P. K.-H.; Sirringhaus, H.; Friend, R. H., General observation of n-type field-effect behaviour in organic semiconductors. *Nature* **2005**, *434*, 194-199.
21. Anthony, J. E.; Facchetti, A.; Heeney, M.; Marder, S. R.; Zhan, X., n-Type Organic Semiconductors in Organic Electronics. *Advanced Materials* **2010**, *22* (34), 3876-3892.
22. Miozzo, L.; Yassar, A.; Horowitz, G., Surface engineering for high performance organic electronic devices: the chemical approach. *Journal of Materials Chemistry* **2010**, *20* (13), 2513-2538.
23. Horowitz, G., Organic field-effect transistors. *Advanced Materials* **1998**, *10* (5), 365-377.
24. Minemawari, H.; Yamada, T.; Matsui, H.; Tsutsumi, J. y.; Haas, S.; Chiba, R.; Kumai, R.; Hasegawa, T., Inkjet printing of single-crystal films. *Nature* **2011**, *475* (7356), 364-367.
25. Diao, Y.; Tee, B. C. K.; Giri, G.; Xu, J.; Kim, D. H.; Becerril, H. A.; Stoltenberg, R. M.; Lee, T. H.; Xue, G.; Mannsfeld, S. C. B.; Bao, Z., Solution coating of large-area organic semiconductor thin films with aligned single-crystalline domains. *Nat Mater* **2013**, *12* (7), 665-671.
26. Crone, B.; Dodabalapur, A.; Gelperin, A.; Torsi, L.; Katz, H. E.; Lovinger, A. J.; Bao, Z., Electronic sensing of vapors with organic transistors. *Applied Physics Letters* **2001**, *78* (15), 2229-2231.
27. Torsi, L.; Lovinger, A.; Crone, B., Correlation between oligothiophene thin film transistor morphology and vapor responses. *The Journal of Physical Chemistry B* **2002**, *12563*-12568.
28. Torsi, L.; Magliulo, M.; Manoli, K.; Palazzo, G., Organic field-effect transistor sensors: a tutorial review. *Chemical Society reviews* **2013**, *42* (22), 8612-8628.
29. Overney, R. M.; Meyer, E.; Frommer, J.; Guentherodt, H. J.; Fujihira, M.; Takano, H.; Gotoh, Y., Force Microscopy Study of Friction and Elastic Compliance of Phase-Separated Organic Thin Films. *Langmuir* **1994**, *10* (4), 1281-1286.
30. Kelley, T. W.; Granstrom, E.; Frisbie, C. D., Conducting Probe Atomic Force Microscopy: A Characterization Tool for Molecular Electronics. *Advanced Materials* **1999**, *11* (3), 261-264.
31. Kelley, T. W.; Frisbie, C. D., Point contact current-voltage measurements on individual organic semiconductor grains by conducting probe atomic force microscopy. *Journal of Vacuum Science & Technology B* **2000**, *18* (2), 632-635.
32. Mativetsky, J. M.; Loo, Y.-L.; Samori, P., Elucidating the nanoscale origins of organic electronic function by conductive atomic force microscopy. *Journal of Materials Chemistry C* **2014**, *2* (17), 3118-3128.
33. Coffey, D. C.; Reid, O. G.; Rodovsky, D. B.; Bartholomew, G. P.; Ginger, D. S., Mapping Local Photocurrents in Polymer/Fullerene Solar Cells with Photoconductive Atomic Force Microscopy. *Nano Letters* **2007**, *7* (3), 738-744.
34. Dang, X.-D.; Tamayo, A. B.; Seo, J.; Hoven, C. V.; Walker, B.; Nguyen, T.-Q., Nanostructure and Optoelectronic Characterization of Small Molecule Bulk Heterojunction Solar Cells by Photoconductive Atomic Force Microscopy. *Advanced Functional Materials* **2010**, *20* (19), 3314-3321.

35. Puntambekar, K. P.; Pesavento, P. V.; Frisbie, C. D., Surface potential profiling and contact resistance measurements on operating pentacene thin-film transistors by Kelvin probe force microscopy. *Applied Physics Letters* **2003**, *83* (26), 5539-5541.
36. Hoppe, H.; Glatzel, T.; Niggemann, M.; Hinsch, A.; Lux-Steiner, M. C.; Sariciftci, N. S., Kelvin Probe Force Microscopy Study on Conjugated Polymer/Fullerene Bulk Heterojunction Organic Solar Cells. *Nano Letters* **2005**, *5* (2), 269-274.
37. Pingree, L. S. C.; Reid, O. G.; Ginger, D. S., Electrical Scanning Probe Microscopy on Active Organic Electronic Devices. *Advanced Materials* **2009**, *21* (1), 19-28.
38. Kelley, T. W.; Frisbie, C. D., Gate Voltage Dependent Resistance of a Single Organic Semiconductor Grain Boundary. *The Journal of Physical Chemistry B* **2001**, *105* (20), 4538-4540.
39. Chwang, A. B.; Frisbie, C. D., Temperature and gate voltage dependent transport across a single organic semiconductor grain boundary. *Journal of Applied Physics* **2001**, *90* (3), 1342-1349.
40. Binnig, G.; Quate, C. F.; Gerber, C., Atomic Force Microscope. *Physical Review Letters* **1986**, *56* (9), 930-933.
41. Jalili, N.; Laxminarayana, K., A review of atomic force microscopy imaging systems: application to molecular metrology and biological sciences. *Mechatronics* **2004**, *14* (8), 907-945.
42. Zhong, Q.; Inniss, D.; Kjoller, K.; Elings, V. B., Fractured polymer/silica fiber surface studied by tapping mode atomic force microscopy. *Surface Science Letters* **1993**, *290* (1), L688-L692.
43. Giessibl, F. J., Atomic resolution of the silicon (111)-(7x7) surface by atomic force microscopy. *Science* **1995**, *267* (5194), 68-71.
44. Gross, L.; Mohn, F.; Moll, N.; Liljeroth, P.; Meyer, G., The Chemical Structure of a Molecule Resolved by Atomic Force Microscopy. *Science* **2009**, *325* (5944), 1110-1114.
45. Gross, L.; Mohn, F.; Moll, N.; Schuler, B.; Criado, A.; Guitian, E.; Pena, D.; Gourdon, A.; Meyer, G., Bond-Order Discrimination by Atomic Force Microscopy. *Science* **2012**, *337*, 1326-1329.
46. Thundat, T.; Zheng, X. Y.; Chen, G. Y.; Warmack, R. J., Role of relative humidity in atomic force microscopy imaging. *Surface Science* **1993**, *294* (1), L939-L943.
47. Sugimura, H.; Ishida, Y.; Hayashi, K.; Takai, O.; Nakagiri, N., Potential shielding by the surface water layer in Kelvin probe force microscopy. *Applied Physics Letters* **2002**, *80* (8), 1459-1461.
48. Martin, F.; Hendriksen, B. L. M.; Katan, A. J.; Qi, Y.; Mauldin, C.; Fréchet, J. M. J.; Salmeron, M., Sensitivity to Molecular Order of the Electrical Conductivity in Oligothiophene Monolayer Films. *Langmuir* **2013**, *29* (4), 1206-1210.
49. Nonnenmacher, M., Kelvin probe force microscopy. *Applied Physics Letters* **1991**, *598*, 2921-2923.
50. Melitz, W.; Shen, J.; Kummel, A. C.; Lee, S., Kelvin probe force microscopy and its application. *Surface Science Reports* **2011**, *66*, 1-27.
51. Mohn, F.; Gross, L.; Moll, N.; Meyer, G., Imaging the charge distribution within a single molecule. *Nat Nano* **2012**, *7* (4), 227-231.

52. Beerbom, M. M.; Lägél, B.; Cascio, A. J.; Doran, B. V.; Schlaf, R., Direct comparison of photoemission spectroscopy and in situ Kelvin probe work function measurements on indium tin oxide films. *Journal of Electron Spectroscopy and Related Phenomena* **2006**, *152* (1–2), 12-17.
53. Siegbahn, K., Electron spectroscopy for atoms, molecules, and condensed matter. *Reviews of Modern Physics* **1982**, *54* (3), 709-728.
54. Ogletree, D. F.; Bluhm, H.; Lebedev, G.; Fadley, C. S.; Hussain, Z.; Salmeron, M., A differentially pumped electrostatic lens system for photoemission studies in the millibar range. *Review of Scientific Instruments* **2002**, *73* (11), 3872-3877.
55. Salmeron, M.; Schlögl, R., Ambient pressure photoelectron spectroscopy: A new tool for surface science and nanotechnology. *Surface Science Reports* **2008**, *63* (4), 169-199.
56. Starr, D. E.; Liu, Z.; Havecker, M.; Knop-Gericke, A.; Bluhm, H., Investigation of solid/vapor interfaces using ambient pressure X-ray photoelectron spectroscopy. *Chemical Society reviews* **2013**, *42* (13), 5833-5857.
57. Ketteler, G.; Ashby, P.; Mun, B. S.; Ratera, I.; Bluhm, H.; Kasemo, B.; Salmeron, M., In situ photoelectron spectroscopy study of water adsorption on model biomaterial surfaces. *Journal of Physics: Condensed Matter* **2008**, *184024*, 184024.
58. Hexemer, A.; Müller-Buschbaum, P., Advanced grazing-incidence techniques for modern soft-matter materials analysis. *IUCrJ* **2015**, *2* (Pt 1), 106-125.
59. Lakowicz, J. R., *Principles of fluorescence spectroscopy*. Springer Science & Business Media: 2013.
60. Brenner, T. J. K.; McNeill, C. R., Spatially Resolved Spectroscopic Mapping of Photocurrent and Photoluminescence in Polymer Blend Photovoltaic Devices. *The Journal of Physical Chemistry C* **2011**, *115* (39), 19364-19370.
61. Honmou, Y.; Hirata, S.; Komiyama, H.; Hiyoshi, J.; Kawauchi, S.; Iyoda, T.; Vacha, M., Single-molecule electroluminescence and photoluminescence of polyfluorene unveils the photophysics behind the green emission band. *Nature Communications* **2014**, *5*.
62. Petty, M. C., *Langmuir-Blodgett films: an introduction*. Cambridge University Press: 1996.
63. Roberts, G. G.; Vincett, P. S.; Barlow, W. A., Technological applications of Langmuir-Blodgett films. *Physics in Technology* **1981**, *12* (2), 69.
64. Zasadzinski, J.; Viswanathan, R.; Madsen, L.; Garnæs, J.; Schwartz, D., Langmuir-Blodgett films. *Science* **1994**, *263* (5154), 1726-1733.
65. Schwartz, D. K., Langmuir-Blodgett film structure. *Surface Science Reports* **1997**, *27* (7), 245-334.
66. Kobayashi, M.; Chen, J.; Chung, T. C.; Moraes, F.; Heeger, A. J.; Wudl, F., Synthesis and properties of chemically coupled poly(thiophene). *Synthetic Metals* **1984**, *9* (1), 77-86.
67. Sato, M.; Tanaka, S.; Kaeriyama, K., SOLUBLE CONDUCTING POLYTHIOPHENES. *J. Chem. Soc.-Chem. Commun.* **1986**, (11), 873-874.
68. McCullough, R. D., The chemistry of conducting polythiophenes. *Advanced Materials* **1998**, *10* (2), 93-+.

69. Ong, B. S.; Wu, Y. L.; Liu, P.; Gardner, S., High-performance semiconducting polythiophenes for organic thin-film transistors. *Journal of the American Chemical Society* **2004**, *126* (11), 3378-3379.
70. Zhang, F.; Wu, D.; Xu, Y.; Feng, X., Thiophene-based conjugated oligomers for organic solar cells. *Journal of Materials Chemistry* **2011**, *21* (44), 17590-17600.
71. Lin, Y.; Li, Y.; Zhan, X., Small molecule semiconductors for high-efficiency organic photovoltaics. *Chemical Society reviews* **2012**, *41* (11), 4245-4272.
72. Garnier, F.; Yassar, A.; Hajlaoui, R.; Horowitz, G.; Deloffre, F.; Servet, B.; Ries, S.; Alnot, P., Molecular engineering of organic semiconductors: design of self-assembly properties in conjugated thiophene oligomers. *Journal of the American Chemical Society* **1993**, *115* (19), 8716-8721.
73. Fichou, D., Structural order in conjugated oligothiophenes and its implications on opto-electronic devices. *Journal of Materials Chemistry* **2000**, *10* (3), 571-588.
74. Mishra, A.; Ma, C.-Q.; Bäuerle, P., Functional Oligothiophenes: Molecular Design for Multidimensional Nanoarchitectures and Their Applications. *Chemical reviews* **2009**, *109* (3), 1141-1276.
75. Akimichi, H.; Waragai, K.; Hotta, S.; Kano, H.; Sakaki, H., Field - effect transistors using alkyl substituted oligothiophenes. *Applied Physics Letters* **1991**, *58* (14), 1500-1502.
76. Horowitz, G.; Hajlaoui, M. E.; Hajlaoui, R., Temperature and gate voltage dependence of hole mobility in polycrystalline oligothiophene thin film transistors. *Journal of Applied Physics* **2000**, *87*, 4456-4463.
77. Halik, B. M.; Klauk, H.; Zschieschang, U.; Schmid, G.; Ponomarenko, S.; Kirchmeyer, S.; Weber, W., Relationship Between Molecular Structure and Electrical Performance of Oligothiophene Organic Thin Film Transistors. *Advanced Materials* **2003**, *15*, 917-922.
78. Afsharimani, N.; Nysten, B., Electronic properties of dioctylterthiophene-based organic thin-film transistors: A Kelvin probe force microscopy study. *Thin Solid Films* **2013**, *536*, 295-301.
79. Rahman, M.; Kumar, P.; Park, D.-S.; Shim, Y.-B., Electrochemical Sensors Based on Organic Conjugated Polymers. *Sensors* **2008**, *8* (1), 118.
80. Schmelzer, M.; Burghard, M.; Bäuerle, P.; Roth, S., Structural information on thiophene Langmuir-Blodgett heterostructures. *Thin Solid Films* **1994**, *243* (1), 620-624.
81. Belobrzeczkaja, L.; Bajo, G.; Bolognesi, A.; Catellani, M., Thin films of poly-3-(oxaalkyl)thiophenes by Langmuir-Blodgett technique. *Synthetic Metals* **1997**, *84* (1), 195-196.
82. Cirák, J.; Toměčík, P.; Červeň, I.; Čík, G.; Végh, D., X-ray studies on Langmuir-Blodgett films of novel amphiphilic oligothiophenes. *Supramolecular Science* **1997**, *4* (3), 539-542.
83. Isz, S.; Weissbuch, I.; Kjaer, K.; Bouwman, W. G.; Als-Nielsen, J.; Palacin, S.; Raudel-Teixier, A.; Leiserowitz, L.; Lahav, M., Crystalline Mono- and Multilayer Self-Assemblies of Oligothiophenes at the Air-Water Interface. *Chemistry – A European Journal* **1997**, *3* (6), 930-939.
84. Tsuzuki, S.; Honda, K.; Azumi, R., Model Chemistry Calculations of Thiophene Dimer Interactions: Origin of π -Stacking. *Journal of the American Chemical Society* **2002**, *124* (41), 12200-12209.

85. Scherlis, D. a.; Marzari, N., pi-Stacking in thiophene oligomers as the driving force for electroactive materials and devices. *Journal of the American Chemical Society* **2005**, *127*, 3207-12.
86. Chen, J.; Murphy, A. R.; Esteve, J.; Ogletree, D. F.; Salmeron, M.; Fréchet, J. M. J., Preparation and nanoscale mechanical properties of self-assembled carboxylic acid functionalized pentathiophene on mica. *Langmuir* **2004**, *20*, 7703-10.
87. Hendriksen, B. L. M.; Martin, F.; Qi, Y.; Mauldin, C.; Vukmirovic, N.; Ren, J.; Wormeester, H.; Katan, A. J.; Altoe, V.; Aloni, S.; Fréchet, J. M. J.; Wang, L.-W.; Salmeron, M., Electrical Transport Properties of Oligothiophene-Based Molecular Films Studied by Current Sensing Atomic Force Microscopy. *Nano Letters* **2011**, *11*, 4107-4112.
88. Altoe, V.; Martin, F.; Katan, A. J.; Salmeron, M.; Aloni, S., Electron microscopy reveals structure and morphology of one molecule thin organic films. *Nano Letters* **2012**, *12*, 1295-9.
89. Yin, N.-N.; Buyanin, A.; Riechers, S. L.; Lee, O. P.; Fréchet, J. M. J.; Salmeron, M.; Liu, G.-y., In Situ and Real-Time Atomic Force Microscopy Studies of the Stability of Oligothiophene Langmuir–Blodgett Monolayers in Liquid. *The Journal of Physical Chemistry C* **2014**, *118* (11), 5789-5795.
90. Grass, M. E.; Karlsson, P. G.; Aksoy, F.; Lundqvist, M.; Wannberg, B.; Mun, B. S.; Hussain, Z.; Liu, Z., New ambient pressure photoemission endstation at Advanced Light Source beamline 9.3.2. *Review of Scientific Instruments* **2010**, *81* (5), 053106.
91. Martin, F.; Hendriksen, B. L. M.; Katan, A. J.; Qi, Y.; Mauldin, C.; Fréchet, J. M. J.; Salmeron, M., Sensitivity to molecular order of the electrical conductivity in oligothiophene monolayer films. *Langmuir* **2013**, *29*, 1206-10.
92. Ewbank, P. C.; Stefan, M. C.; Sauvé, G.; McCullough, R. D., Synthesis, Characterization and Properties of Regioregular Polythiophene-Based Materials. In *Handbook of Thiophene-Based Materials*, John Wiley & Sons, Ltd: 2009; pp 157-217.
93. Curtis, M. D.; Cao, J.; Kampf, J. W., Solid-State Packing of Conjugated Oligomers: From π -Stacks to the Herringbone Structure. *Journal of the American Chemical Society* **2004**, *126* (13), 4318-4328.
94. Ramin, L.; Jabbarzadeh, A., Odd–Even Effects on the Structure, Stability, and Phase Transition of Alkanethiol Self-Assembled Monolayers. *Langmuir* **2011**, *27* (16), 9748-9759.
95. Hinterwirth, H.; Kappel, S.; Waitz, T.; Prohaska, T.; Lindner, W.; Lämmerhofer, M., Quantifying Thiol Ligand Density of Self-Assembled Monolayers on Gold Nanoparticles by Inductively Coupled Plasma–Mass Spectrometry. *ACS Nano* **2013**, *7* (2), 1129-1136.
96. García, R.; Pérez, R., Dynamic atomic force microscopy methods. *Surface Science Reports* **2002**, *47* (6–8), 197-301.
97. Alemán, C.; Armelin, E.; Iribarren, J. I.; Liesa, F.; Laso, M.; Casanovas, J., Structural and electronic properties of 3,4-ethylenedioxythiophene, 3,4-ethylenedisulfanylfurane and thiophene oligomers: A theoretical investigation. *Synthetic Metals* **2005**, *149* (2–3), 151-156.
98. Bouzzine, S. M.; Bouzakraoui, S.; Bouachrine, M.; Hamidi, M., Density functional theory (B3LYP/6-31G*) study of oligothiophenes in their aromatic and polaronic states. *Journal of Molecular Structure: THEOCHEM* **2005**, *726* (1–3), 271-276.

99. Sirringhaus, H., Device Physics of Solution-Processed Organic Field-Effect Transistors. *Advanced Materials* **2005**, *17*, 2411-2425.
100. Kaake, L. G.; Barbara, P. F.; Zhu, X.-Y., Intrinsic Charge Trapping in Organic and Polymeric Semiconductors: A Physical Chemistry Perspective. *The Journal of Physical Chemistry Letters* **2010**, *1*, 628-635.
101. Hallam, T.; Lee, M.; Zhao, N.; Nandhakumar, I.; Kemerink, M.; Heeney, M.; McCulloch, I.; Sirringhaus, H., Local Charge Trapping in Conjugated Polymers Resolved by Scanning Kelvin Probe Microscopy. *Physical Review Letters* **2009**, *103* (25), 256803.
102. Palermo, V.; Palma, M.; Samorì, P., Electronic Characterization of Organic Thin Films by Kelvin Probe Force Microscopy. *Advanced Materials* **2006**, *18* (2), 145-164.
103. De Boer, B.; Hadipour, A.; Mandoc, M. M.; Van Woudenberg, T.; Blom, P. W. M., Tuning of metal work functions with self-assembled monolayers. *Advanced Materials* **2005**, *17*, 621-625.
104. Saito, N.; Hayashi, K.; Sugimura, H.; Takai, O.; Nakagiri, N., Surface potentials of patterned organosilane self-assembled monolayers acquired by Kelvin probe force microscopy and ab initio molecular calculation. *Chemical Physics Letters* **2001**, *349* (3-4), 172-177.
105. Ellison, D. J.; Lee, B.; Podzorov, V.; Frisbie, C. D., Surface Potential Mapping of SAM-Functionalized Organic Semiconductors by Kelvin Probe Force Microscopy. *Advanced Materials* **2011**, *23* (4), 502-507.
106. Rusu, P. C.; Brocks, G., Surface Dipoles and Work Functions of Alkylthiolates and Fluorinated Alkylthiolates on Au(111). *The Journal of Physical Chemistry B* **2006**, *110* (45), 22628-22634.
107. Friedlein, R.; Crispin, X.; Simpson, C. D.; Watson, M. D.; Jäckel, F.; Osikowicz, W.; Marciniak, S.; de Jong, M. P.; Samorì, P.; Jönsson, S. K. M.; Fahlman, M.; Müllen, K.; Rabe, J. P.; Salaneck, W. R., Electronic structure of highly ordered films of self-assembled graphitic nanocolumns. *Physical Review B* **2003**, *68* (19), 195414.
108. Palermo, V.; Palma, M.; Tomović, Ž.; Watson, M. D.; Friedlein, R.; Müllen, K.; Samorì, P., Influence of Molecular Order on the Local Work Function of Nanographene Architectures: A Kelvin-Probe Force Microscopy Study. *ChemPhysChem* **2005**, *6* (11), 2371-2375.
109. Verdaguer, A.; Weis, C.; Oncins, G.; Ketteler, G.; Bluhm, H.; Salmeron, M., Growth and structure of water on SiO₂ films on Si Investigated by Kelvin probe microscopy and in Situ X-ray spectroscopies. *Langmuir* **2007**, *23*, 9699-703.
110. Foster, M.; D'Agostino, M.; Passno, D., Water on MgO(1 0 0)—An infrared study at ambient temperatures. *Surface Science* **2005**, *590* (1), 31-41.
111. Björneholm, O.; Hansen, M. H.; Hodgson, A.; Liu, L.-M.; Limmer, D. T.; Michaelides, A.; Pedevilla, P.; Rossmeisl, J.; Shen, H.; Tocci, G.; Tyrode, E.; Walz, M.-M.; Werner, J.; Bluhm, H., Water at Interfaces. *Chemical reviews* **2016**, *116* (13), 7698-7726.
112. Ewing, G. E., Ambient Thin Film Water on Insulator Surfaces. *Chemical reviews* **2006**, *106* (4), 1511-1526.
113. Tu, A.; Kwag, H. R.; Barnette, A. L.; Kim, S. H., Water Adsorption Isotherms on CH₃-, OH-, and COOH-Terminated Organic Surfaces at Ambient Conditions Measured with PM-RAIRS. *Langmuir* **2012**, *28* (43), 15263-15269.

114. Wang, Z.; Nania, S. L.; Shaw, S. K., Structure of Aqueous Water Films on Textured –OH-Terminated Self-Assembled Monolayers. *Langmuir* **2015**, *31* (8), 2382-2389.
115. Rozenberg, M.; Loewenschuss, A.; Marcus, Y., An empirical correlation between stretching vibration redshift and hydrogen bond length. *Physical Chemistry Chemical Physics* **2000**, *2* (12), 2699-2702.
116. Chabinye, M. L.; Endicott, F.; Vogt, B. D.; DeLongchamp, D. M.; Lin, E. K.; Wu, Y.; Liu, P.; Ong, B. S., Effects of humidity on unencapsulated poly(thiophene) thin-film transistors. *Applied Physics Letters* **2006**, *88* (11), 113514.
117. Hendrik, B.; Ogletree, D. F.; Charles, S. F.; Zahid, H.; Miquel, S., The premelting of ice studied with photoelectron spectroscopy. *Journal of Physics: Condensed Matter* **2002**, *14* (8), L227.
118. Velasco-Velez, J.-J.; Wu, C. H.; Pascal, T. A.; Wan, L. F.; Guo, J.; Prendergast, D.; Salmeron, M., The structure of interfacial water on gold electrodes studied by x-ray absorption spectroscopy. *Science* **2014**, *346* (6211), 831-834.
119. Buckel, F.; Effenberger, F.; Yan, C.; Götzhäuser, A.; Grunze, M., Influence of Aromatic Groups Incorporated in Long-Chain Alkanethiol Self-Assembled Monolayers on Gold. *Advanced Materials* **2000**, *12* (12), 901-905.
120. Kobayashi, T.; Rentzepis, P. M., On the picosecond kinetics and photostability of indigo and 6,6'-dimethoxyindigo. *The Journal of Chemical Physics* **1979**, *70* (2), 886-892.
121. Seixas de Melo, J.; Moura, A. P.; Melo, M. J., Photophysical and Spectroscopic Studies of Indigo Derivatives in Their Keto and Leuco Forms. *The Journal of Physical Chemistry A* **2004**, *108* (34), 6975-6981.
122. Seixas de Melo, J.; Rondao, R.; Burrows, H. D.; Melo, M. J.; Navaratnam, S.; Edge, R.; Voss, G., Photophysics of an indigo derivative (keto and leuco structures) with singular properties. *J Phys Chem A* **2006**, *110* (51), 13653-61.
123. Irimia-Vladu, M.; Głowacki, E. D.; Troshin, P. A.; Schwabegger, G.; Leonat, L.; Susarova, D. K.; Krystal, O.; Ullah, M.; Kanbur, Y.; Bodea, M. A.; Razumov, V. F.; Sitter, H.; Bauer, S.; Sariciftci, N. S., Indigo - A Natural Pigment for High Performance Ambipolar Organic Field Effect Transistors and Circuits. *Advanced Materials* **2012**, *24* (3), 375-380.
124. Pitayatanakul, O.; Iijima, K.; Kadoya, T.; Ashizawa, M.; Kawamoto, T.; Matsumoto, H.; Mori, T., *Ambipolar Organic Field-Effect Transistors Based on Indigo Derivatives*. 2015; Vol. 19.
125. He, B.; Pun, A. B.; Zhrebetsky, D.; Liu, Y.; Liu, F.; Klivansky, L. M.; McGough, A. M.; Zhang, B. A.; Lo, K.; Russell, T. P.; Wang, L.; Liu, Y., New Form of an Old Natural Dye: Bay-Annulated Indigo (BAI) as an Excellent Electron Accepting Unit for High Performance Organic Semiconductors. *Journal of the American Chemical Society* **2014**, *136* (42), 15093-15101.
126. Ashizawa, M.; Masuda, N.; Higashino, T.; Kadoya, T.; Kawamoto, T.; Matsumoto, H.; Mori, T., Ambipolar organic transistors based on isoindigo derivatives. *Organic Electronics* **2016**, *35*, 95-100.
127. Rabani, E.; Reichman, D.; Geissler, P. L.; Brus, L. E., Drying-mediated self-assembly of nanoparticles. *Nature* **2003**, *213901*, 2-5.

128. Barth, J. V.; Costantini, G.; Kern, K., Engineering atomic and molecular nanostructures at surfaces. *Nature* **2005**, *437*, 671-9.
129. Miszta, K.; de Graaf, J.; Bertoni, G.; Dorfs, D.; Brescia, R.; Marras, S.; Ceseracciu, L.; Cingolani, R.; van Roij, R.; Dijkstra, M.; Manna, L., Hierarchical self-assembly of suspended branched colloidal nanocrystals into superlattice structures. *Nature Materials* **2011**, *10*, 872-876.
130. Lee, J. Y.; Roth, S.; Park, Y. W., Anisotropic field effect mobility in single crystal pentacene. *Applied Physics Letters* **2006**, *88* (25), 252106.
131. Reese, C.; Bao, Z., High-Resolution Measurement of the Anisotropy of Charge Transport in Single Crystals. *Advanced Materials* **2007**, *19* (24), 4535-4538.
132. Wen, S.-H.; Li, A.; Song, J.; Deng, W.-Q.; Han, K.-L.; Goddard, W. A., First-Principles Investigation of Anisotropic Hole Mobilities in Organic Semiconductors. *The Journal of Physical Chemistry B* **2009**, *113* (26), 8813-8819.
133. Vandevyver, M.; Albouy, P. A.; Mingotaud, C.; Perez, J.; Barraud, A.; Karthaus, O.; Ringsdorf, H., In-plane anisotropy and phase change in Langmuir-Blodgett films of disklike molecules. *Langmuir* **1993**, *9* (6), 1561-1567.
134. Kim, B.-G.; Jeong, E. J.; Chung, J. W.; Seo, S.; Koo, B.; Kim, J., A molecular design principle of lyotropic liquid-crystalline conjugated polymers with directed alignment capability for plastic electronics. *Nat Mater* **2013**, *12* (7), 659-664.
135. Schott, S.; Gann, E.; Thomsen, L.; Jung, S.-H.; Lee, J.-K.; McNeill, C. R.; Siringhaus, H., Charge-Transport Anisotropy in a Uniaxially Aligned Diketopyrrolopyrrole-Based Copolymer. *Advanced Materials* **2015**, *27* (45), 7356-7364.
136. Ling, M. M.; Bao, Z., Thin Film Deposition, Patterning, and Printing in Organic Thin Film Transistors. *Chemistry of Materials* **2004**, *16* (23), 4824-4840.
137. Lu, L.; Cui, H.; Li, W.; Zhang, H.; Xi, S., Selective Crystallization of BaF₂ under a Compressed Langmuir Monolayer of Behenic Acid. *Chemistry of Materials* **2001**, *13* (2), 325-328.
138. Benítez, I. O.; Talham, D. R., Brewster Angle Microscopy of Calcium Oxalate Monohydrate Precipitation at Phospholipid Monolayer Phase Boundaries. *Langmuir* **2004**, *20* (19), 8287-8293.
139. Sinnokrot, M. O.; Valeev, E. F.; Sherrill, C. D., Estimates of the Ab Initio Limit for π - π Interactions: The Benzene Dimer. *Journal of the American Chemical Society* **2002**, *124* (36), 10887-10893.
140. He, Y.; Zhu, B.; Inoue, Y., Hydrogen bonds in polymer blends. *Progress in Polymer Science* **2004**, *29* (10), 1021-1051.
141. Serrano-Andrés, L.; Roos, B. O., A Theoretical Study of the Indigoid Dyes and Their Chromophore. *Chemistry – A European Journal* **1997**, *3* (5), 717-725.
142. Scherwitzl, B.; Resel, R.; Winkler, A., Film growth, adsorption and desorption kinetics of indigo on SiO₂. *The Journal of chemical physics* **2014**, *184705*, 184705.
143. Ku, J.; Aruguete, D. M.; Alivisatos, A. P.; Geissler, P. L., Self-Assembly of Magnetic Nanoparticles in Evaporating Solution. *Journal of the American Chemical Society* **2011**, *133* (4), 838-848.
144. Varón, M.; Beleggia, M.; Kasama, T.; Harrison, R. J.; Dunin-Borkowski, R. E.; Puentes, V. F.; Frandsen, C., Dipolar Magnetism in Ordered and Disordered Low-Dimensional Nanoparticle Assemblies. *Scientific Reports* **2013**, *3*, 1234.

145. Sikes, H. D.; Schwartz, D. K., A Temperature-Dependent Two-Dimensional Condensation Transition during Langmuir–Blodgett Deposition. *Langmuir* **1997**, *13* (17), 4704-4709.
146. Wen, G.; Chung, B.; Chang, T., Effect of spreading solvents on Langmuir monolayers and Langmuir–Blodgett films of PS-b-P2VP. *Polymer* **2006**, *47* (26), 8575-8582.
147. Durbin, M. K.; Malik, A.; Richter, A. G.; Huang, K. G.; Dutta, P., In-Situ X-ray Diffraction Study of Langmuir–Blodgett Deposition. *Langmuir* **1997**, *13* (24), 6547-6549.
148. Gidalevitz, D.; Huang, Z.; Rice, S. A., Protein folding at the air–water interface studied with x-ray reflectivity. *Proceedings of the National Academy of Sciences of the United States of America* **1999**, *96* (6), 2608-2611.
149. Kim, S.; Lee, J. K.; Kang, S. O.; Ko, J.; Yum, J. H.; Fantacci, S.; De Angelis, F.; Di Censo, D.; Nazeeruddin, M. K.; Gratzel, M., Molecular engineering of organic sensitizers for solar cell applications. *Journal of the American Chemical Society* **2006**, *128* (51), 16701-16707.
150. Kasha, M., ENERGY TRANSFER MECHANISMS AND MOLECULAR EXCITON MODEL FOR MOLECULAR AGGREGATES. *Radiat. Res.* **1963**, *20* (1), 55-&.
151. McRae, E. G.; Kasha, M., Enhancement of Phosphorescence Ability upon Aggregation of Dye Molecules. *The Journal of Chemical Physics* **1958**, *28* (4), 721-722.
152. Wurthner, F.; Yao, S.; Debaerdemaeker, T.; Wortmann, R., Dimerization of merocyanine dyes. Structural and energetic characterization of dipolar dye aggregates and implications for nonlinear optical materials. *Journal of the American Chemical Society* **2002**, *124* (32), 9431-9447.
153. Zhao, Y. S.; Fu, H. B.; Peng, A. D.; Ma, Y.; Xiao, D. B.; Yao, J. N., Low-dimensional nanomaterials based on small organic molecules: Preparation and optoelectronic properties. *Advanced Materials* **2008**, *20* (15), 2859-2876.
154. Liu, Y.; Chen, S.; Lam, J. W. Y.; Lu, P.; Kwok, R. T. K.; Mahtab, F.; Kwok, H. S.; Tang, B. Z., Tuning the Electronic Nature of Aggregation-Induced Emission Luminogens with Enhanced Hole-Transporting Property. *Chemistry of Materials* **2011**, *23* (10), 2536-2544.
155. Eisfeld, A.; Briggs, J. S., The J- and H-bands of organic dye aggregates. *Chemical Physics* **2006**, *324* (2–3), 376-384.
156. Spano, F. C.; Silva, C., H- and J-aggregate behavior in polymeric semiconductors. *Annual review of physical chemistry* **2014**, *65*, 477-500.
157. Niles, E. T.; Roehling, J. D.; Yamagata, H.; Wise, A. J.; Spano, F. C.; Moule, A. J.; Grey, J. K., J-Aggregate Behavior in Poly-3-hexylthiophene Nanofibers. *Journal of Physical Chemistry Letters* **2012**, *3*, 259-263.
158. Panzer, F.; Sommer, M.; Bäessler, H.; Thelakkat, M.; Köhler, A., Spectroscopic Signature of Two Distinct H-Aggregate Species in Poly(3-hexylthiophene). *Macromolecules* **2015**, *48* (5), 1543-1553.
159. Lill, E.; Hefferle, P.; Schneider, S.; Dörr, F., Fluorescence decay times of indigo-derivatives measured by means of a synchroscan streak camera. *Applied Physics* **1980**, *22*, 197-200.

160. Seixas De Melo, J.; Moura, a. P.; Melo, M. J., Photophysical and spectroscopic studies of indigo derivatives in their keto and leuco forms. *Journal of Physical Chemistry A* **2004**, *108*, 6975-6981.
161. Costa, A. L.; Gomes, A. C.; Pillinger, M.; Goncalves, I. S.; de Melo, J. S. S., An Indigo Carmine-Based Hybrid Nanocomposite with Supramolecular Control of Dye Aggregation and Photobehavior. *Chemistry-a European Journal* **2015**, *21* (34), 12069-12078.
162. Singh, T. B.; Marjanović, N.; Matt, G. J.; Günes, S.; Sariciftci, N. S.; Montaigne Ramil, A.; Andreev, A.; Sitter, H.; Schwödiauer, R.; Bauer, S., High-mobility n-channel organic field-effect transistors based on epitaxially grown C60 films. *Organic Electronics* **2005**, *6* (3), 105-110.
163. Muccini, M., A bright future for organic field-effect transistors. *Nat Mater* **2006**, *5* (8), 605-613.
164. Wen, Y.; Liu, Y.; Guo, Y.; Yu, G.; Hu, W., Experimental Techniques for the Fabrication and Characterization of Organic Thin Films for Field-Effect Transistors. *Chemical reviews* **2011**, *111* (5), 3358-3406.
165. Liu, C.; Xu, Y.; Noh, Y.-Y., Contact engineering in organic field-effect transistors. *Materials Today* **2015**, *18* (2), 79-96.
166. Smits, E. C. P.; Mathijssen, S. G. J.; van Hal, P. A.; Setayesh, S.; Geuns, T. C. T.; Mutsaers, K. A. H. A.; Cantatore, E.; Wondergem, H. J.; Werzer, O.; Resel, R.; Kemerink, M.; Kirchmeyer, S.; Muzafarov, A. M.; Ponomarenko, S. A.; de Boer, B.; Blom, P. W. M.; de Leeuw, D. M., Bottom-up organic integrated circuits. *Nature* **2008**, *455* (7215), 956-959.
167. Martin, F.; Hendriksen, B.; Katan, A.; Ratera, I.; Qi, Y.; Harteneck, B.; Liddle, J. A.; Salmeron, M., Ultra-flat coplanar electrodes for controlled electrical contact of molecular films. *Review of Scientific Instruments* **2011**, *82* (12), 123901.
168. Di, C.-a.; Wei, D.; Yu, G.; Liu, Y.; Guo, Y.; Zhu, D., Patterned Graphene as Source/Drain Electrodes for Bottom-Contact Organic Field-Effect Transistors. *Advanced Materials* **2008**, *20* (17), 3289-3293.
169. Cao, Y.; Liu, S.; Shen, Q.; Yan, K.; Li, P.; Xu, J.; Yu, D.; Steigerwald, M. L.; Nuckolls, C.; Liu, Z.; Guo, X., High-Performance Photoresponsive Organic Nanotransistors with Single-Layer Graphenes as Two-Dimensional Electrodes. *Advanced Functional Materials* **2009**, *19* (17), 2743-2748.
170. Liu, W.; Jackson, B.; Zhu, J.; Miao, C., Large scale pattern graphene electrode for high performance in transparent organic single crystal field-effect transistors. *ACS Nano* **2010**, *4*, 3927-3932.
171. Kasha, M.; Rawls, H. R.; Ashraf El-Bayoumi, M., The exciton model in molecular spectroscopy. *Eighth European Congress on Molecular Spectroscopy* **1965**, 371-392.
172. Sauer, M.; Hofkens, J.; Enderlein, J., Basic Principles of Fluorescence Spectroscopy. In *Handbook of Fluorescence Spectroscopy and Imaging*, Wiley-VCH Verlag GmbH & Co. KGaA: 2011; pp 1-30.
173. Hirayama, F., Intramolecular Excimer Formation. I. Diphenyl and Triphenyl Alkanes. *The Journal of Chemical Physics* **1965**, *42* (9), 3163-3171.
174. Birks, J. B., Excimers and Exciplexes. *Nature* **1967**, *214* (5094), 1187-1190.

175. Bohn, P. W., Aspects of Structure and Energy Transport in Artificial Molecular Assemblies. *Annual Review of Physical Chemistry* **1993**, *44* (1), 37-60.
176. Irimia-Vladu, M.; Głowacki, E. D.; Troshin, P. a.; Schwabegger, G.; Leonat, L.; Susarova, D. K.; Krystal, O.; Ullah, M.; Kanbur, Y.; Bodea, M. a.; Razumov, V. F.; Sitter, H.; Bauer, S.; Sariciftci, N. S., Indigo--a natural pigment for high performance ambipolar organic field effect transistors and circuits. *Advanced materials (Deerfield Beach, Fla.)* **2012**, *24*, 375-80.
177. Giovannetti, G.; Khomyakov, P. A.; Brocks, G.; Karpan, V. M.; van den Brink, J.; Kelly, P. J., Doping Graphene with Metal Contacts. *Physical Review Letters* **2008**, *101* (2), 026803.
178. Blake, P.; Yang, R.; Morozov, S. V.; Schedin, F.; Ponomarenko, L. A.; Zhukov, A. A.; Nair, R. R.; Grigorieva, I. V.; Novoselov, K. S.; Geim, A. K., Influence of metal contacts and charge inhomogeneity on transport properties of graphene near the neutrality point. *Solid State Communications* **2009**, *149* (27-28), 1068-1071.
179. Nagashio, K.; Nishimura, T.; Kita, K.; Toriumi, A., Contact resistivity and current flow path at metal/graphene contact. *Applied Physics Letters* **2010**, *97* (14), 143514.
180. Watanabe, E.; Conwill, A.; Tsuya, D.; Koide, Y., Low contact resistance metals for graphene based devices. *Diamond and Related Materials* **2012**, *24*, 171-174.
181. Panchal, V.; Pearce, R.; Yakimova, R.; Tzalenchuk, A.; Kazakova, O., Standardization of surface potential measurements of graphene domains. *Scientific reports* **2013**, *3*, 2597.